IBRACON

REVISTA IBRACON DE ESTRUTURAS E MATERIAIS

IBRACON STRUCTURES AND MATERIALS JOURNAL

Volume 8, Number 1

February, 2015

ISSN 1983-4195

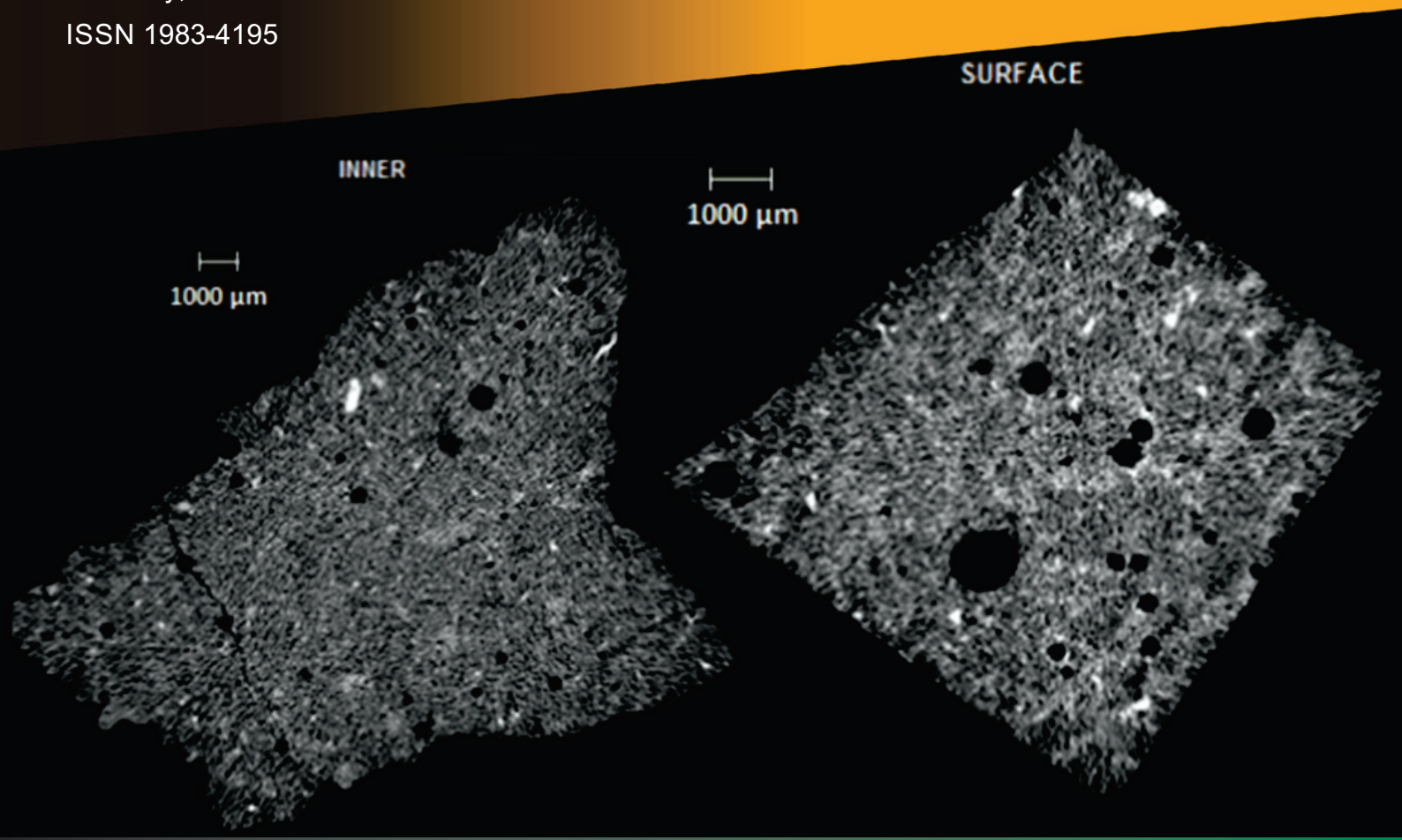

Contents

Editorial

With this issue (Volume 8 Number 1, February 2015), we open the eighth volume of the IBRACON Structures and Materials Journal. This issue contains five articles related to concrete structures and materials. The first article presents an application of Chapelle's method for determining the reactivity of pozzolanic materials. The method is applied to evaluate lime consumption by metakaolin, silica fume, fly ash, sugar cane bagasse ash and rice husk ash, comparing the result with mass proportions - lime:pozzolan 1:1, as originally proposed by Chapelle, and 2:1 according to Brazilian and French Standards. The second article evaluates the effect of polypropylene and steel fibers on the loss of water by evaporation and shrinkage of concrete. A study was carried out to relate the loss of water from the paste and the shrinkage during the first 28 days of age, using a control mix without fiber for comparison. Another article aims to evaluate the use of coal waste to produce concrete paving blocks. A process was developed with the purpose of reducing the sulfur content of the coal waste and changing the particle size distribution to meet the specifications for fine aggregates. The fourth article discusses the implementation and validation of a software for thermal analysis of two-dimensional structures subjected to fire. The last article discusses an anisotropic damage model for analysis of reinforced concrete structures submitted to reversal loading.

We congratulate the authors for the quality of the published articles and acknowledge the dedication of the reviewers.

Américo Campos Filho, José Luiz Antunes de Oliveira e Sousa, Roberto Caldas de Andrade Pinto and Romilde Almeida de Oliveira, Editors

Com esta edição (Volume 8, Número 1, Fevereiro de 2015), abrimos o oitavo volume da Revista IBRACON de Estruturas e Materiais. Este número contém cinco artigos sobre estruturas de concreto e materiais. O primeiro artigo apresenta uma aplicação do método de Chapelle para determinar a reatividade dos materiais pozolânicos. O método é aplicado para metacaulim, sílica ativa, cinza volante, cinza de bagaço de cana-de-açúcar e cinza de casca de arroz, comparando o resultado com proporções em massa cal: pozolana 1:1, conforme proposto originalmente por Chapelle, e 2: 1, de acordo com as normas brasileira e francesa. O segundo artigo avalia o efeito de fibras de polipropileno e de aço na perda de água por evaporação e na retração do concreto. Um estudo foi realizado para relacionar a perda de água da pasta e a retração nos primeiros 28 dias de idade, utilizando um traço de controle sem fibras para comparação. Outro artigo tem como objetivo avaliar a utilização de rejeitos de carvão para a produção de blocos de concreto para pavimentação. Um processo foi desenvolvido para reduzir o teor de enxofre dos rejeitos de carvão e ajustar o tamanho das partículas do material para as especificações de distribuição granulométrica de agregado miúdo. O quarto artigo aborda a implementação e validação de um programa computacional para análise térmica de estruturas bidimensionais submetidas ao fogo. O último artigo discute um modelo de dano anisótropo para a análise de estruturas de concreto armado submetidas a inversão de carregamento.

Parabenizamos os autores pela qualidade dos artigos publicados e agradecemos a dedicação dos revisores.

Américo Campos Filho, José Luiz Antunes de Oliveira e Sousa, Roberto Caldas de Andrade Pinto e Romilde Almeida de Oliveira, Editores

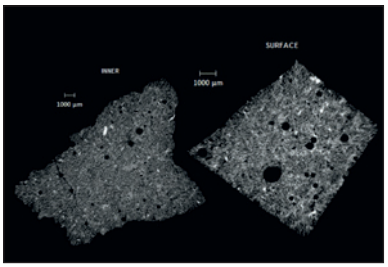

Cover: X-RAY MICROTOMOGRAPHY OF CONCRETE PORE STRUCTURE

Courtesy: E. E. BERNARDES, UFMG, BELO HORIZONTE, BRAZIL

Volume 8, Number 1
February 2015
ISSN: 1983-4195

REVISTA IBRACON DE ESTRUTURAS E MATERIAIS

IBRACON STRUCTURES AND MATERIALS JOURNAL

Contents

IBRACON

Ibracon Structures and Materials Journal
is published bimonthly (February, April, June, August, October and December) by IBRACON.

IBRACON
Instituto Brasileiro do Concreto
Founded in 1972

R. Julieta do Espirito Santo Pinheiro, 68
Jardim Olímpia, São Paulo – SP
Brasil – 05542-120
Phone: +55 11 3735-0202
Fax: +55 11 3733-2190
E-mail: arlene@ibracon.org.br
Website: http://www.ibracon.org.br

Cover design & Layout:
Ellementto-Arte
www.ellementto-arte.com

Diretoria

Diretoria
Biênio 2013/2015

Diretor Presidente
Túlio Nogueira Bittencourt

Assessores da Presidência
Augusto Carlos de Vasconcelos
José Tadeu Balbo
Selmo Chapira Kuperman

Diretor 1º Vice-Presidente
Julio Timerman

Diretor 2º Vice-Presidente
Nelson Covas

Diretor 1º Secretário
Antonio Domingues de Figueiredo

Diretor 2º Secretário
Arcindo Vaqueiro Y Mayor

Diretor 1º Tesoureiro
Claudio Sbrighi Neto

Diretor 2º Tesoureiro
Carlos José Massucato

Diretor de Marketing
Hugo da Costa Rodrigues Filho

Diretor de Eventos
Luiz Prado Vieira Júnior

Assessor de Eventos
Maurice Antoine Traboulsi

Diretor Técnico
Inês Laranjeira da Silva Battagin

Diretor de Relações Institucionais
Ricardo Lessa

Diretor de Publicações e Divulgação Técnica
Paulo Helene

Diretor de Pesquisa e Desenvolvimento
Ana Elisabete Paganelli Guimarães A. Jacintho

Diretor de Cursos
Iria Lícia Oliva Doniak

Diretor de Certificação de Mão-de-obra
Roseni Cezimbra

Conselho Diretor
Biênio 2013/2015

Sócios Titulares Individuais

Inês Laranjeira da Silva Battagin
Cláudio Sbrighi Neto
Ana Elisabete Paganelli Guimarães A. Jacintho
Augusto Carlos de Vasconcelos
Nélson Covas
Vladimir Paulon
Antonio Laranjeiras
Enio Pazini Figueiredo
Júlio Timermam
Luis Prado Vieira Júnior

Sócios Titulares Mantenedores e Coletivos

ABCP – Associação Brasileira de Cimento Portland
POLI-USP – Escola Politécnica da Universidade de São Paulo
IPT – Instituto de Pesquisas Tecnológicas de São Paulo
L. A. FALCÃO BAUER
FURNAS
ABCIC – Associação Brasileira da Construção Industrializada em Concreto
GERDAU
ABESC – Associação Brasileira das Empresas de Serviços de Concretagem
CNO – Companhia Norberto Odebrecht
OTTO BAUMGART

Conselheiros Permanentes

Eduardo Antonio Serrano
Paulo Helene
Ronaldo Tartuce
Rubens Machado Bittencourt
Selmo Chapira Kuperman
Simão Priszkulnik

IBRACON

Volume 8, Number 1 (February 2015) p. 1-7 • ISSN 1983-4195

REVISTA IBRACON DE ESTRUTURAS E MATERIAIS

IBRACON STRUCTURES AND MATERIALS JOURNAL

Indirect and direct Chapelle's methods for the determination of lime consumption in pozzolanic materials

Métodos de ensaio indiretos e método Chapelle direto para determinação do consumo de cal pelos materiais pozolânicos




V. A. QUARCIONI [a]
quarciva@ipt.br

F. F. CHOTOLI [a]
fchotoli@ipt.br

A. C. V. COELHO [b]
acvcoelh@usp.br

M. A. CINCOTTO [c]
cincotto@poli.usp.br

Abstract

In this work, comments are made about indirect methods and direct Chapelle's method applied to the determination of the reactivity of pozzolanic materials. The Chapelle's method is based on the lime-pozzolan reaction and quantifies the pozzolanic reactivity of any material intended to be applied by the cement industry. This lime consumption determination by the pozzolan through this reaction can be made with mass proportions – lime:pozzolan 1:1, as originally proposed by Chapelle or 2:1, as specified in Brazilian and French Standards. Comparative results with both proportions are presented for sugar cane bagasse ash, rice rusk ash, silica fume, fly ash, and metakaolin, commonly studied in our country. Statistical calculations showed that for some materials of similar characteristics to the researched RHA, FA e MK at issue, essays carried out with only 1g of CaO may be underestimating the amounts of CaO consumed per gram of pozzolanic material that can be obtained. Comments were made about the Brazilian and French Standards based on this method and emphasized the expression of lime consumption per mass of the amorphous phase of these materials, as determined by X ray diffraction analysis with the Rietveld refinement method.

Keywords: pozzolanic reactivity, Chapelle's method, sugar cane bagasse ash, rice rusk ash, silica fume, fly ash, metakaolin

Resumo

Neste trabalho, são discutidos os métodos indiretos e método de Chapelle direto aplicados para a determinação da reatividade de materiais pozolânicos. O método Chapelle baseia-se na reação química cal-pozolana e quantifica a reatividade pozolânica de materiais destinados à aplicação pela indústria de cimento. A determinação do consumo de cal pela pozolana que ocorre por meio desta reação química pode ser feita empregando-se as proporções em massa cal: pozolana 1:1, como proposto originalmente por Chapelle, ou 2:1, conforme especificado nas normas técnicas brasileira e francesa. São apresentados os resultados comparativos com as duas proporções cal-pozolana para cinza de bagaço de cana-de-açúcar, cinza de casca de arroz, sílica ativa, cinza volante e metacaulim, comumente estudados em nosso país. Os cálculos estatísticos indicaram para alguns materiais com características semelhantes aos da cinza de casca de arroz (CCA), cinza volante (CV) e metacaulim (MC), pesquisados em questão, que os ensaios realizados com apenas 1 g de CaO podem estar subestimando os valores obtidos de CaO consumidos por grama de material pozolânico. As normas brasileira e francesa foram discutidas com base nos resultados de ensaios Chapelle e enfatizou-se a quantificação do consumo de cal, em massa, pela fase amorfa destes materiais, que pode ser determinada pela análise de difração de raios-X por meio do método de refinamento de Rietveld.

Palavras-chave: reatividade pozolânica, método Chapelle, cinza de bagaço de cana-de-açúcar, cinza de casca de arroz, sílica ativa, cinza volante, metacaulim.

[a] *Instituto de Pesquisas Tecnológicas do Estado de São Paulo (IPT) - Laboratório de Materiais de Construção Civil, São Paulo, Brazil;*
[b] *Escola Politécnica da Universidade de São Paulo – Departamento de Engenharia Metalúrgica e de Materiais. São Paulo, Brazil;*
[c] *Escola Politécnica da Universidade de São Paulo – Departamento de Engenharia de Construção Civil, São Paulo, Brazil.*

Received: 28 Jan 2014 • Accepted: 11 Nov 2014 • Available Online: 03 Feb 2014

1. Introduction

The chemical effect resulting from the application of pozzolanic materials, as Portland cement clinker substitution, modifies the intrinsic characteristics of the paste due to a reaction with calcium hydroxide, which is called pozzolanic activity. Calcium hydroxide — portlandite — is released during the hydration of calcium silicates of the clinker and reacts with the pozzolan, forming hydraulic compounds, the most important of which being calcium silicate hydrate — C-S-H — due to the contribution of its mechanical properties to the hydrated paste. Not less important is the refinement of the porous system resulting from the precipitation of hydrated products and the physical effect from the pozzolan fine fraction [1].
The pozzolanic material does not react immediately with Portland cement under ambient temperature and pressure. As found in literature, the reaction can start anytime between one and seven days, depending on the reactivity of the pozzolanic material. Although such reaction may not have begun, the pozzolan has a beneficial effect by decreasing the released by hydration, which is particularly important for the concrete mass. Mitigation of the alkali-aggregate reaction and reduction of the concrete's susceptibility to leaching are other beneficial effects which occur at later ages [1, 2].
Pozzolans are composed by inert crystalline phases and a reactive vitreous phase. The pozzolanic reaction is the interaction of the solubilized elements of the vitreous phase, in a strong alkaline medium, pH 13.5, with the calcium ion present in the solution in contact with the cement [3]. Therefore, these materials are characterized by the degree of pozzolanic reaction, i.e., by its calcium consumption, which depends on: the Portland cement composition, with or without calcareous filler; the content and composition of the vitreous phase; cement and pozzolan specific surface area; the proportion cement:pozzolan.
Besides the quantification method of calcium consumption, the determination of the pozzolanic reactivity and its effect on the Portland cement hydration has been improved by the development of new methods of X-ray diffractometry applied to the qualitative determination in "real time", also called *in situ*, which allows the identification of the hydrated products formed during the first twenty hours, period in which the effects of additions and admixtures is studied, as well as their rheological properties. The analysis by the Rietveld refinement method quantifies the crystalline and vitreous phases, and the real consumption by the vitreous phase can be calculated; this determination applied over time allows the monitoring of the consumption of the vitreous phase and its effect on mortar or concrete properties [4, 5, 6].
Other methods are applied to determine the pozzolanic interaction in hardened state systems, pozzolan-hydrated lime or pozzolan-Portland cement. The portlandite consumption and the chemically combined water content are determined by thermogravimetry, following the reaction development [7, 8, 9]. The physical effect is commonly analyzed by the evolution of mechanical properties and porosity decrease.
Literature proposes a few methods for fly ash, which provide an indirect determination of pozzolanic reactivity. However, to explain the hydrated cement composition and the microstructure resulting from the interaction with the calcium from the cement and the elements of the pozzolan vitreous phase, the best way is the direct determination of the interaction degree of pozzolan-calcium oxide or calcium hydroxide. In fact, the direct determination conceived by Chapelle is at present a Standard Method in France for metakaolin [10], and in Brazil for pozzolanic materials in general [11].
In this work some comments are made about indirect methods published and the results of Chapelle's method applied to silica fume, fly ash, sugar cane bagasse and rice husk ashes, comparing the effect with the mass proportion lime: pozzolan 1:1, as originally proposed and 2:1 as specified in Brazilian and French Standards.

2. Comments about methods to determine pozzolanic reactivity

2.1 Indirect methods to determine fly ash pozzolanic reactivity

The most common criteria to determine pozzolanic activity is its strength activity index according to the ASTM C311 Standard [12] by applying the compressive strength test on a mix of cement-pozzolanic material. This test is indirect and does not give any information about the pozzolanic material itself, since the result depends on the chemical and physical characteristics of the cement.
Since the C-S-H is the reaction product with lime, which improves the mechanical properties, a high content of silica is the most important parameter of the vitreous phase. Raask & Bhaskar [13] proposed evaluating the fly ash quality by measuring the electrical conductivity of the dissolved silica content in hydrofluoric acid (0.1 M at 300°C, for 10 minutes) and the result inferred from a calibration curve plotted with silica fume. The authors admitted that in that concentration only the silica from the vitreous phase is solubilized. The most serious drawback to this method is that the authors did not prove that all silica present in the glass phase only was dissolved. Further, Majumdar & Larner also questioned the applicability of this method for fly ash [14].
Considering that lime consumption is an indicative of pozzolanic reactivity, Luxán et al. [15] proposed measuring the conductivity of a suspension of an opaline rock in saturated calcium hydroxide, stirring at 40°C. The conductivity decreased during the first 2 minutes then it stabilized. In the light of this result, this method was applied to a set of 100 natural materials, and a reactivity classification was proposed. The authors mentioned that during this period, the adsorption phenomenon is predominant, but did not seek to prove whether there was, in fact, early pozzolanic activity by chemical reaction. The method is therefore, questionable. However, Payá et al. [16] applied this method with modifications, on different fly ashes and concluded that the results were affected by: the soluble salts, the fly ash: lime suspension ratio, and the method does not apply to high-calcium fly ash.
Tashiro et al. [17] proposed to measure the resistivity of pastes of different materials with calcium hydroxide, steam cured at 70°C for 72 hours, determining the progress of the consumption of portlandite by XRD. No relationship was identified between the consumption of calcium hydroxide and the resistivity measurements.
Katyal et al. [18] were concerned only with the determination of the amount of active silica in fly ash, by comparing two treatments: a) initial heating in diluted hydrochloric acid until dry up, and the solid residue is digested in a digestion pump with potassium hexafluorosilicate; in the solution obtained, the hydrofluoric acid released by hydrolysis was titrated with sodium hydroxide. b) Digestion of an initial sample with diluted hydrochloric acid and then with a potassium

hydroxide 25% solution and quantification of the solubilized silica. The issue that arises is that since the content of the glass phase has not been provided it does not show- whether or not the dissolution was complete and from what phase the dissolved silica came from. The purpose of these methods was the speed which the pozzolanic activity could be determined, but in practice it did not happen. Surface phenomena interfere with these results, especially those relating to the high specific surface area of fly ash. In addition, the beginning of the specific reactivity for each pozzolan, it is highly important to determine the age at which the lime consumption is more significant, and the extension of the reaction contributing to the mechanical properties of cementitious materials.

Concerning the hardened state of pastes or mortars, the extension of the interaction was determined by quantifying the calcium hydroxide consumption by thermogravimetry [7,8, 9], or by determining the amount of unreacted fly ash, both methods were applied after different periods of cure. To quantify the unreacted fly ash, the hydrated products were washed with selective reagents. Different reagents were studied — picric acid-methanol, salicylic acid-methanol, hydrochloric acid-sodium carbonate [2, 19, 20, 21]. They all affect the results a little with some solubility of the fly ash, or the incomplete dissolution of hydrated products, which means that some corrections have to be made.

Direct determination of calcium consumption by Chapelle´s test

Chapelle's method modified by Raverdy et al. [22], is an accelerated method for the direct determination of the pozzolan lime consumption. A suspension of pozzolan/lime (1g/1g) and a blank of lime are kept reacting at 90°C for 16 hours; the lime consumed is calculated by the difference between the added and the remaining lime. This method was applied on industrial Portland pozzolanic cements and also on laboratory prepared with three Portland cements of different contents of C_3A and seven pozzolans, whose substitution levels were 10%, 20% and 35% at the same Blaine fineness, totalizing 63 samples. The authors evaluated the contribution of pozzolanic reactivity by comparing any increase in the compressive strength of the cements with pozzolans, after 28 days, with the corresponding pozzolan cements without addition. This study had the merit of indicating a minimum consumption as a reference data obtained from pozzolanic cements. Strength resistance at 180 days was plotted against the content of the glass phase [23] indicating only the gain for pozzolans for which lime consumption was greater than 330 mg per gram of glass phase.

In France, the Chapelle´s method was specified to select metakaolin for addition in concrete. The conformity criteria [10] are: (a) the content of SiO_2+Al_2O_3 >90%, calcined between 600°C and 850°C; this result means that metakaolin has to be obtained from high quality kaolin; (b) the loss on ignition has to be <4.0%; compared to the theoretical ignition loss of pure kaolin, of 13.76%. Thus, we can conclude that the kaolin must have a transformation degree of at least 70%; (c) the specified calcium hydroxide consumption has to be 700 mg/g of metakaolin [700mg of $Ca(OH)_2$ is equal to 530 mg of CaO]. In this standard method, the reaction is one gram of metakaolin and two grams of lime.

Chapelle's method was standardized too by ABNT - Associação Brasileira de Normas Técnicas (NBR 15895:2010), being applicable to natural and artificial pozzolans — calcined clay minerals, fly ash, silica fume and metakaolin but not to siderurgical slags [11]. In fact, it is also not applicable to metallurgical slags, as granulated blast furnace slag.

3. Experimental

Chapelle´s method is commonly applied by the IPT- Construction Materials Laboratory for pozzolanic reactivity determination of different materials. Raverdy´s et al. procedure underwent some adjustments to obtain a good reproduction of results. The results obtained with one gram of lime were carried out before the Brazilian Standard publication.

Test: All materials have their fineness specified, that is, a maximum residue of 12% of 45μm, or around 800 m²/kg. One gram of pozzolan is mixed with one gram of calcium oxide, added to 250 mL water in a 500 mL plastic Erlenmeyer and sealed. Calcium oxide is obtained from the calcination of a calcium carbonate pure reagent for analysis at 1000°C for 1 hour. After, the material is mixed quickly and manually and calcined for an additional half hour. The pozzolanic-lime mix and a blank are kept at 90±5°C in a closed Dubnoff shaking water bath for 16±2 hours (Fig. 1A and 1B), with some Teflon rods and stainless steel little balls. After cooling, 250 mL of a saccharose solution (240g/L) is added (Fig. 1C), Erlenmeyer is closed and the solution shaken for fifteen minutes (Fig. 1D); it is then filtered (Fig. 1E) through a pleated filter paper with an aliquot of 50 mL, the alkalinity is determined with hydrochloric acid 0.1M (Fig. 1I). During the filtration (Fig. 1F and 1G) and pipetting (Fig. 1H) phases it is important to carry them out as fast as possible to avoid carbon dioxide absorption. The result is expressed in reacted milligrams of lime (CaO) reacted or fixed per gram of pozzolan.

Figure 1-A illustrates the Nova Ética, type 304E Thermostatic Bath, with a digital microprocessed controller, at a 0.1°C resolution and a sensor Pt-100. The bath reservoir has an available capacity of 12 L of water, which is enough to maintaining the level of the Erlenmeyer solution covered, kept constant. The evaluation of its thermal profile showed that the 4°C temperature gradient does not interfere with the test results [24].

Calculation considering 2g of CaO and 1g of pozzolan:

$$mg\,CaO\,per\,gram\,of\,material = \frac{28x\left(v_3 x m_3 - v_2\right)x F_c x 2x2}{m_4 x m_3 x m_2} \quad (1)$$

being:

m_2 = grams of pozzolanic material;
m_3 = grams of CaO mixed with pozzolanic material;
m_4 = grams of CaO in the blank test;
v_2 = milliliters of HCl 0.1M consumed by the sample solution;
v_3 = milliliters of HCl 0.1M consumed by the blank solution;
F_c = correction factor of HCl 0.1M standard solution.

4. Results and discussion – calcium consumption of different pozzolans

Regarding to the reference metakaolin, the medium, maximum, minimum and standard deviation results are presented on Table 1. We can see that although consumption increases, the result with 2g is not the double of the result with 1g. The Table also presents the calcium oxide results determined and calculated as calcium hydroxide (CaO x 1.32). Tables 2 and 3 illustrate the results of the

Figure 1 – Dubnoff shaking water bath with Erlenmeyer prepared for the Chapelle´s test and illustrative steps of this essay

Dubnoff shaking water bath

Detail of Dubnoff shaking water bath

Addition of a sucrose solution

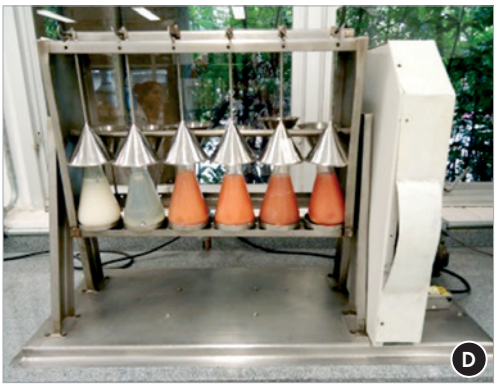

Agitation after addition of the sucrose solution

Decantation before filtration

Filtering the set of tests

Samples at the end of filtration

Pipetting a volume set to titration

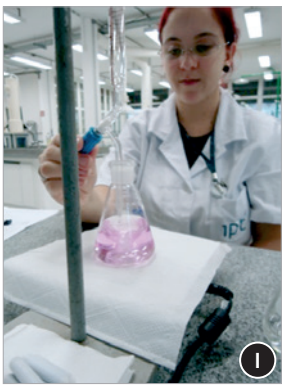

Titration of a sample

pozzolanic materials analyzed in the IPT's Laboratory in the last three years, tests being carried out with one gram and two grams of calcium oxide, respectively.

5. Results and discussion – calcium consumption of different pozzolans

Regarding the reference metakaolin, the mean, maximum, minimum and standard deviation results are presented on Table 1. We can see that the CaO consumption increases. Table 1 also presents calcium oxide results calculated as calcium hydroxide (CaO x 1.32). Table 2 illustrates the calcium consumption of the pozzolanic materials that has been analyzed in IPT's Laboratory in the last three years, tests being carried out with one gram and two grams of calcium oxide. Analysis of variance (ANOVA) was carried out between 1g and 2g results in order to observe if one gram of calcium oxide is sufficient to consume all the existing vitreous phase in pozzolanic material. Figure 2 presents graphically the dispersion of the results.

Table 1 – Calcium consumption of metakaolin as the reference material

Calcium consumption	Test with 1g of CaO (188 tests)		Test with 2g of CaO (56 tests)	
	CaO mg/g sample	$Ca(OH)_2$ mg/g sample	CaO mg/g sample	$Ca(OH)_2$ mg/g sample
Medium	857	1131	1068	1410
Maximum	876	1156	1134	1497
Minimum	833	1100	973	1284
Standard deviation	11	–	48	–

A wide result variation was observed in three materials: sugar cane bagasse ash (SCBA), rice husk ash (RHA) and silica fume (SF). SCBA and RHA are generally collected at the production site and calcined under temperature conditions and residence time specific to each research laboratory. Consequently, the composition of the ash and content of vitreous phase may vary. The region from where they come from also influences their composition due to the type of fertilizer employed. This can explain the significant calcium consumption difference for these two materials.

SF, on the contrary, comes from industrial processes under controlled conditions and should have homogeneous characteristics which restricts the variation of calcium consumption. At the moment, we have no explanation for the wide degree of variation observed.

Fly ash (FA) and metakaolin (MK) also come from industrial processes under controlled conditions. In the case of these two materials, the variation of the results was quite small as expected.

An analysis of variance (ANOVA) carried out for the 1g and 2g CaO results made it possible to confirm that the results of consumed CaO are statistically equal, whether starting from 1g or 2g of CaO, for sugar cane bagasse ash and for fly ash. It can be said that for these two types of materials, 1g CaO is sufficient to consume practically the whole vitreous phase contained in one gram of pozzolanic material, and that an increase in the amount of CaO does not give rise to an increase in consumption.

In the other tested materials (RHA, FA and MK), the increase in the amount of CaO initially added (from 1g to 2g) gives rise to a statistically significant increase in CaO consumption. These materials should have vitreous phases whose nature and/or amount are such that they do not completely react when only 1g of CaO is added, and require a higher lime concentration. This finding, in addition to the metakaolin results presented on Table 1, suggest that for some materials of similar characteristics to the researched RHA, FA e MK at issue, essays carried out with only 1g of CaO may be underestimating the amounts of CaO consumed per gram of pozzolanic material that can be obtained. For this very reason, the French and Brazilian standards were objective by adopting the use of 2g of CaO.

6. Conclusions

The number of tests made with metakaolin illustrates the good reproducibility of the method for each lime-pozzolan proportion.

The difficulty found in applying Chapelle's method as disclosed by Raverdy et al. was the glassy phase determination, which has now been solved with the introduction of the Rietveld refinement method of the XRD analysis interpretation. All these results of calcium consumption refer to the pozzolanic material as received; real consumption cannot be given because the vitreous phase was not determined.

Table 2 – Calcium consumption (g of CaO/g of pozzolanic material) of different pozzolanic materials. Tests were carried out with 1g or 2g of CaO. SCBA = sugar cane bagasse ash; RHA = rice husk ash; FA = fly ash; MK = metakaolin; SF = silica fume

	SCBA		RHA		FA		MK		SF	
	1g	2g	1g	2g	1g	2g	1g	2g	1g	2g
Mean value	279	298	622	864	269	403	656	842	755	1089
Minimum value	146	143	255	559	174	286	579	752	394	967
Maximum value	468	568	867	1080	378	489	804	1015	858	1153
Standard deviation	106	145	141	179	97	91	50	101	117	71
Number of materials	7	13	16	6	4	4	17	8	16	5
ANOVA analysis - with 95% confidence, 1g and 2g results are:	equal		different		equal		different		different	

However, these results allow us to emphasize that the conclusions drawn about the chemical effect of the properties of Portland cements where the clinker has been replaced by pozzolan have to take in account the real content of the vitreous phase and the effective reactivity.

Chapelle's method quantifies the calcium consumption related to the amorphous or vitreous phase of pozzolanic materials. The Rietveld refinement method gives the percentage of the amorphous and vitreous phase. These available methods allow correlating the effective calcium consumption with the effect of mechanical properties of the cements with clinker replacement by pozzolanic materials.

7. Acknowledgements

The authors are very thankful to Instituto de Pesquisas Tecnológicas (IPT) for its permission to publish these results and the financial support for this study.

8. References

[01] MASSAZZA, F. Pozzolans and pozzolanic cements. In: Lea´s chemistry of cement and concrete. Edited by Peter C. Hewlett. Fourth Edition. 1998.

[02] UCHIKAWA, H. Effect of blending components on hydration and structure formation. In: 8th INTERNATIONAL CONGRESS ON THE CHEMISTRY OF CEMENT (ICCC). Special Reports – Vol. 1, p. 249 – 280. Rio de Janeiro, 1986.

[03] UCHIKAWA, H., USHIDA, S., HANEHARA, S Effect of character of glass phase in blending components on their reactivity in calcium hydroxide mixture. 8th INTERNATIONAL CONGRESS ON THE CHEMISTRY OF CEMENT. Vol. IV, Rio de Janeiro - Brazil, 1980, 245- 250.

[04] HESSE, C., GOETZ-NEUNHOEFFER, F., NEUBAUER, J., BRAEU, M., GAEBERLEIN, P. Quantitative in-situ x-ray diffraction analysis of early hydration of portland cement at defined temperatures. JCPDS-International Centre for Diffraction Data 2009 ISSN 1097-0002.

[05] WARD, C. R.; FRENCH, D. Determination of glass content and estimation of glass composition in fly ash using quantitative X-ray diffractometry. Fuel, Volume 85, Issue 16, p. 2268 – 2277, November 2006.

[06] GOBBO, L. A.; SANT'AGOSTINO, L. M.; D'AGOSTINO, L. Z. XRD-Rietveld quantitative analysis of glass-containing by-products used in the Brazilian cement industry, 12th International Congress on the Chemistry of Cements. Montreal, Canada, 2007.

[07] VEDALAKSHMI, R.; RAJ, A. S.; SRINIVASAN, S.; BABU, K. G. Quantification of hydrated cement products of blended cements in low and medium strength concrete using TG and DTA technique. Thermochimica Acta, Vol. 407, Issues 1 – 2, p. 49 – 60, December 2003.

[08] ROSZCZYNIALSKI, W. Determination of pozzolanic activity of materials by thermal analysis. Journal of Thermal Analysis and Calorimetry, Vol. 70, Number 2, p. 387 – 392, September 2002.

[09] BAERT, G., HOSTE, S., De SHUTTER, G., De BELLIE, N. Reactivity of fly ash in cement paste studied by means

Figure 2 – Calcium consumption (g of CaO/g of vitreous of materials) of different pozzolanic materials. Tests were carried out with 1g (solid lines) or 2g (hollow lines) of CaO. Vertical lines represent the scattering of the results; mean values are shown as horizontal dashes. SCBA = sugar cane bagasse ash; RHA = rice husk ash; FA = fly ash; MK = metakaolin; SF = silica fume

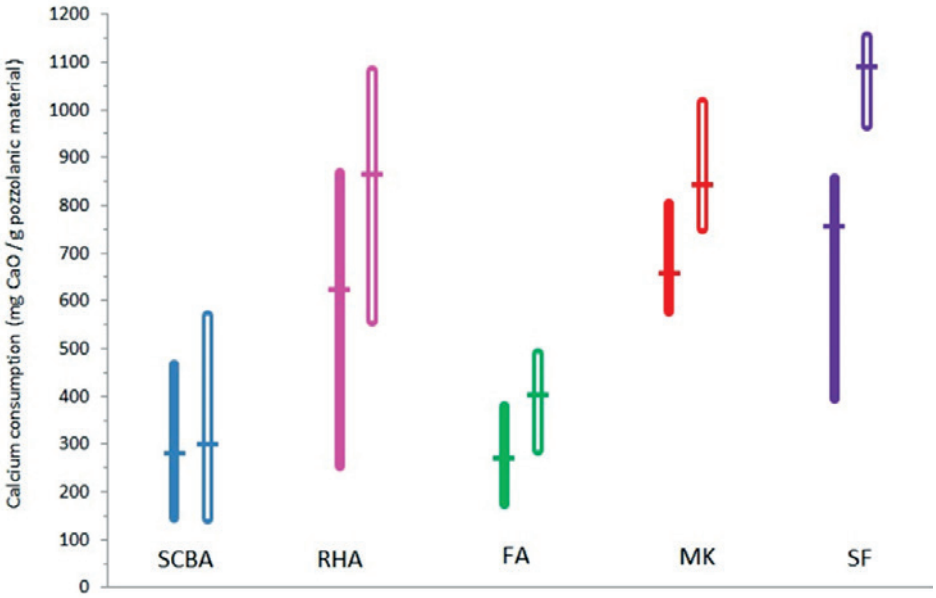

of thermogravimetry and isothermal calorimetry. Journal of Thermal Analysis and Calorimetry, 94, Issue 2 (2008) 485-492.

[10] AFNOR – Association Française de Normalisation - Standard NF P 18-513/2010 – "Pozzolanic addition for concrete – Metakaolin – Definitions, Specifications and Conformity Criteria,19 p.

[11] ABNT- Associação Brasileira de Normas Técnicas NBR 15.895/10 "Materiais pozolânicos - Determinação do teor de hidróxido de cálcio fixado - Método Chapelle modificado"

[12] American Society for Testing and Materials - ASTM C 311 Standard methods for sampling and testing fly ash in natural pozzolans for use as a mineral admixture in Portland cement concrete.

[13] RAASK, E., BHASKAR, M. C., Pozzolanic activity of pulverized ash, Cement and Concrete Research, 5(1975) 363-375.

[14] MAJUMDAR, A. J., LARNER, L. J., The measurement of pozzolanic activity (Note), Cement and Concrete Research, 7 (1977) 209-210.

[15] LUXÁN, M. P., MADRUGA, F., SAAVEDRA, J. Rapid evaluation of pozzolanic activity of natural products by conductivity measurements, Cement and Concrete Research, 19 (1989) 63-68.

[16] PAYÁ, J., BORRACHERO, M. V., MONZÓ, J., PERIS-MORA, E., AMAHJOUR, F., Enhanced conductivity measurement techniques for evaluation of fly ash pozzolanic activity, Cement and Concrete Research, 31(2001) 41-49.

[17] TASHIRO, C., IKEDA, K., INOUE, Y., Evaluation of pozzolanic activity by the electric resistance measurement method. Cement and Concrete Research, 24(1994) 1133-1139.

[18] KATYAL, N. K., SHARMA, J. M., DHAVAN, A.K., ALI, M. M., MOHAN, K., Development of a rapid method for the estimation of reactive silica in fly ash, Cement and Concrete Research, 38 (2008) 104-106.

[19] OHSAWA, R., ASAGA, K, GOTO, S., Daimon, M. Quantitative determination of fly ash in hydrated fly ash-CaSO4-Ca(OH)2. Cement and Concrete Research, 15 (1985) 357-366.

[20] SHIQUN LI, DELLA M. ROY, AMITHABA KUMAR, Quantitative determination of pozzolans in hydrated systems of cement or Ca(OH)2 with fly ash or silica fume, Cement and Concrete Research, 13(1985) 1079-1086.

[21] BEN HAHA, M., E Weerdt, K., LOTHENBACH Quantification of the degree of reaction of fly ash. Cement and Concrete Research, 40 (2010)14620-11629.

[22] RAVERDY, M.; BRIVOT, F.; PAILLERE, A. M.; DRON, R. Appreciation of pozzolanic reactivity of minor components. 7th INTERNATIONAL CONGRESS ON THE CHEMISTRY OF CEMENT. Vol. 3, Paris, France, 1980.

[23] MILLET, J., HOMMEY, R., BRIVOT, F. Dosage de la phase vitreuse dans les matériaux pozzolaniques. Bulletin nº. 92, 1977, 101-104.

[24] CHOTOLI, F. ,F., ALEIXO, D.M., COSTA, R.G., CASTANHO, M. A. P. Avaliação do perfil térmico de banho-maria com agitação tipo "Dubnoff" ENQUALAB-2007 – Congresso da Qualidade em Metrologia-Rede Metrológica do Estado de São Paulo – REMESP- SP, 2007.

Volume 8, Number 1 (February 2015) p. 8-13 • ISSN 1983-4195

REVISTA IBRACON DE ESTRUTURAS E MATERIAIS

IBRACON STRUCTURES AND MATERIALS JOURNAL

The effect of fibers on the loss of water by evaporation and shrinkage of concrete

Efeito das fibras na perda da água por evaporação e na retração do concreto

N. M. P. PILLAR [a]
nr.pillar@gmail.com

W. L. REPETTE [a]
wellington.repette@gmail.com

Abstract

Shrinkage is one of the least desirable attributes in concrete. Large areas of exposed concrete surfaces , such as in shotcrete tunnel linings, where it is practically impossible to make a moist cure, are highly susceptible to plastic shrinkage at early ages. The autogenous and drying shrinkage can lead to states of greater than threshold strength, causing fracture, mechanical damage and lack of durability of concrete structures. The addition of fibers can greatly reduce plastic shrinkage, but has limited effect in mitigating autogenous and drying shrinkage. To evaluate the performance of polypropylene and steel fibers to understand their effect on shrinkage of concrete, a study was carried out to relate the loss of water from the paste and the shrinkage during the first 28 days of age, and compare it with a control mix without fiber. The loss of water was obtained by the weight loss of the specimens at different ages, since the only component that could contribute for the loss of weight was the water lost by the paste of the concrete. And the paste itself is the only source of shrinkage. Uniaxial compressive tests from very early ages enabled the determination of time when plastic shrinkage ended. It was observed that the control concrete mix lost three times more water and developed plastic and drying shrinkage 60 % higher than the fiber reinforced concrete mixes. It was possible to demonstrate that the reduced loss of water caused by the incorporation of fibers is related to the mitigation of plastic shrinkage. It was observed that the fibers are effective to restrain the movement of water through the cement paste in the plastic state, however such effect is limited after concrete starts the hardening state.

Keywords: fiber reinforced concrete, plastic shrinkage, drying shrinkage, water loss, early age properties.

Resumo

A retração é um dos atributos menos desejáveis em concreto. Grandes áreas de superfícies expostas de concreto, tais como nos túneis em concreto projetado, onde é praticamente impossível proceder a uma cura úmida, são altamente suscetíveis à retração plástica nas primeiras idades. Retrações autógena e por secagem podem conduzir a estados de tensões maiores que a limite, provocando fratura, comprometimento mecânico e da durabilidade das peças de concreto. A adição de fibras pode reduzir consideravelmente a retração plástica, mas apresenta efeito limitado na mitigação das retrações autógena e por secagem. Na busca pela avaliação do desempenho das fibras e entendimento dos seus efeitos na retração do concreto relacionou-se a perda de água da pasta com a retração no período dos primeiros 28 dias. Concretos reforçados com fibras de polipropileno e de aço tiverem seus desempenhos em retração e perda de água comparados com um traço de controle sem fibra. A perda de água foi obtida pela perda de peso dos espécimes em diferentes idades, pois o único componente que contribui para a perda de peso é a perda de água pela pasta. E a pasta é a única fonte de retração. Testes de compressão uniaxial em idades muito precoces auxiliaram na determinação da idade quando a retração plástica terminou. Foi observado que o traço de controle perdeu três vezes mais água e desenvolveu retração plástica e por secagem 60 % mais altas do que os traços com fibras no mesmo período. Foi possível demonstrar que a redução da perda de água causada pela incorporação das fibras está relacionada com a mitigação da retração plástica. Observou-se que as fibras são eficazes em conter o movimento de água através da pasta de cimento no estado plástico, mas o mesmo não se dá após o início do endurecimento do concreto.

Palavras-chave: concreto reforçado com fibra, retração plástica, retração por secagem, perda de água, propriedades nas primeiras idades.

[a] *Universidade Federal de Santa Catarina – UFSC, Civil Engineering Department, Florianópolis, SC, Brazil.*

Received: 28 Aug 2012 • Accepted: 12 Nov 2014 • Available Online: 03 Feb 2014

1. Introduction

Plastic shrinkage is the volume contraction due to the loss of water in the plastic paste. Drying shrinkage is the volume change associated with the loss of water from the hardened paste structure. Autogenous shrinkage is the change due to the consumption of water during the hydration process. Shrinkage has harmful effects on concrete structure life span if the right measures are not taken place on time [1]. For this purpose, it is reported in the history of concrete that Romans, more than 2000 years ago, incorporated horse hair to reduce shrinkage in concrete; as well as the industry of concrete technology has developed shrinkage-reducing admixtures to reduce the harmful effects of shrinkage. It is also largely accepted that plastic shrinkage can be prevented through wet curing, however large areas of exposed concrete surfaces, such as lining of tunnels in shotcrete, where is practically impossible to make a moist cure, are highly susceptible to plastic shrinkage [2]. Tunnels are also subjected to great movement of warm or cool air, which propitiates evaporation, increasing water loss and consequent plastic shrinkage on the concrete surface [3]. If the loss of water is severe, internal strains may develop due to capillary pressures in the concrete mass causing concrete to shrink [4]. In structures restrained by a substrate, such as tunnel linings and concrete sidewalks, shrinkage generates internal tensile stresses in the concrete mass that can lead to crack if the internal tensile stress exceeds the low tensile strength of the concrete at early ages [1,2]. It is reported in the literature that plastic shrinkage cracking in concrete develops within about the first 3 hours after placement of the material and have a “map” like pattern [5]. Plastic shrinkage cracks can cross an entire slab and form planes of weakness reducing the integrity of the structure before concrete has achieved its final strength. The addition of fibers, such as steel and polypropylene, can bridge the forces across the cracks and can reduce plastic shrinkage cracking up to 70-80 % [5].

Currently polypropylene fibers are the favorite in tunnels because they prevent concrete spalling during events of fire [6,7]. In the plastic state, such fiber inhibits exudation and segregation due to their large surface area, by the accumulation of water on its surface, suppressing plastic shrinkage cracking at early ages. They are low cost, easily dispersible and inert in high pH. It has been reported that polypropylene fibers are more effective for this purpose than steel fibers [2,5,6,7].

If the loss of water in the paste is closely related to shrinkage, it will be possible to cross both parameters to better understanding the phenomenon of shrinkage on its different phases, plastic and hardened. This procedure can lead to a better choice for the compounds of a concrete mixes.

However, it is important to determine when plastic shrinkage ended and concrete started the hardening process. Some authors call this time as the *“time zero”* [8]. Up to now, there is no agreement among the technical community, on the exact time to be considered “*time zero*”; some adopted the initial setting time; others the final setting time; and others even another different time [8].

This paper aims to determine the influence of fibers, not only on plastic shrinkage, but also on drying shrinkage, by crossing the loss of water with measured shrinkage on unloaded specimens, during the first 28 days, for 3 concrete mixes: Plain Concrete (PC) as control, Polypropylene Fiber Reinforced Concrete (PFRC) and Steel Fiber Reinforced Concrete (SFRC).

2. Materials and experimental program

The basic plain concrete (PC) used as a control mix for the steel (SFRC) and polypropylene (PFRC) fiber reinforced mixes, consisted of: Australian type SL (shrinkage limited) Portland Cement (420 kg); silica fume (40 kg); fly ash (60 kg); coarse aggregate (450 kg) (10 mm crushed river gravel); coarse sand (770 kg); fine sand (370 kg); water (210 kg) and Rheobuild 100 superplasticizer (1 liter); the water/ binder ratio was 0.40 (Table 1). Fibers were added to the above reference mix to produce the two fiber reinforced concrete mixes (PFRC and SFRC). Novotex FE 0730 steel fiber for SFRC, with tensile strength of 1200 MPa; modulus of elasticity

Table 1 – Mix proportion for PC, SFRC and PFRC

Mix	Control	Steel fiber	Polypropylene fiber
	(PC)	(SFRC)	(PFRC)
Portland Cement (kg/m³)	420	420	420
Silica fume (kg/m³)	40	40	40
Fly ash (kg/m³)	60	60	60
Coarse aggregate (kg/m³)	450	450	450
Coarse sand (kg/m³)	770	770	770
Fine sand (kg/m³)	370	370	370
Water (kg/m³ and W/B ratio)	210 and 0.4	210 and 0.4	210 and 0.4
Superplasticizer (liter)	1	1.6	0.75
Steel fiber (kg/m³ and vol.%)	–	60 and 2.5	–
Polypropylene fiber (kg/m³ and vol.%)	–	–	9 and 1
Moist content (%)	10.2	9.9	10.2

Figure 1 – Shrinkage specimen

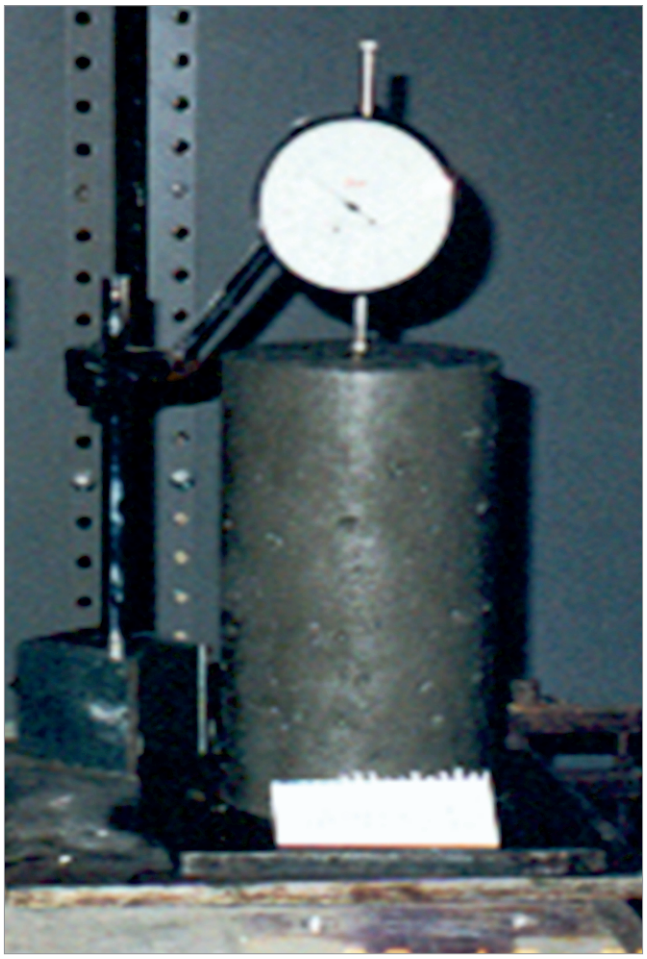

of 210 GPa; 30 mm long by 1.5 mm in diameter; flat ends, were added at a proportion of 2.5% by weight of concrete (i.e. at a dosage of 60 kg/m^3). The specific weight of the steel fiber was 7.9 (kg/dm^3) and the dosage rate by volume was therefore 0.76% (based on a concrete density of 2400 kg/m^3). Polypropylene S-152 HPP fibers were used for PFRC mix. These crimped fibers were 50 mm long, 2.5 mm diameter, specific weight of 0.91 (kg/dm^3), with a tensile strength of 400 MPa and a modulus of elasticity of 4.80 GPa. And a dosage rate of 0.38% by weight of concrete (i.e. 9 kg/m^3) or 1% by volume. The SL (shrinkage limit) type of Portland Cement was specified by AS 3972 94 , which allows a maximum drying shrinkage strain of 750 μstrain at 28 days of age, with shrinkage tests starting from 7 days of age [10]. The superplasticizer was a sodium naphthalene formaldehyde sulphonate based admixture (Rheobuild 1000, BASF), with solids content of 38-42%.

The moisture content was measured by using standard small tin containers filled with the fresh concrete and weighed immediately on a high precision scale, while the cylinders were casted. The tins were placed in a multi-use electrical oven with a temperature of 105 ºC for more than 12 hours. After that, when the samples have cooled they were weighed again. For example, for PFRC the self-weight of the container was 25.8 g, the wet concrete weighed 167.9 g; the dry concrete weighed 152.3 g. Therefore the mass of water evaporated was 15.6 g, which provided a moisture content of 10.2 % for PFRC.

The loss of water was obtained by the weight loss of the specimens at different ages, since the only component that could contribute for the loss of weight was the water lost by the paste of the concrete. And the paste itself is the only source of shrinkage.

Shrinkage and compressive strength were measured on cylinders of 100 mm diameter x 200 mm (see Figure 1). Plastic cylinder moulds with a longitudinal cut and tighten by belts allowed to strip the specimens with no disturbance, enabling testing the green concrete at very early ages, say less than 4 hours after casting. Moisture content was taken from all mixes; PC and PFRC had 10.2 % moist content, while SFRC had 9.99%. All specimens were stored and tested in the same ambient conditions (T= 23 ºC and RH= 73%), and stripped from moulds at 4 hours after casting.

Shrinkage tests started at 4 hours after casting without any wet cure, using the standard apparatus with dial gauges with divisions of 0.002 mm as shown at (Figure 1). During the first 12 hours, readings of shrinkage and RH were taken at each hour. Compressive strength (Table 2) and weight loss were taken at every 2 hours in the first 8 hours. After this age, shrinkage and RH were measured every day; while weight loss and compressive strength were measured at 24, 72, 96, 168 and 672 hours. No specific autogenous shrinkage test was performed on sealed specimens, therefore the measured shrinkage here presented contains the plastic, the autogenous and the drying components depending on the age analyzed.

3. Results and discussions

The compressive strength results for PC, PFRC and SFRC from 2 hours to 28 days after casting, as a reference of the mixes are presented at Table 2. It can be observed that the Fiber Reinforced Concretes developed higher compressive strengths during the first

Table 2 – Compressive strength (MPa)

Mix	2 hrs	4hrs	6 hrs	8 hrs	24 hrs	72 hrs	168 hrs	672 hrs
PC	0.03	0.09	0.3	0.7	16	27.3	32	38.4
PFRC	0.08	0.39	1.15	2.0	15.3	23.6	30	37.5
SFRC	0.08	0.3	0.7	1.64	14.3	23	29	35

Figure 2 – Shrinkage strain versus time during 28 days test

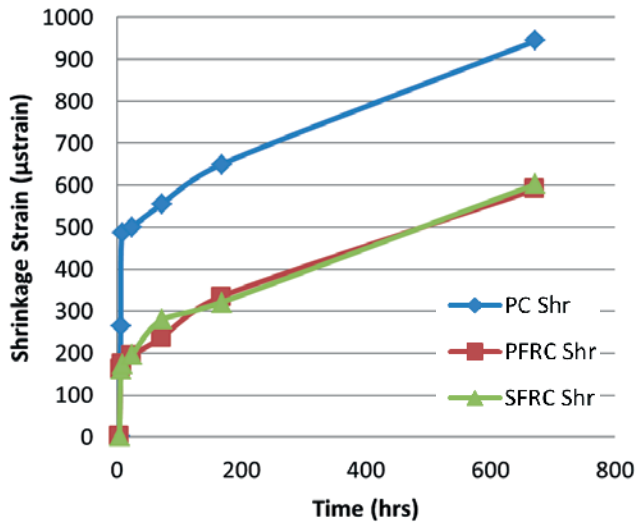

8 hours of age when compared with the control mix PC. Fibers may act like a sort of accelerator, interfering on setting time of concrete, as Soroushian et al apud Tanesi and Figueiredo [6] already mentioned. Soroushian et al found that fibers can accelerate the initial and final set from 9% to 27% respectively with and addition of 0.1 % of fibers, but not enough data to prove such find yet. Based on Mindess [9], the final setting time starts when concrete achieves a compressive strength of 0,7 MPa in a cylindrical specimen under compression test. Therefore, based on Table 2, it can be implied that PFRC has set say at 5 hours after casting, SFRC from 6 hours after casting, while PC sets from 8 hours of age on. After 8 hours of age, all mixes developed similar compressive strengths, where PC indeed developed compressive strengths slightly higher than PFRC and SFRC as shown on Table . These facts will be also observed on the studies of shrinkage and loss of water presented subsequently.

The Shrinkage curves depicted at (Figure 2) are the average measure of 2 specimens. It shows that PC developed a total shrinkage strain at 28 days of age of about 944 µstrain, while PFRC and SFRC had similar behaviour with 590 µstrain and 602 µstrain, respectively. Therefore, PC had 60 % more total shrinkage than PFRC and SFRC, demonstrating that the fibers are the sole compound that might contribute for the reduced shrinkage in these mixes. As can be also observed, PFRC and SFRC developed steep shrinkage curves in the first 6 hours of age reaching about 160 µstrain, while PC developed a significant steep shrinkage curve during the first 8 hours of age reaching 485 µstrain (Figure 2). After 8 hours of age all mixes developed similar shrinkage rates as shown in (Figure 3). Therefore, based on Table 2 and Figure 3, it can be assumed that PFRC and SFRC are on their plastic state prior 6 hours of age, while PC is on its plastic state until 8 hours of age. After that, all mixes behaved similarly with regard shrinkage and compressive strength, showing that the fibers are effective on mitigating plastic shrinkage, but does not interfere during the hardening state.

When Shrinkage and Loss of Water are analysed altogether along the period of 28 days, as shown in (Figure 4), PC also had an inferior performance if compared with its fiber counterparts, losing 8%

Figure 3 – Shrinkage strain versus time with de dominium of plastic and hardening states

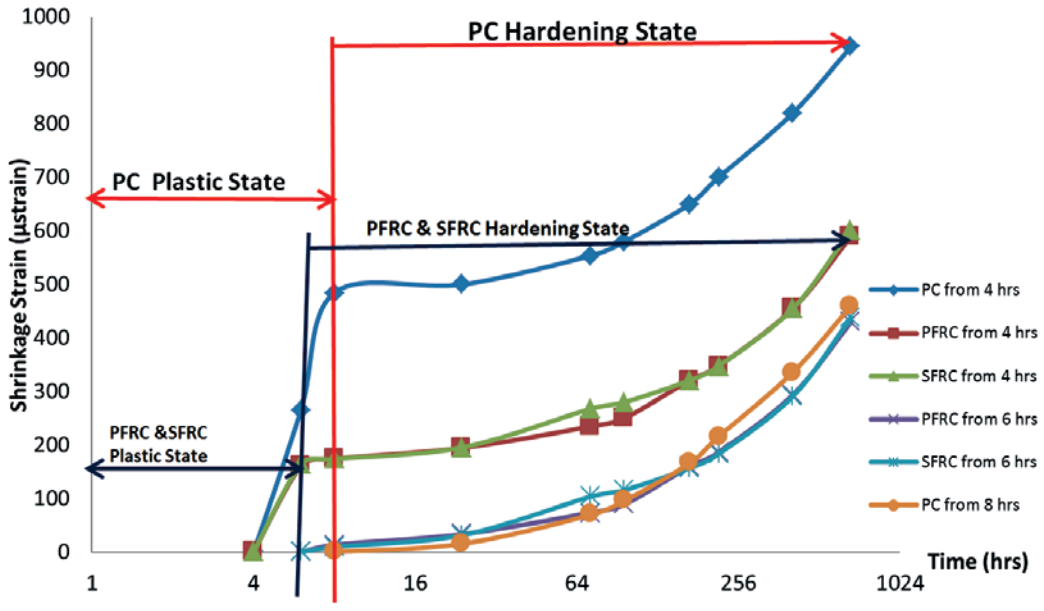

Figure 4 – Results of tests on shrinkage strain and loss of water of PC, SFRC and PFRC

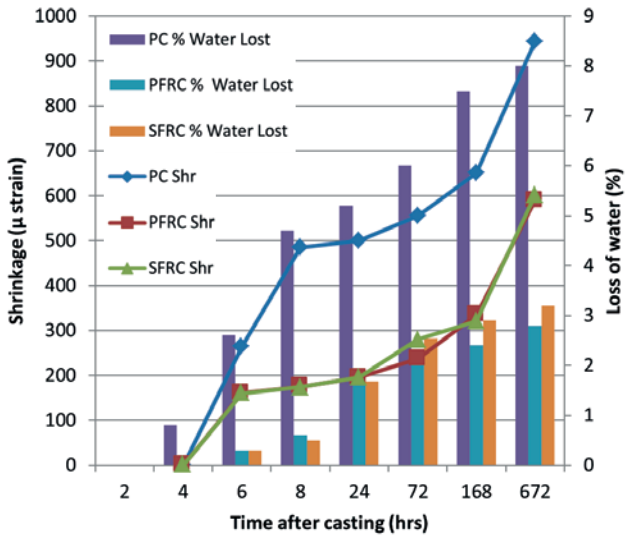

of its initial moisture content, while PFRC and SFRC lost 2.8% and 3.2 % respectively, during the same period of time. It can also be observed at Figure 4 that the PFRC and SFRC lost 0.6% and 0.5 % respectively of its initial moisture content during the first 8 hours after casting, which is a minor quantity if compared with the 4.7 % lost by PC in the same period. This period of time can be associated with the phase of the most vigorous plastic shrinkage at PC, as described on the previous paragraph. Most of the water lost by PFRC and SFRC happened during the hardened phase (2.2% and 2.3 % respectively), while PC lost a great quantity of water (4.7%) during its plastic phase and 3.3 % on its hardening. Therefore, after 8 hours of age, in the hardening state, all mixes lose water in a similar manner (Figure 4), developed similar shrinkage strain rates (Figure 3), and similar compressive strengths (Table 2).

Therefore, the fibers provided an effective mechanism to inhibit exudation and segregation during the plastic phase, by accumulating water on its surface by adsorption, resulting on both, lower shrinkage and loss of water than PC, of around 1/3 of what PC presented. Polypropylene fibers performed better than steel fibers because even PFRC having slightly higher moist content than SFRC, it still retained more water than SFRC and developed smaller shrinkage than SFRC. This can be regarded to its long length and large surface area. Such facts justify the use of fibers, and can clearly demonstrated that while plastic shrinkage prevailed, the fibers were highly effective to adsorb water impeding the movements of water in the paste, diminishing evaporation during the plastic state.

Also based on Cusson [8] the called *"time zero"* to identify at which time shrinkage can cause stresses, it could be assumed that it corresponds to the initial time of the "*hardening state"* at Figure 3. For PFRC and SFRC this time can be 6 hours and to PC corresponds to 8 hours; and the shrinkage which happened before this time can be disregarded for shrinkage stress calculation, in a restrained element.

4. Conclusions

Both, Polypropylene and Steel fibers, presented effective performances on reducing plastic shrinkage in comparison with the plain control mix. It was clearly demonstrated that shrinkage is closely related to the loss of water, as PC lost 3 times more water during the first 28 days of age than PFRC and SFRC. Also PC achieved the highest shrinkage strain of 944 μstrain, while PFRC and SFRC achieved 36% less shrinkage during this same period of time.

When the hardening state started, all mixes attained similar shrinkage strains and lose water in similar rates, demonstrating that fibers were effective on impeding the loss of water during the plastic state, but were not as effective after this phase.

PFRC had a slightly superior performance when compared with SFRC with regard to reduction of shrinkage, loss of water and compressive strength during the plastic phase. It could be observed that indeed fibers seem to accelerate setting, which is a topic to be explored in future.

It is also possible to identify the plastic and hardening phases of concrete on the shrinkage strain curves tested from early ages. The plastic phase coincides with the steep part of such curves; and the hardening phase is the region of the curve where it becomes steady with lower increases rates of strains. This is only possible to obtain when shrinkage tests start at very early ages.

Finally, it can be seen from the above that the method of separating the volume fraction of paste from a mix; weighing the samples from very early ages and crossing its values with the shrinkage measured at the same period of time, showed to be effective to a better understanding of the phenomenon of shrinkage to identify its plastic and hardening phases.

5. Acknowledgements

- CAPES – Coordination on Improvement of Academic Personnel/Brazil, for the financial support for the first author.
- The experimental program was carried out at the Laboratory of Concrete of School of Civil and Environmental Engineering, UNSW- The University of New South Wales, Sydney, Australia under the supervision of Dr. N. Gowripalan.

6. References

[01] NEVILLE, A.M Properties of Concrete, 4th Edition, Longman Group Limited, London, UK, 844 p, 1995.

[02] BANTHIA, N., and GUPTA, R. "Influence of Polypropylene fiber geometry on plastic shrinkage cracking in concrete", Cement and Concrete Research, 36, pp. 1263-1267, 2006.

[03] MELBYE, T.A. Sprayed Concrete for Rock Support, 5th Edition, Copyright MBT International Underground Construction Group, Division of MBT (Switzerland) Ltd., 1996, 188 p.

[04] ONGHERO, L. and REPETTE, W.L. "O efeito de diferentes teores de aditivo redutor de retração na reologia de pastas de cimento auto-adensáveis", Anais do 52º Congresso Brasileiro do Concreto CBC 2010, IBRACON, 2010

[05] GOWRIPALAN, N. "Basic fibre theory, fibre types and current trends", Fibres in Concrete 97 –Seminar, Edited by Cement and Concrete Association of Australia, Australia, pp. 1-32, 1997.

[06] TANESI, J. and FIGUEIREDO, A. D. “Fissuração por retração em concretos reforçados com fibras de polipropileno (CRFP)”, Boletim Técnico- Série BT/PCC , Escola Politécnica de São Paulo, 1999.
[07] FIGUEIREDO, A. D. Concreto Reforçado com Fibras , Tese de Livre Docência, Escola Politécnica da Universidade de São Paulo, São Paulo, 247 pp, 2011.
[08] CUSSON, D. and HOOGEVEEN, T, “An experimental approach for the analysis of early-age behavior of high-performance concrete structures under restrained shrinkage”, Cement and Concrete Research, 37, pp. 200-209, 2007.
[09] MINDESS, S., YOUNG, J.F., and DARWIN, D. Concrete, Prentice Hall 2003, 644 pp, 2003.

Volume 8, Number 1 (February 2015) p. 14-24 • ISSN 1983-4195

REVISTA IBRACON DE ESTRUTURAS E MATERIAIS

IBRACON STRUCTURES AND MATERIALS JOURNAL

Mineral processing and characterization of coal waste to be used as fine aggregates for concrete paving blocks

Processamento mineral e caracterização de rejeito de carvão mineral para produção de blocos de concreto para pavimentação

C. R. SANTOS [a]
cassiano_eng@hotmail.com

R. M. C.TUBINO [a]
rejane.tubino@ufrgs.br

I. A. H. SCHNEIDER [a]
ivo.andre@ufrgs.br

Abstract

Commercial coal production in the southern region of Brazil has been occurring since the beginning of the twentieth century. Due to the geological characteristics of the region, large amounts of solid wastes are generated. The aim of this work was to evaluate the use of coal waste to produce concrete paving blocks. A procedure to process the coal waste with the purpose of reducing the sulfur content and changing the particle size distribution of the material to meet the specification of fine aggregates was developed. The methodology considered the following steps: (a) sampling of a coal mining waste; (b) gravity separation of the fraction with specific gravity between 2.4 and 2.8; (c) comminution of the material and particle size analysis; (d) technological characterization of the material and production of concrete paving blocks; and (e) acidity generation prediction (environmental feasibility). The results showed that the coal waste considered in this work can be used to replace conventional sand as a fine aggregate for concrete paving blocks in a proportion of up to 50%. This practice can result in cleaner coal production and reduce the demand for exploitation of sand deposits.

Keywords: coal waste, environment, fine aggregate, concrete, paving.

Resumo

A produção de carvão mineral na região sul do Brasil vem ocorrendo desde o início do século XX. Devido às características geológicas da região, grandes quantidades de resíduos sólidos são gerados. O objetivo deste trabalho foi avaliar a utilização de rejeito de carvão para a produção de blocos de pavimentação de concreto. O rejeito de carvão foi beneficiado com o objetivo de reduzir o teor de enxofre e ajustar o tamanho das partículas do material para as especificações de distribuição granulométrica de agregado miúdo. A metodologia considerou os seguintes passos: (a) amostragem do rejeito de carvão mineral; (b) separação gravimétrica da fração com densidade entre 2,4 e 2,8; (c) cominuição do material e análise da distribuição granulométrica; (d) caracterização tecnológica do material e produção de blocos de concreto para pavimentação; e (e) predição da geração de acidez (viabilidade ambiental). Os resultados mostraram que o rejeito de carvão utilizado neste trabalho pode ser utilizado para substituir a areia convencional como um agregado miúdo na produção de blocos de concreto para pavimentação numa proporção de até 50%. Esta prática pode colaborar com a produção mais limpa de carvão mineral e reduzir a demanda de exploração de jazidas de areia.

Palavras-chave: rejeito de carvão mineral, meio ambiente, agregado miúdo, concreto, pavimentação.

[a] *Programa de Pós-Graduação em Engenharia de Minas, Metalúrgica e de Materiais, Universidade Federal do Rio Grande do Sul, Porto Alegre, RS, Brasil.*

Received: 18 Jan 2013 • Accepted: 20 Nov 2014 • Available Online: 03 Feb 2014

1. Introduction

Commercial coal production in the southern region of Brazil (comprising the Paraná, Santa Catarina, and Rio Grande do Sul states) has been occurring since the beginning of the twentieth century. Specifically in the Santa Catarina State, the production occurs at the "Irapuá", "Bonito", and mainly "Barro Branco" seams. These Gondwanic coals are classified for the major part as a high-volatile bituminous in rank. The thickness of the Barro Branco seam ranges from 1.66 to 2.27 m, with an average value of 1.80 m. However, net clean coal thickness is reduced to 0.47–1.48 m, due to the presence of alternating layers of impure coal (shaley coal and coaly shale), carbonaceous shale, siltstone, and sandstones. Pyrite lenses that are several centimeters thick are also common [1]. Currently, the run-of-mine coal (ROM) is gravimetrically concentrated and almost entirely used for electricity generation. Due to the geological characteristics of the region, large amounts of solid wastes are generated. It is estimated that more than 300 million metric tons of coal waste exist in the south of Brazil, generating environmental impacts and economic costs. Regarding the Santa Catarina Coalfields, about 60%–65% of the ROM coal is discharged at dump deposits as waste [2]. These wastes can lead to the formation of acid mine drainage (AMD), a source of groundwater and surface water pollution [3].

Through gravity concentration processes of coal waste from Barro Branco seam, it is possible to produce three output streams: (i) a low-specific-gravity material composed of shaley coal and carbonaceous shale; (ii) an intermediate material composed of siltstone and sandstone; and (iii) a high-specific-gravity material that is rich in pyrite. Presently, there are some initiatives in Brazil to reprocess some coal waste deposits to recover part of the carbonaceous materials for energy production and, alternatively, to concentrate the pyrite for sulfuric acid production. However, the intermediate-density material still remains, which represents 50%–60% in mass of the coal waste deposit and can be considered as a material for possible use in civil construction [4]. Mining wastes has been considered worldwide as a material for aggregate production [5,6,7], including coal wastes (colliery spoil) [8].

Concrete paving blocks can be used in a large range of applications. The conventional source of fine aggregates for paving blocks are river sand or, alternatively, artificial sand obtained by crushing rocks [9]. However, previous research has shown that it is possible to use some wastes to produce concrete paving blocks, for example, gasification residues [10], construction and demolition waste [11,12], ceramic tile production wastes [13], marble production wastes [14], recycled glass [15], polypropylene fiber [16], crushed brick [17], electric-arc furnace dust [18], red mud [19], and fly ash [19].

According to the Brazilian standard NBR 9781 [20], the compression resistance of concrete blocks for paving should meet the minimum of 35 MPa for pedestrian and commercial vehicles and 50 MPa for heavy-duty vehicles. The same limit of 35 MPa is used by Thailand [21]. Other countries allow lower resistances, like India (30 MPa) [22], Sri Lanka (15 MPa for pedestrians) [23], and Indonesia (20 MPa) [24], or require higher resistances, like USA (55.2 MPa) [25] and UK (49 MPa) [26].

Thus, the aim of this work was to study the use of coal waste to produce concrete blocks for paving. A procedure to process the coal waste with the purpose of reducing the sulfur content and changing the particle size distribution of the material to meet the specification for fine aggregates was developed. Additionally, the coal waste aggregate was characterized in terms of its chemical and physical properties. The article evaluates the main technical and environmental parameters that are involved in recycling part of the coal waste and aimed at turning it into a useful product.

2. Materials and experimental program

Coal waste was collected from the coal dump deposit of the "Verdinho mine," Santa Catarina State, Brazil, which extracts the Barro Branco seam. The material was submitted to a laboratory dense medium separation processing, using organic liquids, which aimed at obtaining a fraction with relative density between 2.4 and 2.8 [27]. This fraction was crushed in a roller mill and sieved to reach the particle size distribution required for fine aggregates in concrete, according to NBR 7211 [28]. The mineral-processing steps to produce the coal waste fine aggregate from coal mining tailings are presented in Figure 1.

Quartz river sand was obtained from Jacuí River, Rio Grande do Sul State. Technological characterization of both materials included particle size distribution, density measurements, visual observation in a petrographic magnifying lens, and mineral phase determination by x-ray diffraction. Determination of sulfate and chloride ions was conducted following the procedure

Figure 1 – Mineral-processing steps to produce coal waste fine aggregate from coal mining tailings

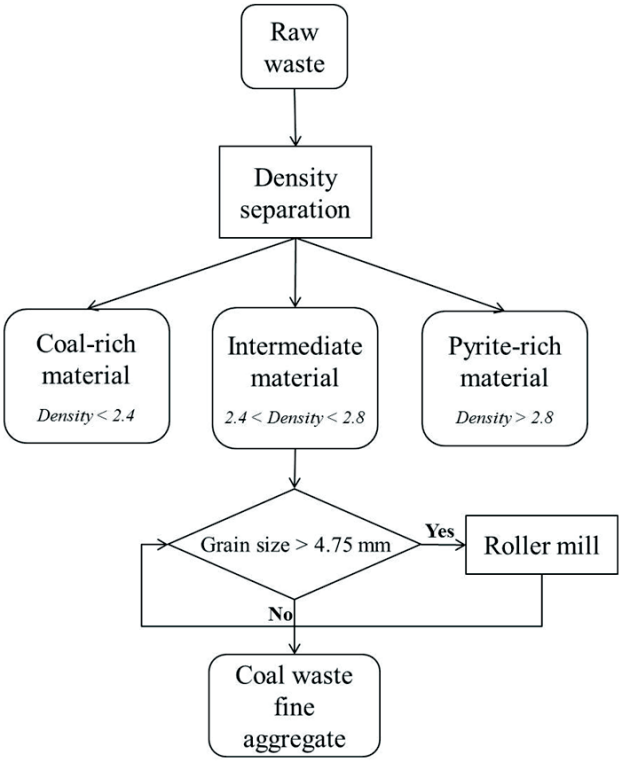

Table 1 – Properties of conventional quartz sand aggregates and the coal waste fine aggregate

Property	Conventional river sand aggregate	Coal waste fine aggregate
Density (kg/dm³)		
Real	2.6	2.3
Apparent	1.6	1.3
Particle shape	Rounded and subrounded	Angular
Mineralogical composition	Quartz – SiO_2 (major mineral phase)	Quartz – SiO_2 (major mineral phase), kaolinite - $Al_4(OH)_8(Si_4O_{10})$, illite - $(K,H_3O)(Al,Mg,Fe)_2(Si,Al)_4O_{10}((OH)_2,(H_2O))$, andgypsum - $CaSO_4.2H_2O$
Sulfate ions (% of SO_4^{2-})	ND	1.00
Chloride ions (% of Cl^-)	ND	ND
Elemental composition (%)		
C	ND	2.6
H	ND	0.8
N	ND	0.1
S	ND	1.9
Si	63.7	47.0
Fe	1.0	7.5
Al	1.7	14.0
Mn	0.03	0.2
Ca	0.4	4.2
K	3.1	5.5

ND – not detected

described in NBR 9917 [29]. Elemental analyses of the fine aggregates were carried out by x-ray fluorescence (for Si, Fe, Al, Ca, and K) and high-temperature decomposition in a CHNS analyzer (for C, H, N, and S). The main characteristics of both materials are summarized in Table 1.

Concrete paving blocks were produced in a vertical shaft concrete mixer. The reference trace used 5.36 kg of cement (CP-V-ARI-RS), 6.26 kg of coarse granitic aggregate, 14.18 kg of river sand aggregate, and a water/cement ratio of 0.35. Chemical properties of the cement are presented in Table 2. Coal waste was used as a substitute for river sand aggregate, considering the following volumetric levels of substitution: 0%, 25%, 50%, 75%, and 100%. For each level of substitution, the water/cement ratio was reestablished to provide the same consistency of concrete [30]. The concrete blocks were molded in manual press equipment with a production capacity of six blocks per cycle. The blocks were molded in the "unipaver" shape with the following dimensions: 22.5 cm length, 12.0 cm width, and 8 cm height (Figure 2). The technological characterization of the paving blocks included resistance to compression, abrasion resistance and water absorption. It was produced 90 blocks for compression resistance, 10 blocks for abrasion resistance, and 10 blocks for water absorption tests. The results of compression resistance are the average of six test results (n= 6 for each level of substitution and each curing period) and the curing periods were 7, 28, and 90 days. Abrasion resistance and water absorption were carried out in two concrete blocks (n=2) resulting from each level of substitution at a curing period of 28 days. The effect of the experimental parameters on these properties was

Table 2 – Chemical properties of the cement

Compounds	% weight
SiO_3	25.12
Al_2O_3	7.31
Fe_2O_3	3.47
CaO	53.21
MgO	6.12
K_2O	1.47
Na_2O	0.05
SO_3	2.59
CO_2	2.38

evaluated statistically by using analysis of variance (ANOVA, significance level of 95%) and the Tukey test.

Compression resistance and water absorption were carried out in accordance with the Brazilian Standard Procedures NBR 9780 [31] and NBR 9778 [32], respectively. Abrasion resistance was determined according to the CIENTEC method. The procedure consists of dividing a paving block specimen into two pieces with a diamond saw. Each piece is placed to a rotatory machineand submitted to a constant pressure of 0.06 MPa in the presence of an abrasive powder (silicon carbide). The aim is to simulate a pathway of 500 m. The width of the paving block was measured before and after the experiment in five positions of each paving block piece. The wear rate result, expressed in millimeters, is the mean of 10 measurements.

The acid generation potential of the raw waste, coal waste fine aggregates, and blocks with 25% and 50% substitution of river sand by coal waste fine aggregate at 28 days was measured by the traditional method of accounting for acids and bases (ABA) [33]. The objective was to determine the balance between the minerals that produce acidity (acidity potential - AP) and the minerals that consume acidity (neutralization potential - NP). The determination of acidity potential (AP) was carried out from the analysis of total sulfur using a CHNS analyzer. AP was calculated by the following conversion factor:

$$AP = 31.25 \times \%S \quad (1)$$

To determine the neutralizing potential (NP), the procedure consisted of subjecting the sample to an acidic solution followed by titration of the acid solution with sodium hydroxide (with the same concentration as that of the acid) to pH 7.0. The net neutralization potential (NNP) was calculated from the difference between NP and AP:

$$NNP = NP - AP \quad (2)$$

A sample is classified as acid forming when it has NNP values less than -20 $CaCO_3$/t and non-acid forming when it has NNP values greater than +20 $CaCO_3$/t. Samples are classified as uncertain when their values range from -20 to +20 $CaCO_3$/t.

A kinetic test in humidity cells following the ASTM D 5744-96 [34] method was carried out to evaluate the chemical stability of the samples. The test consisted of placing 500 g of the material, with particle size between 6.3 mm and 2.0 mm, in a column with an internal diameter of 5 cm and a height of 30 cm. The test was carried out with the raw waste, coal waste fine aggregate, reference block, and block with 50% substitution of river sand by coal waste fine aggregate. During the seven-day cycle, dry air was passed through the column for the first three days and humidified air for the next three days. On the seventh day, the sample was rinsed with 500 mL of distilled water. The leachate was collected and analyzed for the AMD typical parameters: pH, Eh, acidity, alkalinity, concentration of metals (Fe, Al, Mn, Zn, and Ca), and concentration of sulfate. The procedures followed the Standard Methods for the Examination of Water and Wastewater [35] and the results were expressed in terms of average values of twenty weeks (n=20).

Figure 2 – Concrete paving blocks produced with varied levels of substitution

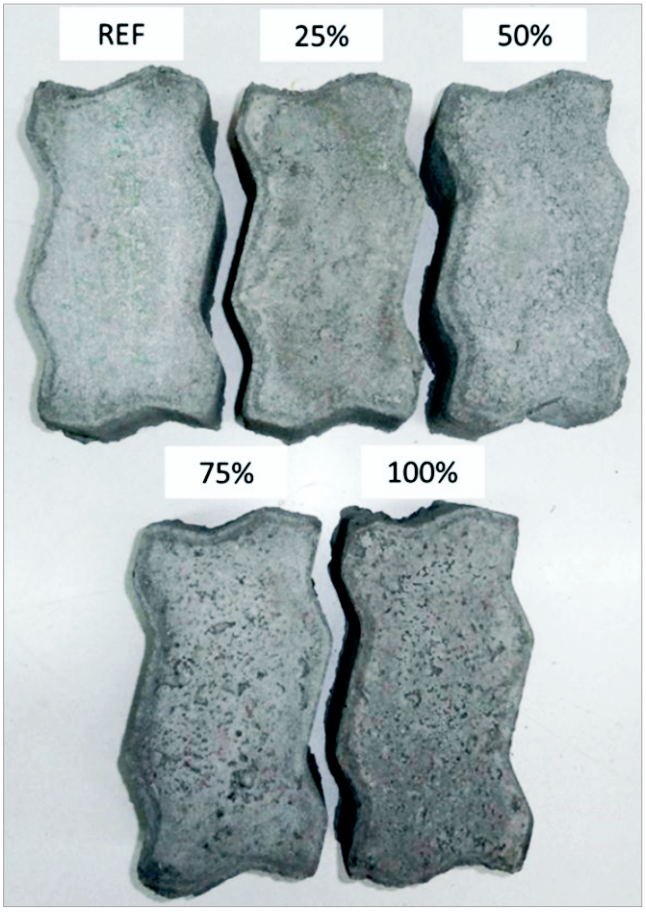

3. Results and discussion

Figure 3 presents particle size distribution of the coal waste fine aggregate as well as the river sand. Both materials have their size distribution from 0.15 to 4.0 mm. However, the D_{50} (grain diameter at which 50% of the mass sample is retained or passed by the sieve) of the coal waste fine aggregate was 0.4 mm and the D_{50} of the river sand was 1.0 mm. So, compared to the river sand used in this work the coal waste fine aggregate has a higher amount of finer particles. It can be also observed that both materials, separately, fit in the applicable zone, but not completely in optimal zone. However, the mixture composed by 50% coal waste and 50% river sand allows a particle size distribution entirely inside the optimal zone as prescribed by NBR 7211 [28].

The x-ray pattern of coal waste and the river sand applied in this work are depicted in Figure 4. The mineral fine aggregates produced from the coal waste have quartz as their major crystalline

phase. The presence of kaolinite, illite, and gypsum was also detected as well as amorphous components. River sand aggregate is basically composed of quartz. The particles of coal waste are angular in shape, due to the rock fragmentation procedure, and grayish in color. In contrast, river sand particles are rounded/subrounded and yellowish in color (Figure 5).

The concentration of sulfate ions in the fine coal aggregate was determined to be 1.00%, whereas in the river sand it were not detected (<0.01%). Chloride ions were not detected in fine coal aggregate and river sand. Sulfate is considered to be harmful for concretes, and it is recommended that the values of sulfates and sulfides in aggregates for concrete production should not exceed the value of 1% (mass) [36,37]. The concentration of sulfates was sufficiently low to be used for paving blocks production. However, the concentration of total sulfur was determined as 1.9%. Thus, for safety reasons, the fine aggregate produced from coal tailings should be applied in levels of river sand substitution of no more than 25% or 50%.

The preparation of concrete with coal waste in all levels of substitution was simple. Coal waste particles mixed properly with river sand and allowed a mixture without sights of bleeding and segregation. However, increasing the amount of coal waste particles in the fine aggregate, more water was necessary to maintain the same consistency of fresh concrete. It was expected because coal waste particles are more angular in shape and smaller in size. Table 3 shows the main technological properties of concrete blocks for paving, while considering the different levels of substitution. It is possible to observe that, increasing the level of substitution, there is an increase in the water/cement ratio and a decrease in the cement consumption. It can be observed that concrete blocks produced with substitution levels of 25% and 50%, at 28 days, statistically present behavior similar to the reference blocks (0% substitution) in terms of compressive resistance, abrasion resistance, and water absorption.

In terms of compression resistance, most of the blocks manufactured with 0%, 25% and 50% substitution attained the minimum value of 35 MPa established by NBR 9781 [20] for commercial standard vehicles. The blocks produced with substitution levels of 75% and 100% did not reach the required compression resistance. The loss in compression resistance in paving blocks with increasing levels of substitution of river sand by alternative aggregates has been observed in other situations, including crushed clay brick [11], ceramic tile waste [13], waste marble [14], and demolition materials [12]. It was also observed a small decrease, but statistically significant, in compression resistance from 28 to 90 days in the paving blocks with any amount of coal waste.

Increasing the level of substitution the abrasion resistance decreases. However, according to statistical analysis, the results were the same for the levels of substitution of 0%, 25%, 50%, and 75%. Blocks with 100% substitution of river sand presented significant difference compared to the others and, therefore, unsatisfactory results. Waste utilization in concrete production can be beneficial or harmful to abrasion resistance. The use of Class F fly ash [38], waste foundry sand [39], ceramic sanitary ware waste

Figure 3 – Size particle distribution of raw coal waste, coal waste fine aggregate, river sand, and the mixture of sand/coal waste fine aggregate (50%) as well the lower and upper limits described by NBR 7211(ZUI and ZUS are, respectively, the lower and the upper limits of the applicable zone, and ZOI and ZOS are the lower and the upper limits of the optimal zone)

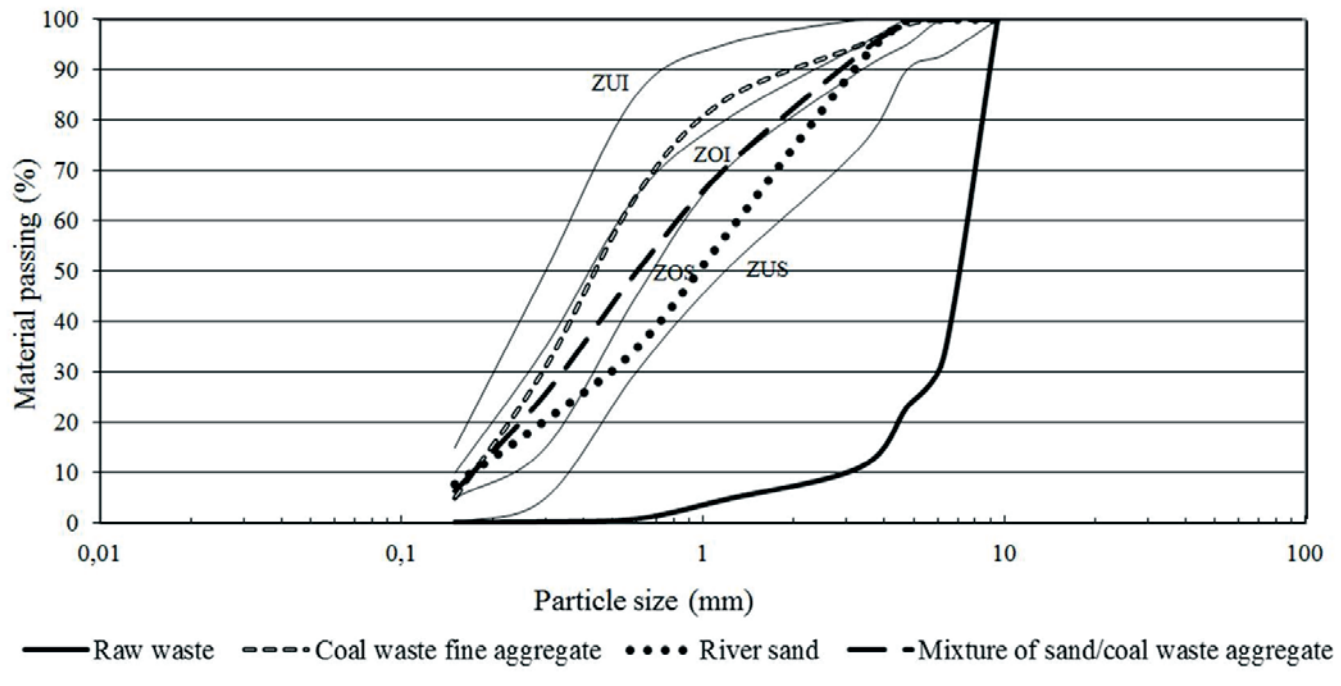

[40] and shredded PET bottle waste [41] increased abrasion resistance while fly ash [42,43,44] and bottom ash [45] decreased abrasion resistance.

In terms of water absorption, it was observed an increase with the substitution of river sand by coal waste. However, the increase of water absorption for blocks with 25% to 50% coal waste is very low. The values of water absorption in reference blocks and with levels of substitution of 0%, 25% and 50% are statistically the same while blocks with levels of substitution of 75% and 100% are statistically different. The same behavior was observed when using bottom ash [45] and recycled fine aggregates from construction and demolition waste [46]. However,

Figure 4 – X-ray diffraction patterns of coal waste fine aggregate and river sand

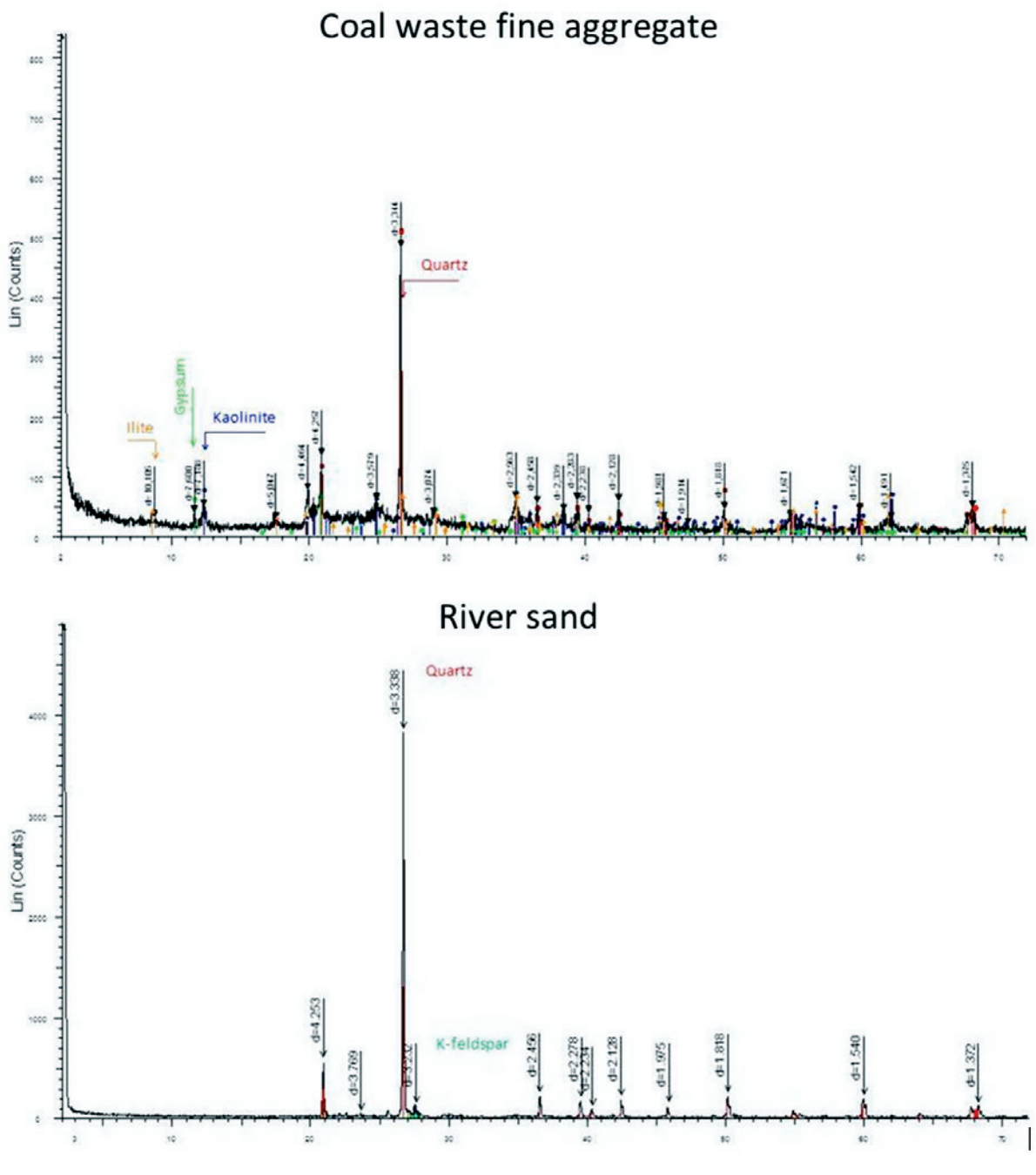

Figure 5 – Pictures showing the morphological characteristics of coal waste fine aggregate and river sand

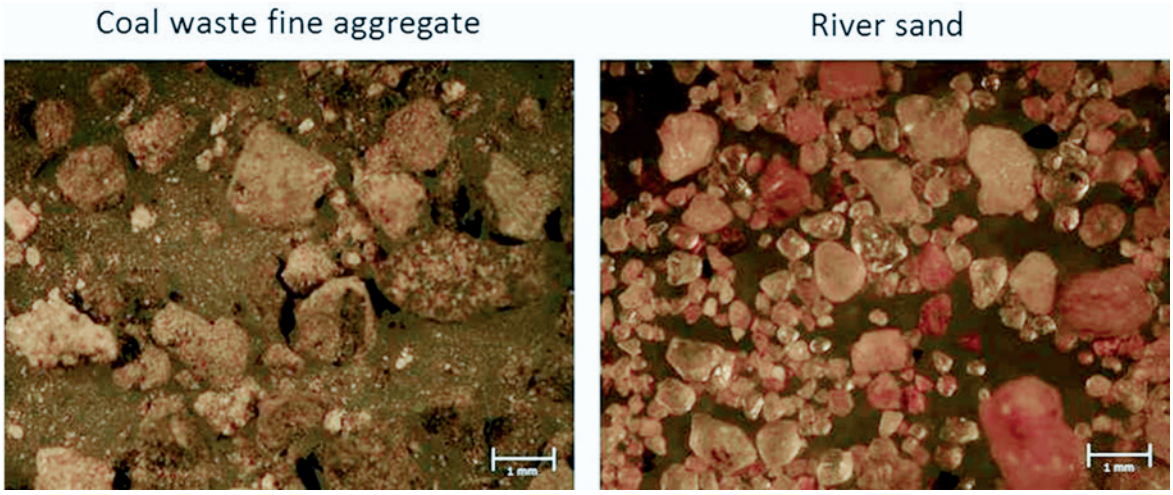

the opposite effect was observed in marble aggregates [47] and slag aggregate [48].

With respect to acid generation (Table 4), the material collected from the coal waste deposit presents a high sulfur content of 7.0%. The result is an AP of 218.8 kg $CaCO_3$/t, a NP of 0.0 kg $CaCO_3$/t, and a NNP of -218.8 kg $CaCO_3$/t. The fraction used for fine aggregate production, with a density between 2.4 and 2.8, exhibited a reduced acid generation potential, with a sulfur content of 1.9%, an AP of 60.8 kg $CaCO_3$/t, a NP of 0.0 kg $CaCO_3$/t, and a NNP of -60.8 $CaCO_3$/t. The paving blocks produced with 25% and 50% substitution of river sand by coal waste fine aggregate presented a NNP that was positive and higher than 400 kg $CaCO_3$/t. These results showed that the manufacture of paving blocks provided an alkaline environment and prevented acid generation.

A twenty weeks period test in humidity cells was carried out to confirm this. It can be observed in Figure 6 that the raw waste and the coal waste fine aggregate generate an acid leach. The pH ranged from 3.3 to 1.3 for the raw waste and from 4.0 to 2.6 for the coal waste fine aggregate. For the concrete blocks, in all situations, the water pH remained neutral or slightly alkaline, with the following pH ranges: 11.8 and 8.3 for the reference blocks and 10.3 and 7.0 for blocks with 50% substitution. These results confirm that the procedure of separation of the material rich in pyrite, followed by the encapsulation of the fine aggregate in a concrete matrix, is a

Table 3 – Properties of the concrete blocks for paving

Property	Substitution				
	0 %	25 %	50 %	75 %	100 %
Water/cement ratio	0.35	0.37	0.39	0.43	0.44
Cement consumption (kg/m³)	483.4	477.3	472.5	465.1	461.9
Elemental composition (%)					
7 days	28.1 ± 2.8[a]	33.0 ± 3.4[b]	34.2 ± 1.3[b]	28.3 ± 1.6[a]	24.8 ± 4.6[a]
28 days	39.5 ± 2.9[a]	37.6 ± 1.6[a]	36.6 ± 1.4[a]	31.2 ± 2.7[b]	27.3 ± 3.1[b]
90 days	40.7 ± 0.3[a]	36.2 ± 5.3[b]	34.1 ± 4.4 [b]	29.0 ± 3.8[c]	27.2 ± 4.8[c]
Abrasion resistance (mm) 28 days	6.6 ± 0.0[a]	7.5 ± 1.3[a]	7.9 ± 0.0[a]	8.1 ± 0.5[a]	11.44 ± 3.0[b]
Water absorption (%) 28 days	4.9 ± 0.0[a]	5.3 ± 0.1[a]	5.4 ± 0.0[a]	6.9 ± 0.6[b]	8.0 ± 0.8[c]
Mass of fine aggregate of coal waste consumed per m² of pavement (kg)	0.0	12.1	24.2	36.4	48.5

Average ± standard deviation.

Values with the same superscript letters compared horizontally do not differ significantly from each other.

Table 4 – Acid generation prediction results of the raw waste, coal waste fine aggregate, and concrete paving blocks with 0%, 25%, and 50% of substitution of river sand by the coal waste fine aggregate

Parameter	Raw coal waste	Coal waste fine aggregate	Concrete paving blocks		
			0% substitution	25% substitution	50% substitution
Total S (%)	7.0	1.9	0.5	0.4	0.9
AP (kg $CaCO_3$/t)	218.8	60.8	15.7	12.2	27.5
NP (kg $CaCO_3$/t)	0.0	0.0	241.0	430.0	488.2
NNP	-218.8	- 60.8	225.3	417.8	460.7
Formation of AMD	Yes	Yes	No	No	No

successful procedure to avoid acid generation. The encapsulation of some remaining pyrite grains into the paving blocks avoids their contact with atmospheric oxygen and water, inhibiting pyrite oxidation reactions. Table 5 presents the average values of chemical parameters analyzed on the leachate considering raw coal waste particles, coal waste fine aggregate, paving blocks with 50% substitution, and reference paving blocks (100% river sand). The leachate of raw coal waste has a low pH and a very high concentration of metals and sulfates. This is what happens in sulfide mining sites and it is typically named “acid rock drainage”. The procedure applied to prepare the coal waste fine aggregate by density separation, allowed to reduce in 73% the concentration of pyritic sulfur. So, in this case, the leachates were less intense in terms of medium acidification and the release of metals and sulfate. Incorporating the coal waste in concrete in a proportion of 50%, acidification was avoided as well the metal leaching. Comparing the leached water of the concrete produced with 100% river sand with the concrete produced with coal waste in a level of 50% substitution, the results were quite similar. However, in the latter was observed a higher amount of calcium and sulfates. Calcium and sulfate leaching can generate empty spaces in concrete structure, and therefore affect adversely compression resistance in long term.

Analyzing the results, coal waste brings benefits to adjust the particles size of the fine aggregates and the presence of quartz as the major crystalline phase reinforces coal waste as an inert material with weak potential for hydraulic activity. However, the presence of the amorphous phase as well as the minerals kaolinite, illite, gypsum, and pyrite (even at low concentrations) could affect the

Figure 6 – pH values of the leachate from the humidity cells containing raw waste, coal waste fine aggregate, and concrete paving blocks (containing 0% and 50% of coal waste aggregate replacing natural sand)

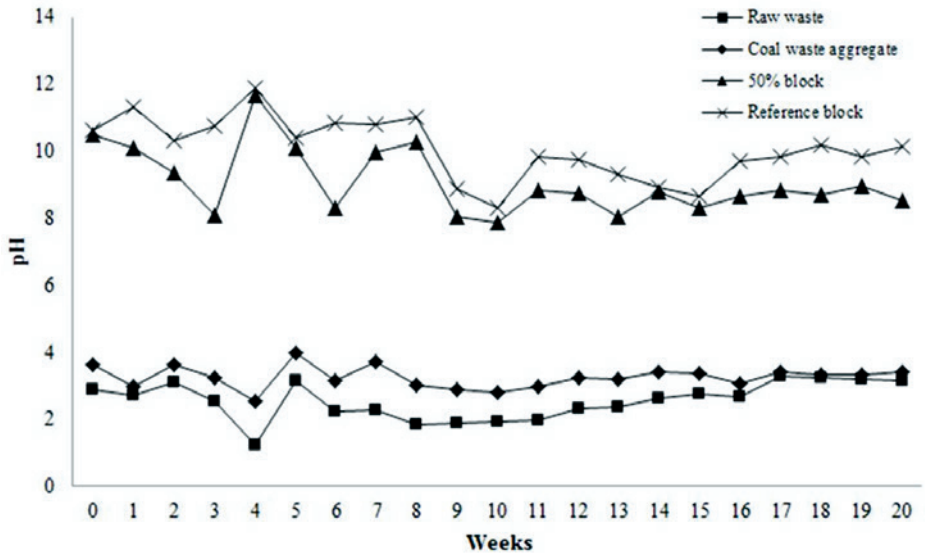

Table 5 – Average values of parameters analyzed along the kinetic test in humidity cells (n=20)

Parameter	Unit	Raw coal waste	Coal waste fine aggregate	50% substitution block	0% substitution block
pH	–	2.5	3.2	9.0	10.0
Eh	mV	721	682	443	417
Acidity	mg/kg $CaCO_3$	3542	186	9.9	4.0
Alkalinity	mg/kg $CaCO_3$	0	0	211	384
Fe	mg/L	290.8	8.2	1.1	1.6
Al	mg/L	37.5	8.8	2.7	3.4
Mn	mg/L	1.65	2.05	0.006	0.001
Zn	mg/L	0.201	0.176	0.013	0.008
Ca	mg/L	56	58	97	53
Sulfate	mg/L	1808	312	248	94

long-term behavior of the paving blocks. The amorphous structure can lead to alkali-aggregate reactivity causing expansion of the aggregate in hardened concrete structure [30]. Illite can also cause expansion and cracking of concretes in such a manner that appeared analogous to alkali-silica reactivity. Expansion by illite was suggested to occur by swelling and followed by de-dolomitisation by the cement alkalis [49]. Gypsum presence in aggregates can produce false set in freshly mixed concrete and pyrite can oxidize and release sulfates. Sulfates can react after the concrete has hardened, causing expansion and cracking [30,50,51]. As mentioned before, the same water/cement ratio used in reference concrete could not be kept in concrete produced with coal waste fine aggregate. The presence of clays in a cement mixture reduces the amount of water available for the hydration reactions, decreases its workability, and alters the course of the pozzolanic reactions [52,53,54]. Problems with increased water demand with clay minerals including kaolinite and illite were observed in other works [55,56]. These comments are in agreement with other studies about coal waste (colliery spoils) as aggregates for concrete production. Those studies highlighted excessive wear, expansive behavior and pyrite oxidation as the main drawbacks for its use as aggregate in civil construction [7,8]. Kinnuthia et al. applied colliery spoil as fine and coarse aggregates in low and medium strength concretes [8].

Finally, with a level of substitution of 25% the demand of coal waste fine aggregate was estimated to be 12.1 kg/m^2 of paved area. Considering a run-of-mine coal production of 40,000 t, 60% of the material is discharged as waste, and 50% of this fraction is separated between the relative densities of 2.4 and 2.8, it is possible to produce about 12,000 t of fine aggregates, which is sufficient to attend a paved area of about 1 km^2.

4. Conclusion

The results showed that it was possible to process the coal waste from the carboniferous region of Santa Catarina and obtain a recycled fine aggregate that can be used in civil construction. The waste material should be submitted to a gravity separation process (with cut densities between 2.4 and 2.8 to remove the carbonaceous and pyritic fractions), which is followed by crushing in a roll mill. The material, composed mainly of siltstone and sandstone, presented a low concentration of sulfur, about 1% of sulfate, and a particle size distribution that met the specification for fine aggregates. Concrete blocks for paving produced with 25% and 50% of recycled coal waste, substituted for river sand, presented satisfactory results in terms of compression resistance. The use of coal waste as a fine aggregate for concrete block paving manufacture presents technical viability and environmental benefits. The demand for sand deposits can be minimized and a part of the coal tailings can be used, reducing the volume in coal waste deposits. We believe that this procedure can be applied to minimize the environmental problems posed by coal production in Brazil.

5. Acknowledgments

The authors are grateful for the financial support extended by FINEP, CAPES, CNPq, and the Brazilian Coal Network for this research.

6. References

[01] Kalkreuth, W., Holz, M., Mexias, A., Balbinot, M., Levandowski, J., Willett, J., Finkelman, R., Burger, H., 2010. Depositional setting, petrology and chemistry of Permian coals from the Paraná Basin: 2. South Santa Catarina Coalfield, Brazil. International Journal of Coal Geology, 84, 213-236.

[02] ABCM (Associação Brasileira do Carvão Mineral), 2012. http://www.carvaomineral.com.br/abcm/conteudo/gm_estatisticas/estatisticas_2011.pdf. Accessed 23 October, 2012.

[03] Silva, R.D.R.; Rubio, J., 2009. Treatment of acid mine drainage (AMD) from coal mines in south Brazil. International Journal of Coal Preparation and Utilization 29, 192–202.

[04] Amaral Filho, J.R.; Schneider, I.A.H.; Brum, I.A.S.; Sampaio, C.H.; Miltzarek, G.; Schneider, C.H., 2013. Character-

ização de um depósito de rejeitos para o gerenciamento integrado dos resíduos de mineração na região carbonífera de Santa Catarina, Brazil. REM. Revista Escola de Minas, 66, p.347-353.

[05] Galpern, E.I.; Pashchenko, L.V.; Bratchun, V.I., 1998. Use of mine waste rock for civil engineering purposes. Proceedings of the fifth International Symposium on Environmental Issues and Waste Management in Energy and Mineral Production, Ankara, Turkey.

[06] Tohver, T., 2010. Utilization of waste rock from oil shale mining. Oil Shale, 27, 321–330.

[07] Nixon, P.J.; Gartner, E.M., 1980. An assessment of processes for the manufacture of synthetic aggregates from colliery spoil. International Journal of Cement Composites and Lightweight Concrete, 2, 141-164

[08] Kinuthia, J.; Snelson, D.; Gailius, A., 2009. Sustainable medium-strength concrete (CS-concrete) from colliery spoil in South Wales UK. Journal of Civil Engineering and Management, 15, 149-157.

[09] American Concrete Institute - ACI, "Aggregates for Concrete," Education Bulletin E1-07, Farmington Hills, 2007, p. 29.

[10] Holt, E.; Raivio, P., 2006. Use of gasification residues in compacted concrete paving blocks. Cement and Concrete Research, 36, 441-448.

[11] Poon, C. S.; Chan, D., 2006. Paving blocks made with recycled concrete aggregate and crushed clay brick. Construction and Building Materials, 20, 569–577.

[12] Soutsos, M.N.; Tang, K.; Millard, S.G., 2011. Use of recycled demolition aggregate in precast products, phase II: Concrete paving blocks. Construction and Building Materials, 25, 3131–3143.

[13] Wattanasiriwech, D.; Saiton, A.; Wattanasiriwech, S, 2009. Paving blocks from ceramic tile production waste. Journal of Cleaner Production, 17, 1663–1668.

[14] Gencel, O.; Ozel, C.; Koksal, F.; Erdogmus, E.; Martínez-Barrera, G.; Brostow, W., 2012. Properties of concrete paving blocks made with waste marble. Journal of Cleaner Production, 21, 62-70.

[15] Ling, T.C.; Poon, C.S., 2014. Use of recycled CRT funnel glass as fine aggregate in dry-mixed concrete paving blocks. Journal of Cleaner Production, 68, 209-215.

[16] Kashiyani, B.K.; Pitroda, J.; Shah, B.K., 2013. Innovative addition of polypropylene fibre in interlocking paver block to improve compressive strength. International Journal of Civil, Structural, Environmental and Infrastructure Engineering Research and Development, 3, 17-26.

[17] Jankovic, K.; Nikolic, D.; Bojovic, D., 2012. Concrete paving blocks and flags made with crushed brick as aggregate. Construction and Building Materials, 28, 659–663.

[18] Vargas, A.S.; Masuero, A.B.; Vilela, A.C.F., 2006. Investigations on the use of electric-arc furnace dust (EAFD) in pozzolan-modified Portland cement I (MP) pastes. Cement and Concrete Research, 36, 1833–1841

[19] Kumar, A.; Kumar, S., 2013. Development of paving blocks from synergistic use of red mud and fly ash using geopolymerization. Construction and Building Materials, 38, 865–871.

[20] ABNT – Associação Brasileira de Normas Técnicas NBR 9781. Peças de concreto para pavimentação – Especificação e métodos de ensaio. Rio de Janeiro, 2013.

[21] TISI Standard. Interlocking concrete paving blocks (TIS 827-2531 (1988)). Thai Industrial Standards Institute. 2003.

[22] IS 15658. Precast concrete blocks for paving. India: Bureau of Indian Standards; 2006.

[23] Sri Lanka Standards Institution, Draft Sri Lanka Standard, 'Specifications for concrete paving blocks: part 1: requirements', Sri Lanka Standards Institution. 2011.

[24] SNI 03 – 0691 -1989, Bata Beton Untuk Lantai, Standard Normalisasi Indonesia. 1989.

[25] ASTM C 936. Standard specification for solid concrete interlocking paving units.Masonry test methods and specifications for the building industry, 4th ed., American Society of Testing and Materials, 2001.

[26] BSI. BS 6717-1:1993 Precast, unreinforced concrete paving blocks – requirements and test methods. London: British Standards Institution (BSI); 1993.

[27] Leonard, J.W., 1991. Coal Preparation, 5th ed. Society for Mining, Metallurgy, and Exploration, Inc. Littleton, Colorado, USA.

[28] ABNT – Associação Brasileira de Normas Técnicas. NBR 7211. Agregados para Concreto, Rio de Janeiro. 2005.

[29] ABNT – Associação Brasileira de Normas Técnicas. NBR 9917. Agregados para concreto – Determinação de sais, cloretos e sulfatos solúveis, Rio de Janeiro. 2009.

[30] Mehta, P.K. and Monteiro, P.J.M, 1993. Concrete: Structure, Properties, and Materials, 2nd ed. Prentice-Hall, Englewood Cliffs, NJ, USA.

[31] ABNT – Associação Brasileira de Normas Técnicas. NBR 9780. Peças de concreto para pavimentação determinação da resistência à compressão - Método de ensaio, Rio de Janeiro. 1987.

[32] ABNT – Associação Brasileira de Normas Técnicas. NBR 9778. Argamassa e concreto endurecidos – Determinação da absorção de água, índice de vazios e massa específica – Método de ensaio, Rio de Janeiro. 2005.

[33] Environmental Protection Agency. EPA 530-R-94-036: Acid Mine Drainage Prediction., 1994. Technical document.

[34] American Society for testing and Material – ASTM. ASTM D 5744: Standard test method for accelerated weathering of solid materials using a modified humidity cell. USA, 1996.

[35] American Public Health Association (APHA), "Standard Methods for the Examination of Water and Wastewater," 21st Edition, APHA-AWWA-WEF, Washington DC, 2005.

[36] Mattus, C. H. and Gilliam, T. M. A Literature Review of Mixed Waste Components: Sensitivities and Effects upon Solidification/Stabilization in Cement-based Matrices. Oak Ridge National Laboratory, Martin Marietta Energy Systems, Inc, 1994. 118p.

[37] HRN.B.B2.010-86, Aggregate for concrete. Technical Requirements (in Croatian).

[38] Siddique, R., 2003. Effect of fine aggregate replacement with Class F fly ash on the abrasion resistance of concrete. Cement and Concrete Research, 33, 1877–1881.

[39] Singh, G.; Siddique, R., 2011. Effect of waste foundry sand (WFS) as partial replacement of sand on the strength, ultrasonic pulse velocity and permeability of concrete. Construction and Building Materials, 26, 416-422.

[40] Halicka, A.; Ogrodnik, P.; Zegardlo, B., 2013. Using ceramic sanitary ware waste as concrete aggregate. Construction and Building Materials, 48, 295–305.

[41] Saikia, N.; Brito, J., 2014. Mechanical properties and abrasion behaviour of concrete containing shredded PET bottle waste as a partial substitution of natural aggregate. Construction and Building Materials, 52, 236–244.
[42] Naik, T.R.; Singh, S.S.; Hossain, M.M., 1994. Abrasion resistance of concrete as influenced by inclusion of fly ash. Cement and Concrete Research, 24, Pages 303–312.
[43] Yen, T.; Hsu, T.H.; Liu, Y.W.; Chen S.H., 2007. Influence of class F fly ash on the abrasion–erosion resistance of high-strength concrete. Construction and Building Materials, 458–463.
[44] Siddique, R.; Kapoor, K.; Kadri, E.H.; Bennacer, R., 2012. Effect of polyester fibres on the compressive strength and abrasion resistance of HVFA concrete. Construction and Building Materials, 29, 270–278.
[45] Siddique, R., 2013. Compressive strength, water absorption, sorptivity, abrasion resistance and permeability of self-compacting concrete containing coal bottom ash. Construction and Building Materials, 47, 1444–1450.
[46] Martínez, I.; Etxeberria, M.; Pavón, E.; Díaz, N., 2013. A comparative analysis of the properties of recycled and natural aggregate in masonry mortars. Construction and Building Materials, 49, 384–392.
[47] Gameiro, F.; Brito, J.; Silva, D.C., 2014. Durability performance of structural concrete containing fine aggregates from waste generated by marble quarrying industry. Engineering Structures, 59, 654–662.
[48] Zelić, J., 2005. Properties of concrete pavements prepared with ferrochromium slag as concrete aggregate. Cement and Concrete Research, 35, 2340-2349.
[49] Swenson, E.G. A Canadian reactive aggregate undetected by ASTM tests. ASTM Bulletin 1957;226:48-51.
[50] Lee, S.Y.; Daugherty, A.M.; Broton, D. J., 2013. Assessing Aggregates for Radiation-Shielding Concrete. Concrete International, 35, 31-38.
[51] Hewlett, P.C. (ed.), 2003. Lea's Chemistry of Cement and Concrete, 4th ed. Butterworth Heinemann, Elsevier, England.
[52] Moukwa, M.; Lewis, B.G.; Shah, S.P.; Ouyang, C., 1993. Effects of clays on fracture properties of cement-based materials. Cement and Concrete Research, 23, 711-723.
[53] Changling, H.; Makovicky, E. and Osbæck, B., 1995. Pozzolanic reaction of six principal clay minerals: activation, reactivity assessments and technological effects. Cement and Concrete Research, 25, 1691-1702.
[54] Fam, M.A.; Santamarina, J. C., 1996. Study of clay-cement slurries with mechanical and electromagnetic waves. Journal of Geotechnical Engineering, 122, 365-373.
[55] Munoz, J. F.; Tejedor, M. I.; Anderson, M. A.; Cramer, S. M., 2010. Detection of aggregate clay coatings and impacts on concrete. ACI Materials Journal, 107, 387−395.
[56] Fernandes, V.A.; Purnell, P.; Still, G.T.; Thomas, T.H., 2007. The effect of clay content in sands used for cementitious materials in developing countries. Cement and Concrete Research, 37, 751−758.

Volume 8, Number 1 (February 2015) p. 25-49 • ISSN 1983-4195
REVISTA IBRACON DE ESTRUTURAS E MATERIAIS
IBRACON STRUCTURES AND MATERIALS JOURNAL

Thermal analysis of two-dimensional structures in fire

Análise térmica de estruturas bidimensionais em situação de incêndio



I. PIERIN [a]
igorpierin@usp.br

V. P. SILVA [a]
valpigss@usp.br

H. L. LA ROVERE [b]
henriettelarovere@gmail.com

Abstract

The structural materials, as reinforced concrete, steel, wood and aluminum, when heated have their mechanical proprieties degraded. In fire, the structures are subject to elevated temperatures and consequently the load capacity of the structural elements is reduced. The Brazilian and European standards show the minimal dimensions for the structural elements had an adequate bearing capacity in fire. However, several structural checks are not contemplated in methods provided by the standards. In these situations, the knowledge of the temperature distributions inside of structural elements as function of time of exposition is required. The aim of this paper is present software developed by the authors called ATERM. The software performs the thermal transient analysis of two-dimensional structures. The structure may be formed of any material and heating is provided by means of a curve of temperature versus time. The data input and the visualization of the results is performed thought the GiD software. Several examples are compared with software Super TempCalc and ANSYS. Some conclusions and recommendations about the thermal analysis are presented.

Keywords: fire, thermal analysis, finite element method, software.

Resumo

Os materiais utilizados na construção civil, tais como o concreto armado, aço, madeira e alumínio, sofrem degradação de suas propriedades mecânicas quando aquecidos. Em situação de incêndio, as estruturas são submetidas a elevadas temperaturas e, consequentemente, os elementos estruturais perdem sua capacidade portante. As normas brasileira e europeia apresentam algumas dimensões mínimas para os elementos estruturais apresentarem capacidade resistente adequada em situação de incêndio. Porém, diversas verificações estruturais não são contempladas nos métodos apresentados pelas normas. Nessas situações, é necessário o conhecimento da distribuição de temperaturas no interior do elemento estrutural em função do tempo de exposição ao incêndio. O objetivo deste artigo é apresentar um programa de computador desenvolvido pelos autores denominado de ATERM. O programa efetua a análise térmica de estruturas bidimensionais em regime transiente por meio do método dos elementos finitos. A estrutura pode ser constituída de qualquer material e o aquecimento é fornecido por meio de uma curva de temperaturas em função do tempo. A entrada de dados e visualização dos resultados é realizada por meio do programa GiD. Diversos resultados foram comparados ao programa Super Tempcalc e ao programa ANSYS. Ao final do artigo são extraídas algumas conclusões e recomendações sobre a análise térmica de estruturas em situação de incêndio.

Palavras-chave: incêndio, análise térmica, método dos elementos finitos, software.

[a] *Escola Politécnica da Universidade de São Paulo.*
[b] *Universidade Federal de Santa Catarina.*

Received: 12 Aug 2014 • Accepted: 17 Nov 2014 • Available Online: 03 Feb 2014

1. Introduction

In several engineering areas, it is very important to know the temperature distribution within a solid body. In civil engineering, especially in the structures fire design and in the design of roll compacted concrete dams, the interest in the study of temperature field evolution within structural elements have significantly grown in recent years.

Concrete structure fire design is ruled by ABNT NBR 15200:2012 [1]. This standard presents simplified methods and allows using advanced methods for checking structural elements in fire, besides the use of tests. The simplified methods are applicable in several situations. Nonetheless, there are design situations that cannot be represented by them, asking for a more refined analysis.

The use of advanced methods for verifying the fire safety of structures requires models for determining the development and distribution of temperatures in structural parts.

The thermal analysis may be based on the heat transfer principles and hypotheses. The model adopted may take into consideration the relevant thermal actions and the variation in thermal properties. When relevant, the effects of non-uniform thermal exposition and heat transfer through components of adjacent constructions should be included.

This paper presents a formulation for the thermal analysis of two-dimensional structures using finite elements. This formulation was implemented in a piece of software named ATERM [2], developed by the authors using FORTRAN 90 language. For data input and visualization of the field of temperatures, GiD [3] software is used. For the validation of results, comparisons were made using Super Tempcalc (STC) [4], developed in Lund, Sweden. STC began being developed in 1985 for the thermal analysis of two-dimensional structures. The software was checked against several experimental tests since its first version and was used for elaborating Eurocode 2 part 1.2 [5].

The results obtained by means of the ATERM [2] software will also be compared to that obtained by ANSYS [6]. SOLID70 elements will be used in the models for the thermal analysis. Convection and radiation effects will be simulated by means of the SURF152 element using one extra node. Models constructed in ANSYS software are tridimensional, but they can be compared to the two-dimensional models obtained by ATERM because there is no temperature variation along the longitudinal axis of the structural element.

ATERM was also used by SILVA [7] in the study of reinforced concrete columns in fire. In that study, a collection of isotherms for several cross sections was created.

2. Finite elements method

In its beginning, the Finite Elements Method was applied to mechanics problems in structural engineering. The thermal analysis was the first non-structural area to use it for modelling engineering problems. The determination of the field of temperatures within the structural element is the first step for structure fire analysis. Temperature distribution affects the stress distribution within the structural element.

Heat propagates within concrete by conduction. This phenomenon is governed by Poisson's equation, which, in its two-dimensional form, is given by equation (1).

$$\frac{\partial}{\partial x}\left(\lambda\frac{\partial\theta}{\partial x}\right)+\frac{\partial}{\partial y}\left(\lambda\frac{\partial\theta}{\partial y}\right)+\dot{Q}=\rho c\frac{\partial\theta}{\partial t} \quad (1)$$

In equation (1), λ is the material thermal conductivity, $\dot{Q}$ is the internally generated heat per volume unit per time, ρ is the density, c is the specific heat, θ is the temperature and t is the time.

To solve equation (1), it is necessary to impose the boundary and initial conditions of the mathematical model. The general boundary conditions of a structure subjected to Poisson's equation are the Dirichlet and Neumann's conditions. Dirichlet's condition, or prescribed temperature, supposes that, for any instant, the temperature in one part of the boundary is known. In fire analysis of structures, Dirichlet's condition is not important, for it does not take into consideration the heat transfer by convection and radiation.

Neumann's condition supposes that the heat flow in one part of the boundary, $\dot{q}$, is, for any instant, known. Mathematically, this condition can be written by equation (2), that is, the derivative of the temperature field in relation to the normal to the boundary surface, *n*.

$$-\lambda\frac{\partial\theta}{\partial n}=\dot{q} \quad (2)$$

One adiabatic, or thermally insulated, surface can be simulated by imposing zero heat flow ($\dot{q}=0$).

The convection and radiation phenomena are included into the numerical model by means of Neumann's boundary condition, which can be written by equation (3).

$$\dot{q}=\alpha_c\left(\theta-\theta_\infty\right)+\varepsilon\sigma\left(T^4-T_\infty^4\right) \quad (3)$$

In equation (3), α_c is the convection coefficient, θ and θ_∞ are, respectively, the temperatures in the structure and out of it, ε is the emissivity, σ is the Stefan-Boltzmann constant, T and T_∞ are, respectively, the absolute temperatures in the structure and out of it.

By making the part due to radiation linear, equation (3) can be rewritten by means of equation (4),

$$\dot{q}=\alpha_c\left(\theta-\theta_\infty\right)+\alpha_r\left(\theta-\theta_\infty\right)=\alpha\left(\theta-\theta_\infty\right) \quad (4)$$

In equation (4), α_r is the coefficient for heat transfer by radiation provided by equation (5).

$$\alpha_r=\varepsilon\sigma\left(T+T_\infty\right)\left(T^2+T_\infty^2\right) \quad (5)$$

As the coefficient for heat transfer by radiation depends on the structure temperature, the process becomes iterative.
The solution for the differential equation (1) can be numerically obtained by the finite elements method (FEM). For the use of FEM, it is necessary to write the weak problem formulation, which is obtained by equation (6).

$$\int_{\Omega} w\left[\frac{\partial}{\partial x}\left(\lambda\frac{\partial\theta}{\partial x}\right)+\frac{\partial}{\partial y}\left(\lambda\frac{\partial\theta}{\partial y}\right)+\dot{Q}-\rho c\frac{\partial\theta}{\partial t}\right]d\Omega=0 \quad (6)$$

In equation (6), *w* is an arbitrary function named weight function and Ω is the problem dominium.
Integrating the two first terms of equation (6) by parts and applying Gauss' Theorem, we obtain equation (7).

$$\int_{\Omega} w\left[\frac{\partial}{\partial x}\left(\lambda\frac{\partial\theta}{\partial x}\right)+\frac{\partial}{\partial y}\left(\lambda\frac{\partial\theta}{\partial y}\right)\right]d\Omega = \int_{S}\left(w\lambda\frac{\partial\theta}{\partial x}l+w\lambda\frac{\partial\theta}{\partial y}m\right)dS - \int_{\Omega}\left(\frac{\partial w}{\partial x}\lambda\frac{\partial\theta}{\partial x}+\frac{\partial w}{\partial y}\lambda\frac{\partial\theta}{\partial y}\right)d\Omega \quad (7)$$

In equation (7), *S* represents the problem boundary region and *l* and *m* are the director cosines.
Substituting equation (7) in (6), we have equation (8).

$$\int_{\Omega} w\dot{Q}d\Omega-\int_{\Omega} w\rho c\frac{\partial\theta}{\partial t}d\Omega+\int_{S}\left(w\lambda\frac{\partial\theta}{\partial x}l+w\lambda\frac{\partial\theta}{\partial y}m\right)dS-\int_{\Omega}\left(\frac{\partial w}{\partial x}\lambda\frac{\partial\theta}{\partial x}+\frac{\partial w}{\partial y}\lambda\frac{\partial\theta}{\partial y}\right)d\Omega=0 \quad (8)$$

Discretizing the problem dominium in a finite number of elements and using Galerkin Method, the set of interpolation functions *N,* as weight functions, the temperature in any point of the finite element can be approximated by equation (9).

$$\theta(x,y,t)=\sum_{i}^{n}N_i\theta \quad (9)$$

In equation (9), *n* is the number of nodes of the element, $N_i=N_i(x,y)$ are the interpolation functions and θ_i are the nodal temperatures of the element.
Substituting equation (9) in (8), we get to the equations system (10), which represents the thermal balance in each finite element.

$$-\int_{A_e}\left[\lambda\frac{\partial N_i}{\partial x}\frac{\partial\theta}{\partial x}+\lambda\frac{\partial N_i}{\partial y}\frac{\partial\theta}{\partial y}-N_i\dot{Q}+N_i\rho c\frac{\partial\theta}{\partial t}\right]dA_e+\int_{S_e}N_i\lambda\frac{\partial\theta}{\partial x}ldS_e+\int_{S_e}N_i\lambda\frac{\partial\theta}{\partial y}mdS_e=0 \quad \text{for i= 1 to n,} \quad (10)$$

In equations (10), *A* and *S* represent the area and the surface of the element dominium.
The derivative of the temperature field in relation to the normal to the boundary surface, *n,* can be written in function of the director cosines, *l* and *m,* by means of equation (11).

$$\frac{\partial\theta}{\partial n}=\frac{\partial\theta}{\partial x}l+\frac{\partial\theta}{\partial y}m \quad (11)$$

Substituting equations (2), (4) and (11) in equation (10), we obtain expression (12),

$$\int_{A_e}N_i\dot{Q}dA_e-\int_{A_e}N_i\rho c\frac{\partial\theta}{\partial t}dA_e-\int_{A_e}\left[\lambda\frac{\partial N_i}{\partial x}\frac{\partial\theta}{\partial x}+\lambda\frac{\partial N_i}{\partial y}\frac{\partial\theta}{\partial y}\right]dA_e-\int_{S_e}N_i\alpha\left(\theta-\theta_{\infty}\right)dS_e=0 \quad (12)$$

Defining the interpolation function vector $\boldsymbol{N}$ and the nodal temperatures vector $\boldsymbol{\theta}$ by means of expressions (13).

$$\boldsymbol{N}=\begin{bmatrix}N_1 & N_2 & \dots & N_{n-1} & N_n\end{bmatrix}$$
$$\theta=\begin{bmatrix}\theta_1 & \theta_2 & \dots & \theta_{n-1} & \theta_n\end{bmatrix}^T \quad (13)$$

Where *n* is the number of nodes of the element and N_i are the interpolation functions of the finite element.
Thus, we can rewrite equation (9) in the matrix form by means of equation (14).

$$\theta(x,y,t)=\sum_{i=1}^{n}N_i\theta=\boldsymbol{N}\theta \quad (14)$$

We also define the conductivity matrix of the material, for the case of isotropic material, by means of equation (15) and the gradient vector by equation (16).

$$\lambda = \begin{bmatrix} \lambda & 0 \\ 0 & \lambda \end{bmatrix} \quad (15)$$

$$\nabla = \begin{Bmatrix} \dfrac{\partial}{\partial x} \\ \dfrac{\partial}{\partial y} \end{Bmatrix} \quad (16)$$

Inserting equations (13) and (16) in equation (12) and rearranging the terms, we obtain the following set of equations (17).

$$\int_{A_e} \boldsymbol{N}^T \rho c \boldsymbol{N} \frac{\partial \theta}{\partial t}\, dA_e + \int_{A_e} (\nabla \boldsymbol{N})^T \lambda \nabla \boldsymbol{N} \theta \, dA_e + \int_{S_e} \boldsymbol{N}^T \alpha \boldsymbol{N} \theta \, dS_e = \int_{A_e} \boldsymbol{N}^T \dot{Q} \, dA_e + \int_{S_e} \boldsymbol{N}^T \alpha \theta_\infty dS_e \quad (17)$$

The set of equations (17) can be rewritten in the matrix form by means of equation (18).

$$\boldsymbol{C}\dot{\theta} + \boldsymbol{K}\theta = \boldsymbol{F} \quad (18)$$

In equation (18), $\dot{\boldsymbol{\theta}}$ is the first derivative of the temperatures field in relation to time.
The total capacitance matrix ($\boldsymbol{K}$) of the element is given by equation (19).

$$\boldsymbol{K} = \boldsymbol{K}_{cond} + \boldsymbol{K}_{conv\_rad} \quad (19)$$

The element conductivity matrix is given by equation (20).

$$\boldsymbol{K}_{cond} = \int_{A_e} \boldsymbol{B}^T \lambda \boldsymbol{B} dA_e \quad (20)$$

where

$$\boldsymbol{B} = \nabla \boldsymbol{N} \quad (21)$$

And the matrix due to the combined effects of convection and radiation of the element is given by equation (22).

$$\boldsymbol{K}_{conv\_rad} = \int_{S_e} (\alpha_c + \alpha_r) \boldsymbol{N}^T \boldsymbol{N} \theta \, dS_e \quad (22)$$

We define the thermal capacity of the material as the product density (ρ) x specific heat (c). Thus, the thermal capacity matrix ($\boldsymbol{C}$) of the element is given by equation (23).

$$\boldsymbol{C} = \int_{A_e} \boldsymbol{N}^T \rho c \boldsymbol{N} dA_e \quad (23)$$

The vector of the consistent thermal actions ($\boldsymbol{F}$) is given by expression (24).

$$\boldsymbol{F} = \int_{A_e} \boldsymbol{N}^T \dot{Q} \, dA_e + \int_{S_e} \boldsymbol{N}^T (\alpha_c + \alpha_r) \theta_\infty dS_e \quad (24)$$

In equation (24), θ_∞ is the temperature outside the structure.
Matrixes $\boldsymbol{N}$ and $\boldsymbol{B}$ depend on the type of element used in structure discretizing.
In ATERM, we employ rectangular and triangular planes of four and three nodes, respectively, and two nodes special bar elements for considering convection and radiation heat transfer effects, which can be superimposed in any face of the plane elements. These elements are briefly described in the following items. Further details on the used finite elements and the computational implementation can be found in Pierin [2].

2.1 Four nodes rectangular element

The four-node plane rectangular finite element with sides 2a by 2b used herein is represented in Figure 1.
The interpolation functions N_i are defined by means of equation (25).

$$N_i = \frac{1}{4}\left(1 + \frac{x}{x_i}\right)\left(1 + \frac{y}{y_i}\right) \text{ to } i = 1,2,3,4 \quad (25)$$

By substituting equations (15), (21) and (25) in equation (20), we obtain equation (26), which represents the matrix of conductivity of the four-node plane rectangular element.

$$\boldsymbol{K}_{cond} = \frac{\lambda a}{6b}\begin{bmatrix} 2 & -2 & -1 & 1 \\ -2 & 2 & 1 & -1 \\ -1 & 1 & 2 & -2 \\ 1 & -1 & -2 & 2 \end{bmatrix} + \frac{\lambda b}{6a}\begin{bmatrix} 2 & 1 & -1 & -2 \\ 1 & 2 & -2 & -1 \\ -1 & -2 & 2 & 1 \\ -2 & -1 & 1 & 2 \end{bmatrix} \quad (26)$$

Figure 1 – Four nodes rectangular element

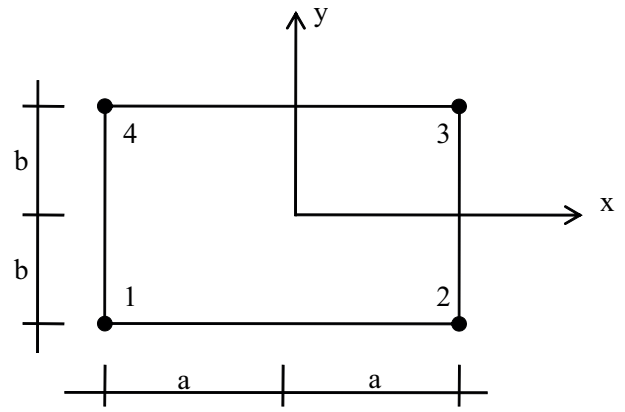

Substituting equation (25) in equation (23), we obtain the matrix of the thermal capacity of this element, which is expressed by equation (27),

$$\boldsymbol{C} = \frac{\rho c a b}{36}\begin{bmatrix} 4 & 2 & 1 & 2 \\ 2 & 4 & 2 & 1 \\ 1 & 2 & 4 & 2 \\ 2 & 1 & 2 & 4 \end{bmatrix} \quad (27)$$

2.2 Triangular element

The triangular finite element used in ATERM software has three nodes identified by 1, 2 and 3 and is represented in Figure 2.

Figure 2 – Triangular element

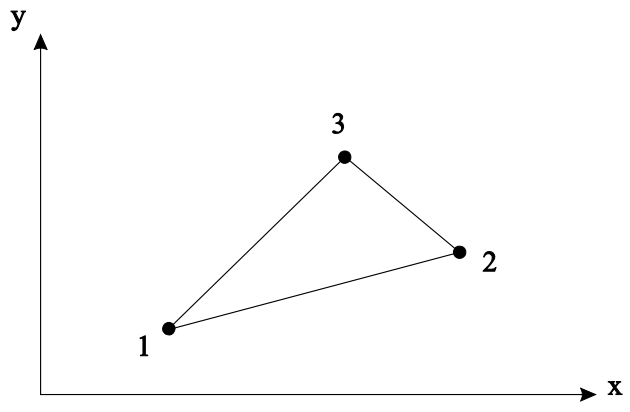

Functions N_i used for interpolation of the nodal temperatures within the triangular finite element are defined by equation (28).

$$N_i = \frac{1}{2A}\left(a_i + b_i x + c_i y\right) \text{ to } i = 1,2,3 \quad (28)$$

In equation (28), *A* represents the area of the finite element and the coefficients a_i, b_i and c_i are provided by expressions (29).

$$\begin{aligned} a_1 &= X_2Y_3 - X_3Y_2; \quad b_1 = Y_2 - Y_3; \quad b_1 = X_3 - X_2 \\ a_2 &= X_3Y_1 - X_1Y_3; \quad b_2 = Y_3 - Y_1; \quad b_2 = X_1 - X_3 \\ a_3 &= X_1Y_2 - X_2Y_1; \quad b_3 = Y_1 - Y_2; \quad b_3 = X_2 - X_1 \end{aligned} \quad (29)$$

In expressions (29), X_i and Y_i represent the coordinates of node *i*. Substituting equations (15), (21) and (28) in equation (20), we obtain equation (30), which represents the matrix of conductivity of the plane triangular element.

$$\boldsymbol{K}_{cond} = \frac{\lambda}{4A}\begin{bmatrix} b_1^2 + c_1^2 & b_1b_2 + c_1c_2 & b_1b_3 + c_1c_3 \\ b_1b_2 + c_1c_2 & b_2^2 + c_2^2 & b_2b_3 + c_2c_3 \\ b_1b_3 + c_1c_3 & b_2b_3 + c_2c_3 & b_3^2 + c_3^2 \end{bmatrix} \quad (30)$$

Substituting equation (28) in equation (23), we obtain the matrix of thermal capacity of this element, expressed by equation (31).

$$\boldsymbol{C} = \frac{\rho c A}{12}\begin{bmatrix} 2 & 1 & 1 \\ 1 & 2 & 1 \\ 1 & 1 & 2 \end{bmatrix} \quad (31)$$

2.3 Two nodes bar special element

The Neumann's boundary conditions can be imposed to the finite elements model by means of a two-node linear element with

Figure 3 – Convection and radiation finite element

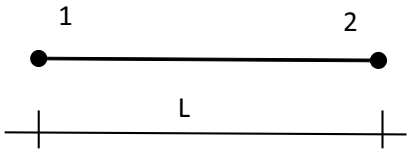

length L, as shown in Figure 3. It is emphasized that, for model coherence, the two-node linear element has to be coincident with the faces of the finite element used for structure discretization.
The matrix of interpolation functions for the finite element of convection and radiation is defined by equation (32).

$$\boldsymbol{N} = \left[1 - \frac{x}{L} \quad \frac{x}{L}\right] \tag{32}$$

Note that the convection linear element is fully compatible with the previously formulated four-node rectangular element because it uses linear functions for temperatures interpolation along the element side.
Substituting equation (32) in expression (22), the convection matrix and the vector of consistent thermal actions due to the convective heat flow are provided by equations (33) and (34), respectively,

$$\boldsymbol{K}_{conv\_rad} = \frac{(\alpha_c + \alpha_r)L}{6}\begin{bmatrix} 2 & 1 \\ 1 & 2 \end{bmatrix} \tag{33}$$

$$\boldsymbol{F}_{conv\_rad} = (\alpha_c + \alpha_r)\theta_\infty \begin{bmatrix} L/2 \\ L/2 \end{bmatrix} \tag{34}$$

3. Cavities

In some structural elements, such as alveolar, ceramic blocks and ribbed slabs filled with EPS blocks, there is the presence of enclosed air inside cavities. The existence of cavities within the structure generates heat transfer by convection and radiation, due to the heating of the enclosed air.
Discretizing the analyzed structure boundary in plane finite elements and the cavity contour in special two-node finite elements, as per Figure 4, we can obtain the temperature of the air inside the cavity from the nodal temperatures by means of equation (35).

$$\sum_{i=1}^{N}\left(\alpha_i(\theta_{cav} - \theta_i) + \varepsilon_i\sigma\left(T_{cav}^4 - T_i^4\right)\right)L_i + \rho_{ar}c_{ar}A_{cav}\left(\theta_{cav} - \theta_{cav}^{t-1}\right) = 0 \tag{35}$$

In equation (35), α_i is the convection coefficient of element *i*, θ_i and θ_{cav} are the temperatures in the element and in the air, respectively, ε_i is the emissivity, σ is the Stefan-Boltzmann Constant, T_i and T_{cav} are the absolute temperatures in and outside the structure, respectively, θ_{cav}^{t-1} is the temperature of air inside the cavity at the previous instant, A_{cav} is the cavity area, c_{ar} and ρ_{ar} are the specific heat and density of air, respectively. L_i is the length of the special finite element.
Equation (35) can be rewritten by means of equation (36).

$$A\theta_{cav}^4 + B\theta_{cav} - C = 0 \tag{36}$$

$$A = \sum_{i-1}^{N}\sigma\varepsilon_i L_i$$

$$B = \sum_{i=1}^{N}\alpha_i L_i + \rho_{ar}c_{ar}A_{cav} \tag{37}$$

$$C = \sum_{i=1}^{N}\alpha_i L_i\theta_i + \sum_{i=1}^{N}\sigma\varepsilon_i L_i T_i^4 + \rho_{ar}c_{ar}A_{cav}\theta_{cav}^{t-1}$$

Figure 4 – Mesh of finite elements

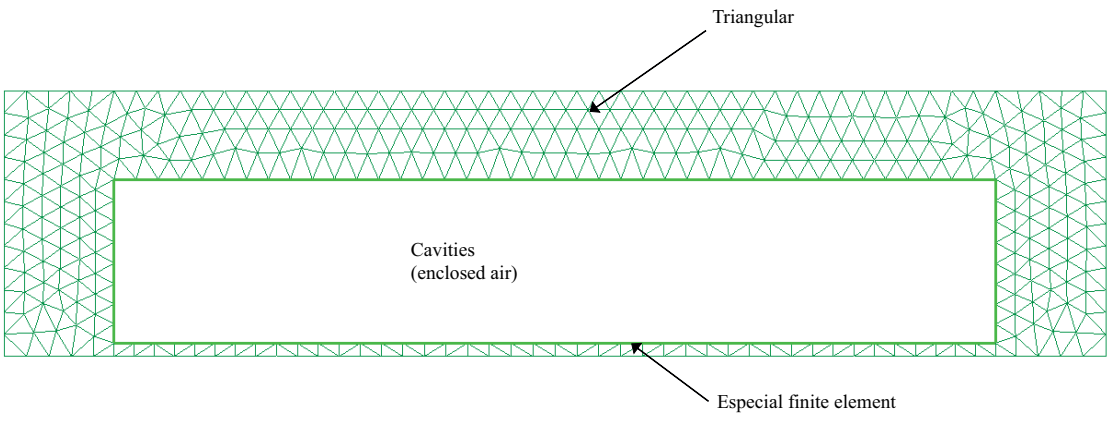

4. Pre-processing

The data input to ATERM software is accomplished by text files that contain information on the two-dimensional structure to be thermally analyzed. This information comprehends the nodes coordinates, the elements connectivity and thermal properties of the materials.

In order to ease the creation of the input data file, some geometry models, such as rectangular and T sections, were created based on GiD software [3], as shown in Figure 5. In these models, it is only necessary to inform the dimensions of the sections, of the finite elements and the type of material.

The exposition to fire can be configured directly in the model, by the indication of the surfaces exposed to standard fire and the surfaces exposed to a constant temperature, as shown in Figure 6. In addition, emissivity and convection coefficients for the consideration of heat transfer by convection and radiation should be informed.

The thermal properties of the materials, such as conductivity, density and coefficient of strength reduction, are informed by means of tables in function of the temperature as shown in Figure 7. We can also define materials the thermal properties of which are independent of temperature.

Other data also necessary to the thermal analysis, such as total time of fire exposition, time increment, initial temperature of the structure, α coefficient for the choice of the time integration method, tolerance for temperatures convergence, time increase for printing results, should be informed as shown in Figure 8. Coefficient α varies from 0 (Euler Implicit Method) to 1 (Euler Explicit Method) and defines the numerical stability for the integration along time.

STC software uses α=2/3, known as Galerkin Method.

5. Numerical simulation

In order to validate the software developed in this work, three simulations were performed, the results of which were compared to those obtained by means of STC [4] and ANSYS [6] software. The thermal properties adopted for concrete were based on ABNT NBR 15200.2012 [1]. In the examples herein, we used siliceous concrete humidity content equal to 1.5% in weight.

In all of the examples, the thermal action is determined according to ISO 834 [8] standard fire curve.

5.1 Concrete beam

As example # 1, the heating of a 20 x 50 cm rectangular

Figure 5 – Models for geometry creation

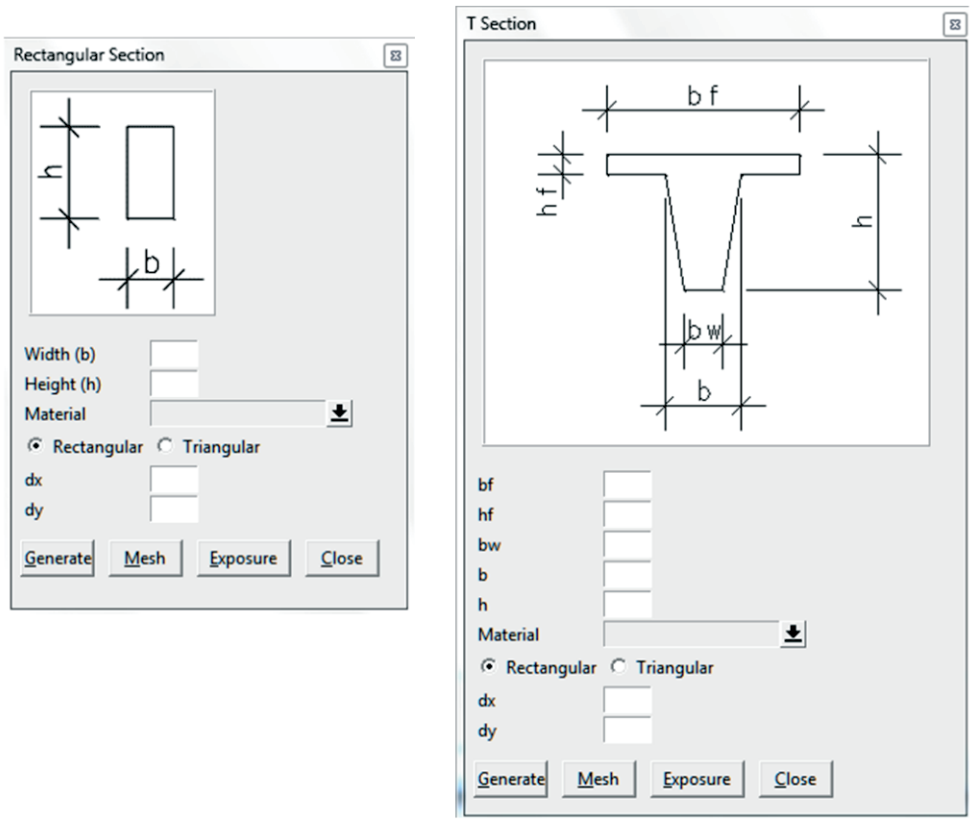

Figure 6 – Exposition to fire

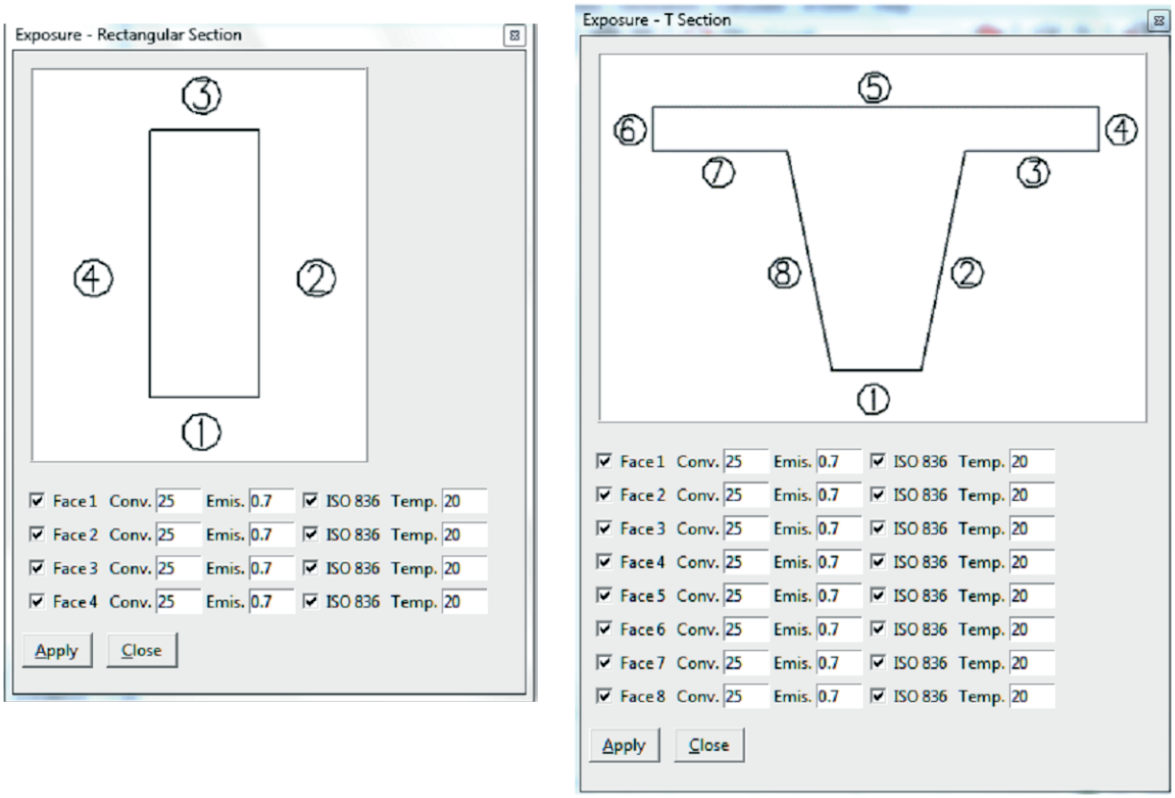

Figure 7 – Thermal properties of materials

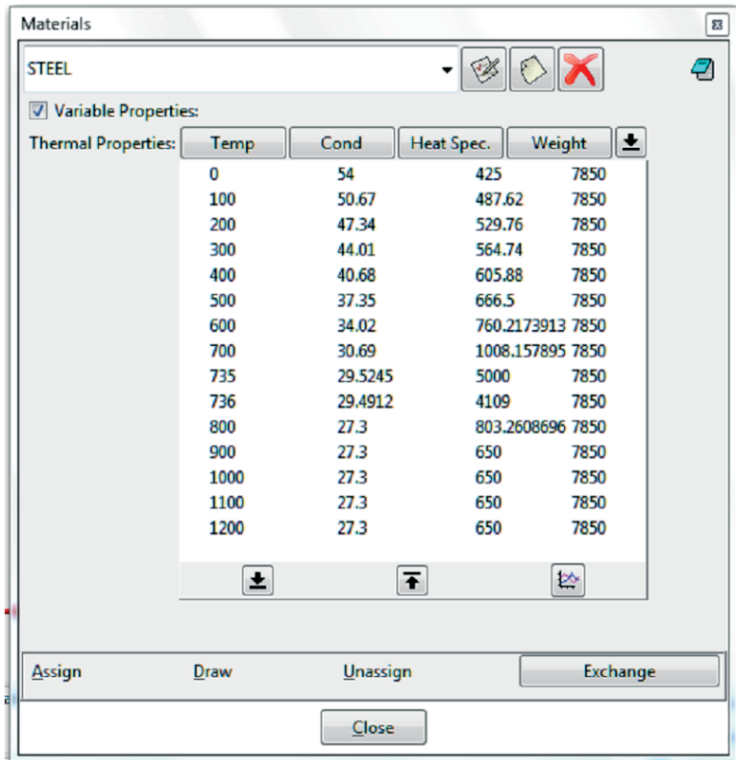

Figure 8 – Other data

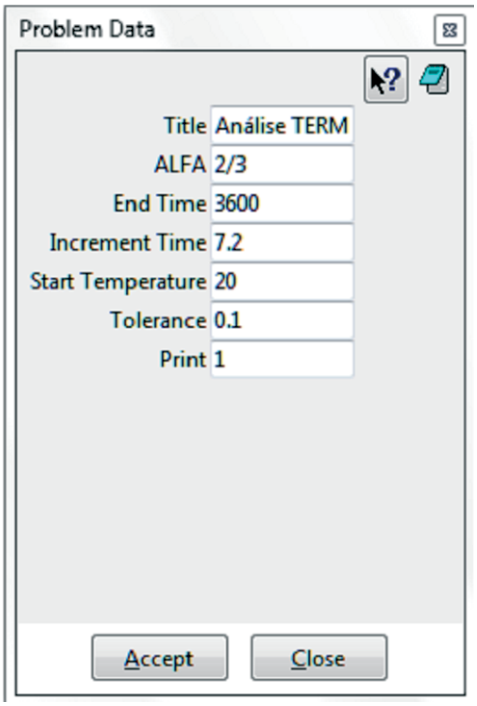

section concrete beam is analyzed, as shown in Figure 9. The fire is admitted to act on three surfaces of the beam. The density of the concrete is considered variable with temperature [1] and that for 20 ºC the density is equal to 2400 kg/m³, according to ABNT NBR 6118:2014 [9] recommendations. The emissivity factor and convection coefficient

Figure 9 – Geometry of beam

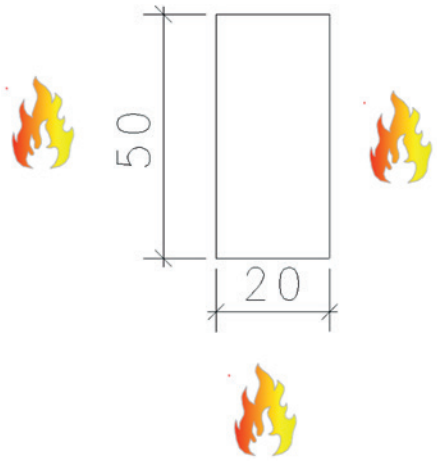

Figure 10 – Influence of the mesh on the nodal temperature

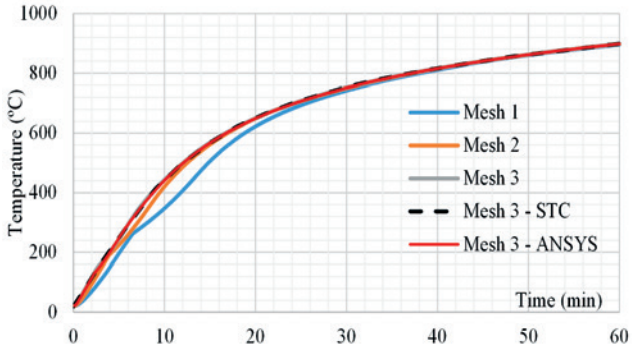

were adopted equal to 0.7 and 25 W/m².ºC, respectively. For the initial temperature of the structure, the value 20ºC is adopted.

The structure was discretized in square elements. For ATERM software, 3 meshes were used: in Mesh 1, we used elements with 5 cm sides, in Mesh 2, with 2.5 cm sides and, in Mesh 3, with 1 cm sides. For modeling in ANSYS and STC, we only used Mesh 3. Figure 10 shows the influence of the mesh refinement on the evolution of temperature in function of time in the node in the middle of the smaller heated side. With mesh refinement, the temperatures is observed to rise a little up to instant t = 28 minutes and after this instant, the temperatures obtained for the different meshes are virtually equal. The solution is verified to tend to converge with mesh refinement and that, for Mesh 3, the results from ATERM, ANSYS and STC are virtually equal.

5.2 *Ribbed slab*

Figure 11 shows the geometry of the thermally analyzed ribbed slab (dimensions in cm). The slab underside is exposed to fire. The adopted values for emissivity factor and convection coefficient were 0.7 and 25 W/m².ºC, respectively, as per Eurocode 2 part 1.2 [5] recommendations. In the upside of the slab, not exposed to fire, the combined phenomena of convection and ra-

Figure 11 – Geometry of ribbed slab

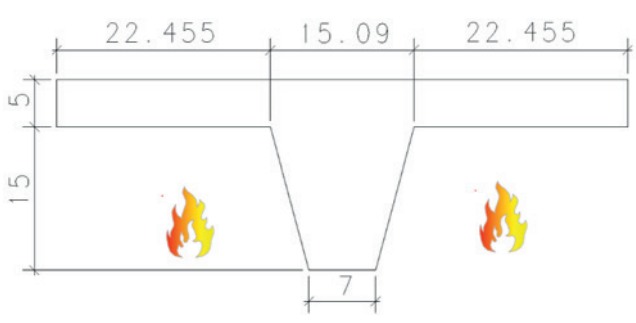

Figure 12 – Analyzed model

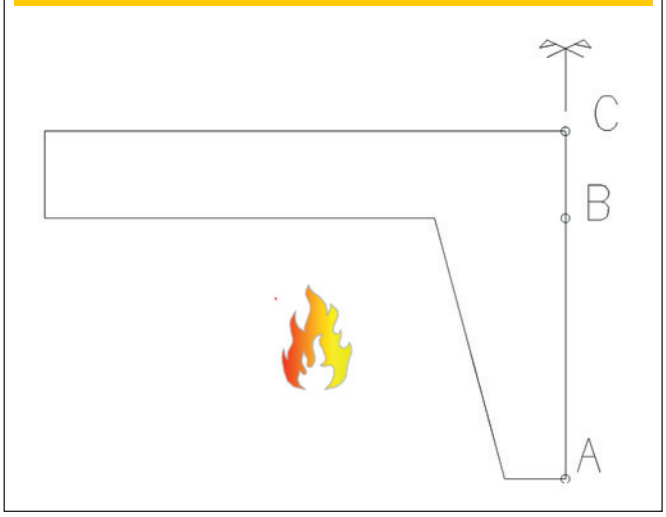

diation were simulated by α_c = 9 W/m² °C [10]. The adopted initial structure temperature was 20 °C. Due to symmetry, only half of the slab was modeled and the symmetry axis was considered to be adiabatic.

Figure 13 shows the variation in the nodal temperature in function of time obtained by ATERM and STC for three distinct points located in the slab symmetry axis (as shown in Figure 12): point A – in the base of the rib. Point B – at the level of the junction between the rib and the flange. Point C – in the upside of the slab. The slab was discretized by triangular elements with 0.5 cm sides, 1653 elements being generated in STC and 1809 elements in ATERM. The difference between the numbers of elements generated by the two pieces of software is due to the distinct mesh generators used by them. The results obtained from the two pieces of software are virtually equal. It is also noted that there is good correlation between the results from ATERM and ANSYS.

Figure 14 shows the field of temperatures after 60 minutes of fire, obtained by ATERM and STC.

Figure 13 – Temperature evolution in function of time

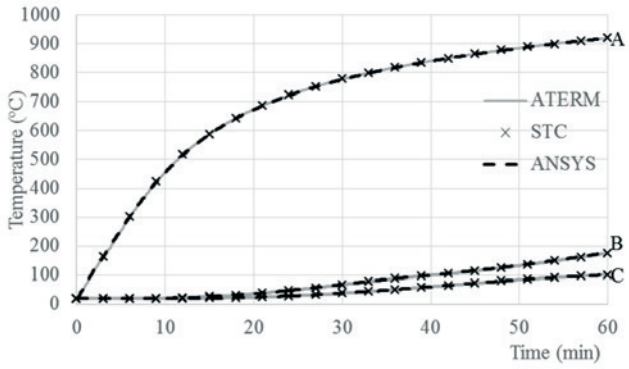

5.3 Design of padded ribbed slabs

In Brazil, ribbed slabs filled with EPS on cement plates, as shown in Figure 15, are also used. When heated, EPS decomposes quickly, resulting in a large space filled with trapped air. This trapped air contributes to the heat transfer between the cement plate, which is at higher temperatures, and the flange. This heat transfer can be taken into account in the numerical model by means of the procedure indicated in item 3 herein.

In the face directly heated by the fire, we applied the ISO 834 [7] standard curve and, in the face not directly exposed to the heat, a combination of convection and radiation, simulated by a_c = 9 W/m² °C, was used.

The thermal properties of the cement plates used in the analyses were: thermal conductivity equal to 2.22 W/m°C, specific heat equal to 840 J/kg K and density equal to 1200 kg/m³ [11].

The variation in temperature was analyzed in two points, as shown in Figure 16: point A – middle point of the upper face of the flange and point B – located in the steel plate. EPS was admitted totally consumed by the fire and disregarded in the analysis.

The variation in temperature of points A and B, in function of the

Figure 14 – Field of temperatures for 60 minutes: (a) ATERM e (b) STC

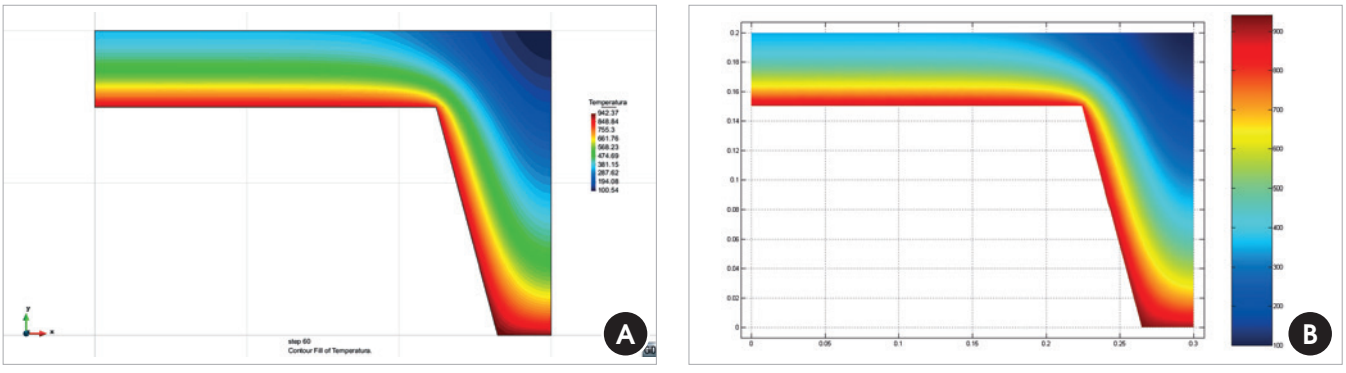

Figure 15 – Model with EPS/cement plate (dimensions in mm)

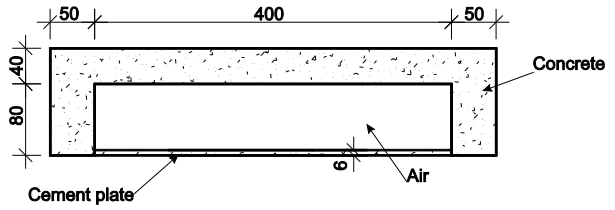

time of fire exposition is represented in Figure 17. Once more, a good correlation between the results obtained by ATERM and STC is verified.

The consideration of the trapped air in the model is observed to cause heating in the upside of the slab in the region between ribs. The fields of temperature at 60 minutes of standard fire on the downside of the slab, with and without the trapped air consideration, are represented in Figures 18 and 19, respectively.

Disregarding the air trapped inside the cavity does not generate the heating of the upside of the slab in the region between ribs, i.e., after 60 minutes of fire, the upside of the slab is at room temperature. There is only a slight rise of the upside temperature in the region of the ribs.

In reality, the trapped air generates heat transfer by convection and radiation between the heated surface (the cement plate) and the face not exposed to fire (flange). This example shows that this heat transfer can be modeled by means of cavities.

6. Conclusion

Within this work, we presented the formulation of the Finite Element Method applied to non-linear thermal analysis of two-dimensional structures, employed in the elaboration of the ATERM software. This kind of analysis is critical to the study of structures in fire.

The results were validated with STC [4] and by means of ANSYS [6] software. It was observed that the results obtained by both types of software present an excellent correlation in all the examples performed.

However, depending on the mesh used, the results were observed not to correspond to the physical behavior. Thus, a study of geometrical and time meshes is recommended before undertaking a thermal analysis.

In some situations, such as in ribbed slabs and ribbed slabs filled with inert material, cavities do exist within the structural element. Such cavities are filled with trapped air that, when heated, transfer heat by convection and radiation to the neighboring regions. In the finite element analysis, the heat transfer by means of the trapped air can be considered, both by ATERM and STC softwares.

The performance of ATERM showed that the software is very effective in relation to STC, having a much shorter processing time. By means of the GiD software, several sections were created for data input, such as rectangular and T sections, which facilitate the creation of the geometry and the mesh of finite elements.

Figure 16 – Control points for the analysis

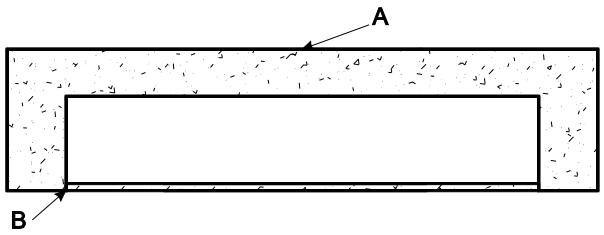

These basic models can be used to define other more complex geometries.

7. Acknowledgments

We thank FAPESP – the State of São Paulo Research Foundation the Brazilian National Council of Scientific and Technological Development, CNPq –and Tuper for their support.

8. Bibliography

[01] ASSOCIAÇÃO BRASILEIRA DE NORMAS TÉCNICAS. NBR 15200: Projeto de estruturas de concreto em situação de incêndio. Rio de Janeiro, 2012.

[02] PIERIN; I. A instabilidade de perfis formados a frio em situação de incêndio. Tese de Doutorado. Escola Politécnica. Universidade de São Paulo. 2011.

[03] International Center for Numerical Methods in Engineering (CIMNE). GiD 10.0 Users Manual. http://gid.cimne.upc.es/., 2011.

[04] FIRE SAFETY DESIGN (FSD). TCD 5.0 User's manual. Lund: Fire Safety Design AB, 2007.

[05] EUROPEAN COMMITTEE FOR STANDARDIZATION. EN 1992-1-2: Eurocode 2: Design of concrete structures - part 1.2: general actions - actions on structures exposed to fire. Brussels: CEN, 2004.

Figure 17 – Evolution of temperature in function of time for points A and B

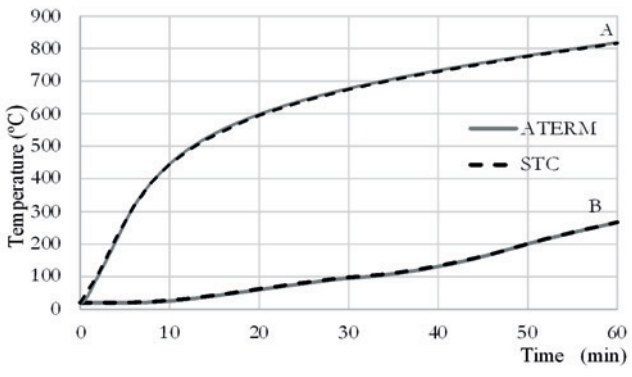

Figure 18 – Field of temperatures for 60 minutes (with presence of cavities)

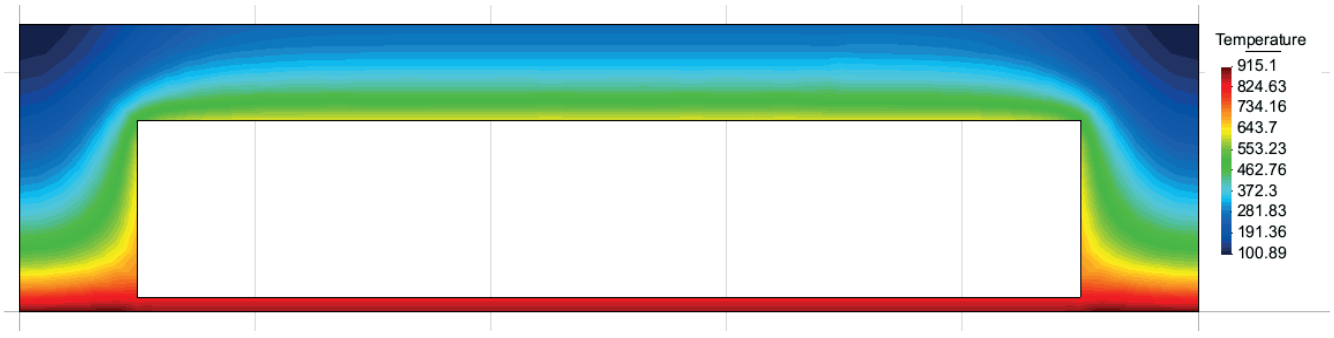

Figure 19 – Field of temperatures for 60 minutes (no cavities)

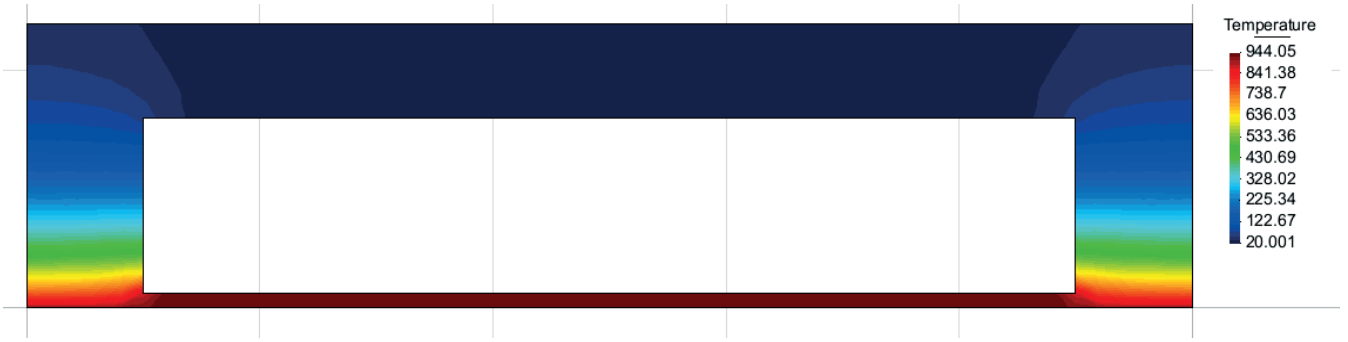

[06] Ansys INC, (2004). Ansys Realese 9.0 – Documentation,

[07] SILVA; V. P. Projeto de estruturas de concreto em situação de incêndio. Editora Blucher, 2012.

[08] INTERNATIONAL ORGANIZATION FOR STANDARDIZATION. ISO 834: Fire-resistance tests: elements of building construction - part 1.1: general requirements for fire resistance testing. Geneva, 1999. 25 p. (Revision of first edition ISO 834:1975).

[09] ASSOCIAÇÃO BRASILEIRA DE NORMAS TÉCNICAS. NBR 6118: Projeto de estruturas de concreto. Rio de Janeiro, 2014.

[10] EUROPEAN COMMITTEE FOR STANDARDIZATION. EN 1991-1-2: Eurocode 1: Actions on structures - part 1.2: general actions - actions on structures exposed to fire. Brussels: CEN, 2002.

[11] PIERIN; I., SILVA; V. P. Fire design of composite ribbed slabs. Revista IBRACON de Estruturas e Materiais. v. 7, p. 178-192, 2014.

Volume 8, Number 1 (February 2015) p. 25-48 • ISSN 1983-4195

REVISTA IBRACON DE ESTRUTURAS E MATERIAIS

IBRACON STRUCTURES AND MATERIALS JOURNAL

Thermal analysis of two-dimensional structures in fire

Análise térmica de estruturas bidimensionais em situação de incêndio



I. PIERIN [a]
igorpierin@usp.br

V. P. SILVA [a]
valpigss@usp.br

H. L. LA ROVERE [b]
henriettelarovere@gmail.com

Abstract

The structural materials, as reinforced concrete, steel, wood and aluminum, when heated have their mechanical proprieties degraded. In fire, the structures are subject to elevated temperatures and consequently the load capacity of the structural elements is reduced. The Brazilian and European standards show the minimal dimensions for the structural elements had an adequate bearing capacity in fire. However, several structural checks are not contemplated in methods provided by the standards. In these situations, the knowledge of the temperature distributions inside of structural elements as function of time of exposition is required. The aim of this paper is present software developed by the authors called ATERM. The software performs the thermal transient analysis of two-dimensional structures. The structure may be formed of any material and heating is provided by means of a curve of temperature versus time. The data input and the visualization of the results is performed thought the GiD software. Several examples are compared with software Super TempCalc and ANSYS. Some conclusions and recommendations about the thermal analysis are presented.

Keywords: fire, thermal analysis, finite element method, software.

Resumo

Os materiais utilizados na construção civil, tais como o concreto armado, aço, madeira e alumínio, sofrem degradação de suas propriedades mecânicas quando aquecidos. Em situação de incêndio, as estruturas são submetidas a elevadas temperaturas e, consequentemente, os elementos estruturais perdem sua capacidade portante. As normas brasileira e europeia apresentam algumas dimensões mínimas para os elementos estruturais apresentarem capacidade resistente adequada em situação de incêndio. Porém, diversas verificações estruturais não são contempladas nos métodos apresentados pelas normas. Nessas situações, é necessário o conhecimento da distribuição de temperaturas no interior do elemento estrutural em função do tempo de exposição ao incêndio. O objetivo deste artigo é apresentar um programa de computador desenvolvido pelos autores denominado de ATERM. O programa efetua a análise térmica de estruturas bidimensionais em regime transiente por meio do método dos elementos finitos. A estrutura pode ser constituída de qualquer material e o aquecimento é fornecido por meio de uma curva de temperaturas em função do tempo. A entrada de dados e visualização dos resultados é realizada por meio do programa GiD. Diversos resultados foram comparados ao programa Super Tempcalc e ao programa ANSYS. Ao final do artigo são extraídas algumas conclusões e recomendações sobre a análise térmica de estruturas em situação de incêndio.

Palavras-chave: incêndio, análise térmica, método dos elementos finitos, software.

[a] *Escola Politécnica da Universidade de São Paulo.*
[b] *Universidade Federal de Santa Catarina.*

Received: 12 Aug 2014 • Accepted: 17 Nov 2014 • Available Online: 03 Feb 2014

1. Introdução

O conhecimento da distribuição de temperaturas no interior de um sólido é de grande importância em várias áreas da engenharia. Na Engenharia Civil, em particular nos projetos de estruturas em situação de incêndio e nos projetos de barragens de concreto compactado a rolo, o interesse pelo estudo da evolução do campo de temperaturas nos elementos estruturais tem crescido consideravelmente nos últimos anos.

O projeto de estruturas de concreto em situação de incêndio é regido pela norma ABNT NBR 15200:2012 [1]. Essa norma apresenta métodos simplificados e permitem métodos avançados para a verificação dos elementos estruturais em situação de incêndio, além do uso de ensaios. Em diversas situações, os métodos simplificados são aplicáveis. No entanto, há situações de projeto que não podem ser representadas pelas formulações simplificadas presentes na norma, sendo necessária uma análise mais refinada.

O uso dos métodos avançados de verificação da segurança das estruturas em situação de incêndio requer modelos para a determinação do desenvolvimento e da distribuição de temperatura nas peças estruturais.

A análise térmica deve ser baseada em princípios reconhecidos e hipóteses da transferência de calor. O modelo adotado deve considerar as ações térmicas relevantes e a variação das propriedades térmicas do material com a temperatura. Os efeitos da exposição térmica não uniforme e da transferência de calor em componentes de edifícios adjacentes devem ser incluídos quando forem relevantes.

Apresenta-se neste artigo uma formulação para a análise térmica de estruturas bidimensionais utilizando o método dos elementos finitos. Esta formulação foi implementada em um programa computacional denominado ATERM [2], desenvolvido pelos autores na linguagem FORTRAN 90. Para a entrada de dados e a visualização do campo de temperaturas, utiliza-se o programa GiD [3]. Para validar os resultados obtidos pelo programa ATERM, foram feitas comparações ao programa Super Tempcalc (STC) [4], desenvolvido em Lund, Suécia. O programa STC começou a ser desenvolvido em 1985 para a análise térmica de estruturas bidimensionais. O programa foi verificado em comparação a inúmeros ensaios experimentais, desde a sua primeira versão e foi utilizado na elaboração do Eurocode 2 parte 1.2 [5].

Os resultados obtidos por meio do programa ATERM [2] também serão comparados aos obtidos pelo programa ANSYS [6]. Nos modelos serão utilizados os elementos SOLID70 para a análise térmica. Os efeitos de convecção e radiação serão simulados por meio do elemento SURF152 com a utilização do nó extra. Os modelos construídos no programa ANSYS são tridimensionais, porém podem ser comparados aos modelos bidimensionais obtidos no ATERM, pois não há variação de temperatura ao longo do eixo longitudinal do elemento estrutural.

O programa ATERM já foi utilizado por SILVA [7] para o estudo de pilares de concreto armado em situação de incêndio. Neste estudo foi elaborada uma biblioteca de isotermas para várias seções transversais.

2. Método dos elementos finitos

Inicialmente, o método dos elementos finitos foi aplicado a problemas mecânicos da engenharia estrutural. A análise térmica foi a primeira área não estrutural a utilizar o método dos elementos finitos para a modelagem de problemas de engenharia.

A determinação do campo de temperaturas no elemento estrutural é o primeiro passo para a análise de estruturas em situação de incêndio. A distribuição de temperaturas influencia a distribuição de tensões no elemento estrutural.

O calor propaga-se no concreto por condução, cujo fenômeno é regido pela equação de Poisson que, para domínios bidimensionais, é dada pela equação (1).

$$\frac{\partial}{\partial x}\left(\lambda\frac{\partial\theta}{\partial x}\right)+\frac{\partial}{\partial y}\left(\lambda\frac{\partial\theta}{\partial y}\right)+\dot{Q}=\rho c\frac{\partial\theta}{\partial t} \quad (1)$$

Na equação (1), λ é a condutividade térmica do material, $\dot{Q}$ é o calor gerado internamente por unidade de volume e de tempo, ρ é a massa específica, *c* é o calor especifico, θ é a temperatura e *t* é o tempo.

Para resolver a equação (1) é necessário impor as condições de contorno e as condições iniciais no modelo matemático. As condições gerais de contorno nas quais se encontra uma estrutura, sujeita à equação de Poisson, são as condições de Dirichlet e de Neumann. A condição de Dirichlet, ou temperatura prescrita, supõe conhecida para todo instante a temperatura em uma parte do contorno. Em análise de estruturas em situação de incêndio, a condição de Dirichlet não é importante, pois a mesma não leva em consideração a transferência de calor por convecção e radiação.

A condição de Neumann supõe que seja conhecido o fluxo de calor, $\dot{q}$, em uma parte do contorno em todo o instante. Matematicamente, essa condição pode ser escrita pela equação (2), ou seja, a derivada do campo de temperaturas em relação à normal à superfície no contorno, *n*.

$$-\lambda\frac{\partial\theta}{\partial n}=\dot{q} \quad (2)$$

Uma superfície com condição adiabática ou isolada termicamente pode ser simulada por meio da imposição de um fluxo nulo ($\dot{q}=0$).

Os fenômenos de convecção e radiação são incluídos no modelo numérico por meio da condição de contorno de Neumann, que pode ser escrita pela equação (3).

$$\dot{q}=\alpha_c\left(\theta-\theta_\infty\right)+\varepsilon\sigma\left(T^4-T_\infty^4\right) \quad (3)$$

Na equação α_c é o coeficiente de convecção, θ e θ_∞ são as temperaturas na estrutura e externa à estrutura, respectivamente, ε é a emissividade, σ é a constante de Stefan-Boltzmann, T e T_∞ são as temperaturas absolutas na estrutura e externa à estrutura, respectivamente.

Linearizando a parcela devido à radiação, a equação (3) pode ser reescrita por meio da equação,

$$\dot{q} = \alpha_c (\theta - \theta_\infty) + \alpha_r (\theta - \theta_\infty) = \alpha (\theta - \theta_\infty) \quad (4)$$

Na equação (4), α_r é o coeficiente de transmissão de calor por radiação fornecido pela equação (5).

$$\alpha_r = \varepsilon\sigma (T + T_\infty)(T^2 + T_\infty^2) \quad (5)$$

Como o coeficiente de transmissão de calor por radiação depende da temperatura da estrutura, o processo se torna iterativo.
A solução da equação diferencial (1) pode ser obtida numericamente por meio do método dos elementos finitos (*MEF*). Para a utilização do *MEF* é necessário escrever a formulação fraca do problema, a qual é obtida por meio da equação (6),

$$\int_\Omega w \left[\frac{\partial}{\partial x}\left(\lambda \frac{\partial \theta}{\partial x}\right) + \frac{\partial}{\partial y}\left(\lambda \frac{\partial \theta}{\partial y}\right) + \dot{Q} - \rho c \frac{\partial \theta}{\partial t} \right] d\Omega = 0 \quad (6)$$

Na equação (6), *w* é uma função arbitrária denominada de função peso e Ω é o domínio do problema.
Integrando por partes os dois primeiros termos da equação (6) e aplicando-se o Teorema de Gauss, obtém-se a equação (7).

$$\int_\Omega w \left[\frac{\partial}{\partial x}\left(\lambda \frac{\partial \theta}{\partial x}\right) + \frac{\partial}{\partial y}\left(\lambda \frac{\partial \theta}{\partial y}\right) \right] d\Omega = \int_S \left(w\lambda \frac{\partial \theta}{\partial x} l + w\lambda \frac{\partial \theta}{\partial y} m \right) dS - \int_\Omega \left(\frac{\partial w}{\partial x}\lambda \frac{\partial \theta}{\partial x} + \frac{\partial w}{\partial y}\lambda \frac{\partial \theta}{\partial y} \right) d\Omega \quad (7)$$

Na equação (7), *S* representa a região de contorno do problema e *l* e *m* são os cossenos diretores.
Substituindo a equação (7) em (6), tem-se a equação (8).

$$\int_\Omega w\dot{Q} d\Omega - \int_\Omega w\rho c \frac{\partial \theta}{\partial t} d\Omega + \int_S \left(w\lambda \frac{\partial \theta}{\partial x} l + w\lambda \frac{\partial \theta}{\partial y} m \right) dS - \int_\Omega \left(\frac{\partial w}{\partial x}\lambda \frac{\partial \theta}{\partial x} + \frac{\partial w}{\partial y}\lambda \frac{\partial \theta}{\partial y} \right) d\Omega = 0 \quad (8)$$

Discretizando-se o domínio do problema em um número finito de elementos e utilizando-se no Método de Galerkin o conjunto de funções de interpolação N_i como funções peso, a temperatura em qualquer ponto no interior do elemento finito pode ser aproximada pela equação (9).

$$\theta(x, y, t) = \sum_i^n N_i \theta \quad (9)$$

Na equação (9), *n* é o número de nós do elemento, $N_i = N_i(x, y)$ são as funções de interpolação e θ_i são as temperaturas nodais do elemento.
Substituindo a equação (9) em (8), chega-se no sistema de equações (10), que representa o equilíbrio térmico em cada elemento finito.

$$-\int_{A_e} \left[\lambda \frac{\partial N_i}{\partial x}\frac{\partial \theta}{\partial x} + \lambda \frac{\partial N_i}{\partial y}\frac{\partial \theta}{\partial y} - N_i\dot{Q} + N_i\rho c \frac{\partial \theta}{\partial t} \right] dA_e + \int_{S_e} N_i \lambda \frac{\partial \theta}{\partial x} l dS_e + \int_{S_e} N_i \lambda \frac{\partial \theta}{\partial y} m dS_e = 0 \quad \text{para i= 1 até n,} \quad (10)$$

Na equação (9), A_e e S_e representam a área e a superfície do domínio do elemento.
A derivada do campo de temperaturas em relação à normal à superfície no contorno, *n*, pode ser escrita em função dos cossenos diretores, *l* e *m*, por meio da equação (11).

$$\frac{\partial \theta}{\partial n} = \frac{\partial \theta}{\partial x} l + \frac{\partial \theta}{\partial y} m \quad (11)$$

Substituindo as equações (2), (4) e (11) na equação (10), obtém-se a expressão (12),

$$\int_{A_e} N_i \dot{Q} dA_e - \int_{A_e} N_i \rho c \frac{\partial \theta}{\partial t} dA_e - \int_{A_e} \left[\lambda \frac{\partial N_i}{\partial x}\frac{\partial \theta}{\partial x} + \lambda \frac{\partial N_i}{\partial y}\frac{\partial \theta}{\partial y} \right] dA_e - \int_{S_e} N_i \alpha (\theta - \theta_\infty) dS_e = 0 \quad (12)$$

Definindo-se o vetor de funções de interpolação $\boldsymbol{N}$ e o vetor de temperaturas nodais $\boldsymbol{\theta}$ por meio das expressões (13).

$$\boldsymbol{N} = [N_1 \quad N_2 \quad \ldots \quad N_{n-1} \quad N_n]$$
$$\theta = [\theta_1 \quad \theta_2 \quad \ldots \quad \theta_{n-1} \quad \theta_n]^T \quad (13)$$

onde *n* é o número de nós do elemento e N_i são as funções de interpolação do elemento finito.
Assim, pode-se reescrever a equação (9) na forma matricial por meio da equação (14).

$$\theta(x,y,t) = \sum_{i=1}^{n} N_i \theta_i = \boldsymbol{N}\theta \quad (14)$$

Define-se também a matriz de condutividade do material, para o caso de material isótropo, por meio da equação (15).

$$\lambda = \begin{bmatrix} \lambda & 0 \\ 0 & \lambda \end{bmatrix} \quad (15)$$

e o vetor gradiente pela equação (16).

$$\nabla = \begin{Bmatrix} \dfrac{\partial}{\partial x} \\ \dfrac{\partial}{\partial y} \end{Bmatrix} \quad (16)$$

Inserindo-se as equações (13) a (16) na equação (12) e rearranjando os termos, obtém-se o sistema de equações (17).

$$\int_{A_e} \boldsymbol{N}^T \rho c \boldsymbol{N} \frac{\partial \theta}{\partial t} dA_e + \int_{A_e} (\nabla \boldsymbol{N})^T \lambda \nabla \boldsymbol{N} \theta \, dA_e + \int_{S_e} \boldsymbol{N}^T \alpha \boldsymbol{N} \theta \, dS_e = \int_{A_e} \boldsymbol{N}^T \dot{Q} \, dA_e + \int_{S_e} \boldsymbol{N}^T \alpha \theta_\infty dS_e \quad (17)$$

O sistema de equações (17) pode ser reescrito de forma matricial por meio da equação (18).

$$\boldsymbol{C}\dot{\theta} + \boldsymbol{K}\theta = \boldsymbol{F} \quad (18)$$

Na equação (18), $\dot{\boldsymbol{\theta}}$ é a primeira derivada do campo de temperaturas em relação ao tempo.
A matriz de capacitância total ($\boldsymbol{K}$) do elemento é dada pela pela equação (19).

$$\boldsymbol{K} = \boldsymbol{K}_{cond} + \boldsymbol{K}_{conv\_rad} \quad (19)$$

onde a matriz de condutividade do elemento é dada pela equação (20).

$$\boldsymbol{K}_{cond} = \int_{A_e} \boldsymbol{B}^T \lambda \boldsymbol{B} dA_e \quad (20)$$

em que,

$$\boldsymbol{B} = \nabla \boldsymbol{N} \quad (21)$$

e a matriz devido aos efeitos combinados de convecção e radiação do elemento é dada pela equação (22).

$$\boldsymbol{K}_{conv\_rad} = \int_{S_e} (\alpha_c + \alpha_r) \boldsymbol{N}^T \boldsymbol{N} \theta \, dS_e \quad (22)$$

Define-se capacidade térmica do material como sendo o produto entre a massa específica (ρ) e o calor específico (c). Assim, a matriz de capacidade térmica ($\boldsymbol{C}$) do elemento é dada pela equação (23).

$$\boldsymbol{C} = \int_{A_e} \boldsymbol{N}^T \rho c \boldsymbol{N} dA_e \quad (23)$$

O vetor de ações térmicas consistentes ($\boldsymbol{F}$) é dado pela expressão (24).

$$\boldsymbol{F} = \int_{A_e} \boldsymbol{N}^T \dot{Q} \, dA_e + \int_{S_e} \boldsymbol{N}^T (\alpha_c + \alpha_r) \theta_\infty dS_e \quad (24)$$

Na equação (23), θ_∞ é a temperatura externa à estrutura.
As matrizes $\boldsymbol{N}$ e $\boldsymbol{B}$ dependem do tipo de elemento utilizado na discretização da estrutura.
No programa ATERM utilizam-se elementos retangulares e triangulares planos de quatro e três nós, respectivamente, e elementos especiais de barra de dois nós para a consideração dos efeitos de transferência de calor por convecção e radiação, os quais podem ser justapostos em qualquer face dos elementos planos. Esses elementos estão brevemente descritos nos próximos itens. Maiores detalhes sobre os elementos finitos utilizados e a implementação computacional podem ser obtidos em Pierin [2].

2.1 Elemento retangular de quatro nós

O elemento finito retangular plano de quatro nós de lados *2a* por *2b* utilizado neste trabalho está representado na Figura 1.
As funções de interpolação N_i estão definidas por meio da equação (25).

Figura 1 – Elemento retangular de quatro nós

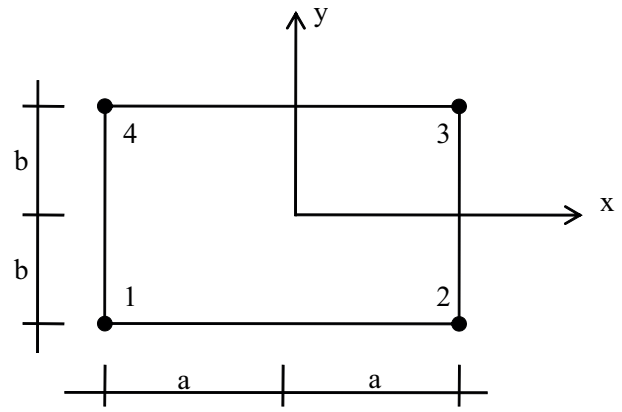

$$N_i = \frac{1}{4}\left(1+\frac{x}{x_i}\right)\left(1+\frac{y}{y_i}\right) \text{ para } i = 1,2,3,4 \qquad (25)$$

Substituindo as equações (15), (21) e (25) na equação (20) obtém-se a equação (26) que representa a matriz de condutividade do elemento retangular plano de quatro nós.

$$\boldsymbol{K}_{cond} = \frac{\lambda a}{6b}\begin{bmatrix} 2 & -2 & -1 & 1 \\ -2 & 2 & 1 & -1 \\ -1 & 1 & 2 & -2 \\ 1 & -1 & -2 & 2 \end{bmatrix} + \frac{\lambda b}{6a}\begin{bmatrix} 2 & 1 & -1 & -2 \\ 1 & 2 & -2 & -1 \\ -1 & -2 & 2 & 1 \\ -2 & -1 & 1 & 2 \end{bmatrix} \qquad (26)$$

Figura 2 – Elemento triangular

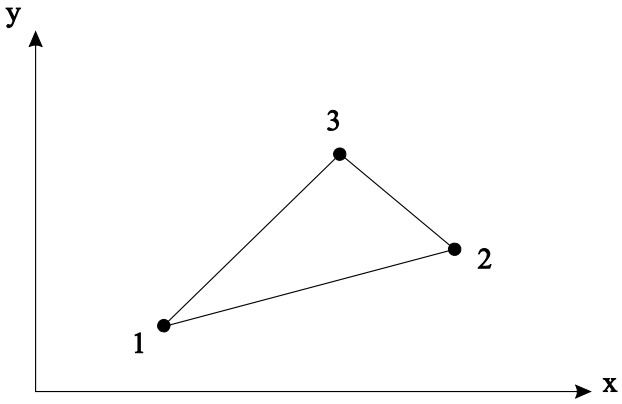

Substituindo a equação (25) na equação (23) obtém-se a matriz de capacidade térmica deste elemento, a qual é expressa pela equação (27),

$$\boldsymbol{C} = \frac{\rho cab}{36}\begin{bmatrix} 4 & 2 & 1 & 2 \\ 2 & 4 & 2 & 1 \\ 1 & 2 & 4 & 2 \\ 2 & 1 & 2 & 4 \end{bmatrix} \qquad (27)$$

2.2 Elemento triangular

O elemento finito triangular utilizado no programa ATERM possui três nós identificados por *1, 2* e *3* e está representado na Figura 2. As funções N_i utilizadas para interpolação das temperaturas nodais no interior do elemento finito triangular são definidas por meio da equação (28).

$$N_i = \frac{1}{2A}\left(a_i + b_i x + c_i y\right) \text{ para } i = 1,2,3 \qquad (28)$$

Na equação (28), A representa a área do elemento finito e os coeficientes a_i, b_i e c_i são fornecidos pelas expressões (29).

$$\begin{aligned} a_1 &= X_2Y_3 - X_3Y_2; \quad b_1 = Y_2 - Y_3; \quad b_1 = X_3 - X_2 \\ a_2 &= X_3Y_1 - X_1Y_3; \quad b_2 = Y_3 - Y_1; \quad b_2 = X_1 - X_3 \\ a_3 &= X_1Y_2 - X_2Y_1; \quad b_3 = Y_1 - Y_2; \quad b_3 = X_2 - X_1 \end{aligned} \qquad (29)$$

Nas expressões (29), X_i e Y_i representam as coordenadas cartesianas do nó *i*.

Substituindo as equações (15), (21) e (28) na equação (20) obtém-se a equação (30) que representa a matriz de condutividade do elemento triangular plano.

$$\boldsymbol{K}_{cond} = \frac{\lambda}{4A}\begin{bmatrix} b_1^2 + c_1^2 & b_1b_2 + c_1c_2 & b_1b_3 + c_1c_3 \\ b_1b_2 + c_1c_2 & b_2^2 + c_2^2 & b_2b_3 + c_2c_3 \\ b_1b_3 + c_1c_3 & b_2b_3 + c_2c_3 & b_3^2 + c_3^2 \end{bmatrix} \qquad (30)$$

Figura 3 – Elemento finito de convecção e radiação

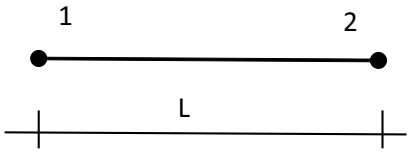

Substituindo a equação (28) na equação (23) obtém-se a matriz de capacidade térmica deste elemento, expressa pela equação (31),

$$\boldsymbol{C} = \frac{\rho c A}{12}\begin{bmatrix} 2 & 1 & 1 \\ 1 & 2 & 1 \\ 1 & 1 & 2 \end{bmatrix} \quad (31)$$

2.3 Elemento especial de barra de dois nós

As condições de contorno de Neumann podem ser impostas ao modelo de elementos finitos por meio de um elemento linear de dois nós de comprimento *L*, conforme mostra a Figura 3. Ressalta-se que para o modelo ser coerente, o elemento linear de dois nós tem que coincidir com as faces do elemento finito utilizado para discretizar a estrutura.
A matriz de funções de interpolação para o elemento finito de convecção e radiação é definida pela equação (32).

$$\boldsymbol{N} = \begin{bmatrix} 1 - \frac{x}{L} & \frac{x}{L} \end{bmatrix} \quad (32)$$

Deve-se observar que o elemento linear de convecção é totalmente compatível com o elemento retangular de quatro nós formulado anteriormente, pois esse utiliza funções lineares para interpolar as temperaturas ao longo do lado do elemento.
Substituindo a equação (32) na expressão (22), a matriz de convecção e o vetor de ações térmicas consistentes devido ao fluxo de calor convectivo são fornecidos pelas equações (33) e (34), respectivamente,

$$\boldsymbol{K}_{conv\_rad} = \frac{(\alpha_c + \alpha_r)L}{6}\begin{bmatrix} 2 & 1 \\ 1 & 2 \end{bmatrix} \quad (33)$$

$$\boldsymbol{F}_{conv\_rad} = (\alpha_c + \alpha_r)\theta_\infty \begin{bmatrix} L/2 \\ L/2 \end{bmatrix} \quad (34)$$

3. Cavidades

Em alguns elementos estruturais há presença de ar enclausurado em cavidades, tais como lajes alveolares, blocos cerâmicos e lajes nervuradas preenchidas com blocos EPS. A presença de cavidades na estrutura provoca a transferência de calor por convecção e radiação devido ao aquecimento do ar enclausurado.
Discretizando o domínio da estrutura a ser analisada termicamente em elementos finitos planos e o contorno da cavidade em elementos finitos especiais de dois nós, conforme mostra a Figura 4, pode-se obter a temperatura do ar no interior da cavidade a partir das temperaturas nodais por meio da equação (35).

$$\sum_{i=1}^{N}\left(\alpha_i\left(\theta_{cav} - \theta_i\right) + \varepsilon_i\sigma\left(T_{cav}^4 - T_i^4\right)\right)L_i + \rho_{ar}c_{ar}A_{cav}\left(\theta_{cav} - \theta_{cav}^{t-1}\right) = 0 \quad (35)$$

Na equação (35), α_i é o coeficiente de convecção do elemento *i*, θ_i e θ_{cav} são as temperaturas no elemento e do ar, respectivamente, ε_i é a emissividade, σ é a constante de Stefan-Boltzmann, T_i e T_{cav} são as temperaturas absolutas na estrutura e externa à estrutura, respectivamente, θ_{cav}^{t-1} é a temperatura do ar no interior da cavidade no instante anterior, A_{cav} é a área da cavidade, c_{ar} e ρ_{ar} são o calor especifico e a massa especifica do ar, respectivamente. L_i é o comprimento do elemento finito especial.
A equação (35) pode ser reescrita por meio da equação (36).

$$A\theta_{cav}^4 + B\theta_{cav} - C = 0 \quad (36)$$

Figura 4 – Malha de elementos finitos

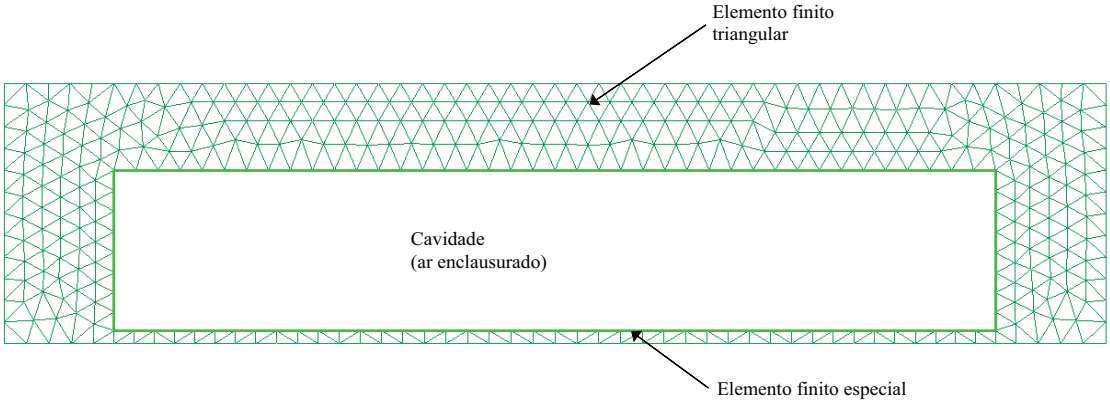

As variáveis *A, B* e *C* são dadas pelas equações (37).

$$A = \sum_{i=1}^{N} \sigma \varepsilon_i L_i$$

$$B = \sum_{i=1}^{N} \alpha_i L_i + \rho_{ar} c_{ar} A_{cav} \qquad (37)$$

$$C = \sum_{i=1}^{N} \alpha_i L_i \theta_i + \sum_{i=1}^{N} \sigma \varepsilon_i L_i T_i^4 + \rho_{ar} c_{ar} A_{cav} \theta_{cav}^{t-1}$$

4. Pré-processamento

A entrada de dados necessária para o programa ATERM é feita por meio de arquivos textos que contém as informações da estrutura bidimensional a ser analisada termicamente. Essas informações se resumem às coordenadas nodais, à conectividade dos elementos e às propriedades térmicas dos materiais. Para facilitar a criação desse arquivo de entrada de dados, foi criado com base no programa GiD [3] alguns modelos de geometria, tais como seção retangular e seção T, como mostra a Figura 5. Nesses modelos é necessário informar apenas as dimensões das seções, dos elementos finitos e o tipo de material.

A exposição ao fogo pode ser configurada diretamente no modelo, indicando apenas as faces expostas ao incêndio-padrão e as faces expostas a uma temperatura constante, conforme mostra a Figura 6. Também devem ser informados os coeficientes de convecção e emissividade para a consideração da transferência de calor por convecção e radiação.

As propriedades térmicas dos materiais, tais como a condutividade, a massa específica, a densidade e o coeficiente de redução da resistência, são informadas por meio de tabelas em função da temperatura conforme mostra a Figura 7. Pode-se também definir materiais cujas propriedades térmicas não dependem da temperatura.

Outros dados necessários à análise térmica, tais como o tempo total de exposição ao incêndio, incremento de tempo, temperatura inicial da estrutura, coeficiente α para escolha do método de integração temporal, tolerância para a convergência das temperaturas, incremento de tempo para impressão dos resultados, devem ser informados conforme mostra a

Figura 5 – Modelos para a criação da geometria

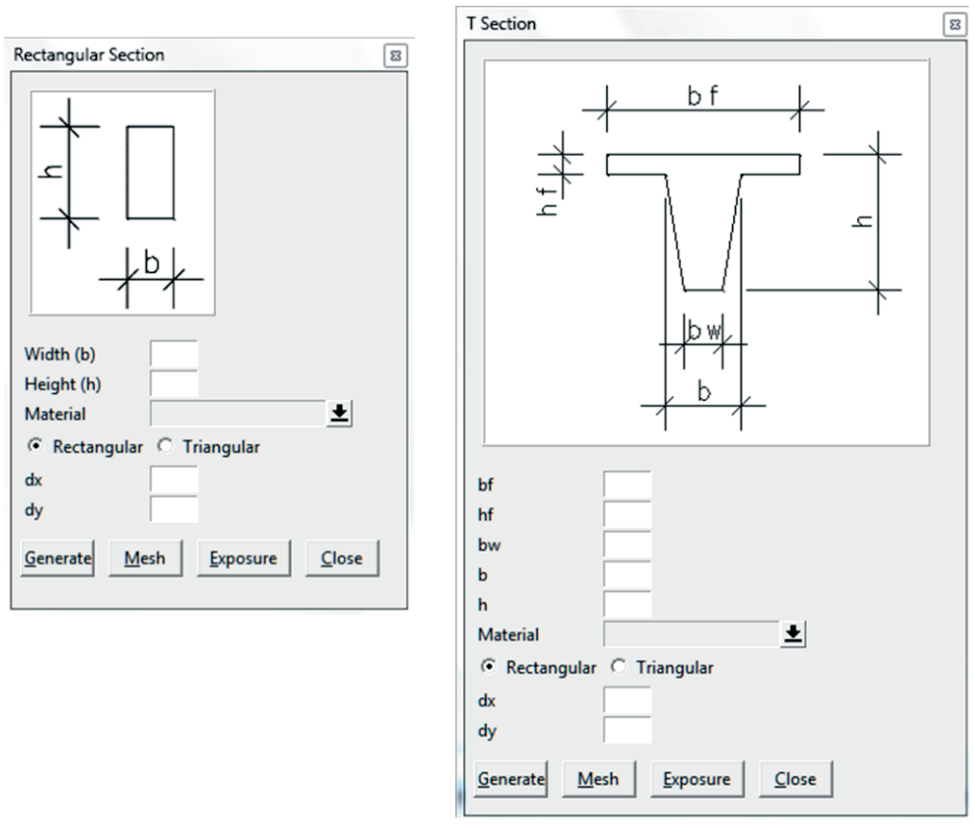

Figura 6 – Exposição ao incêndio

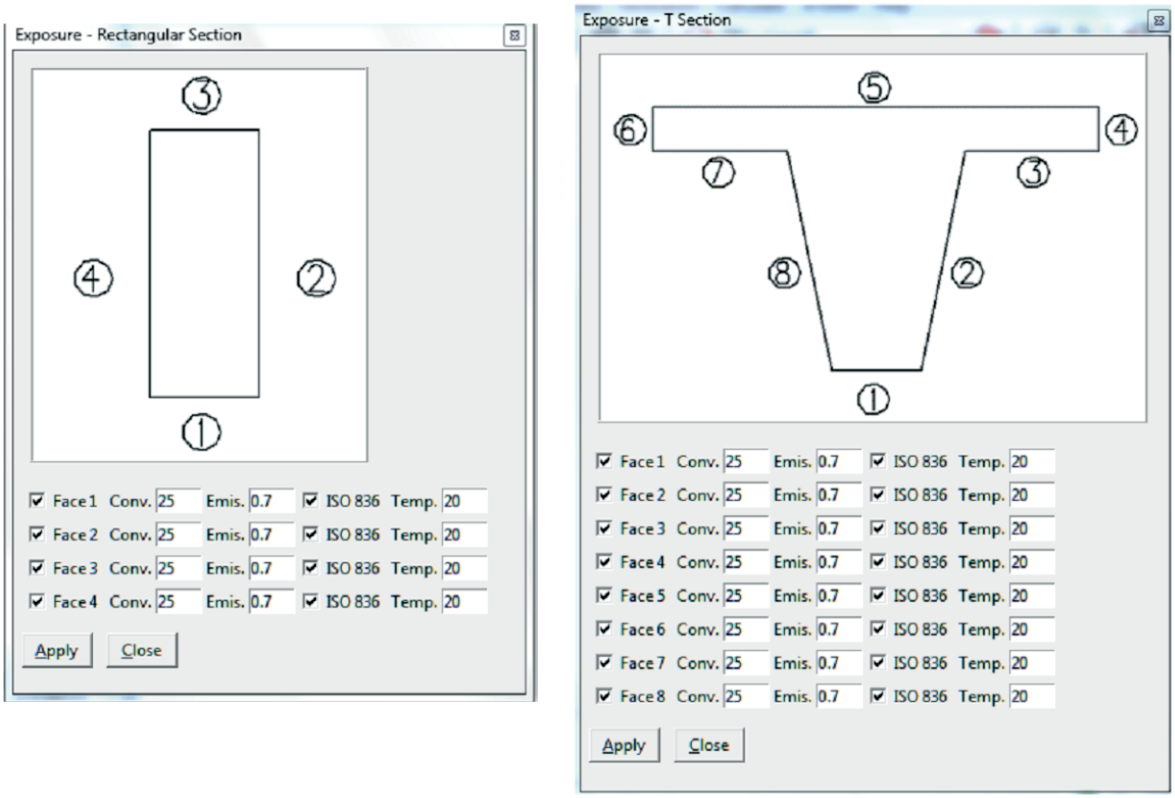

Figura 7 – Propriedades térmicas dos materiais

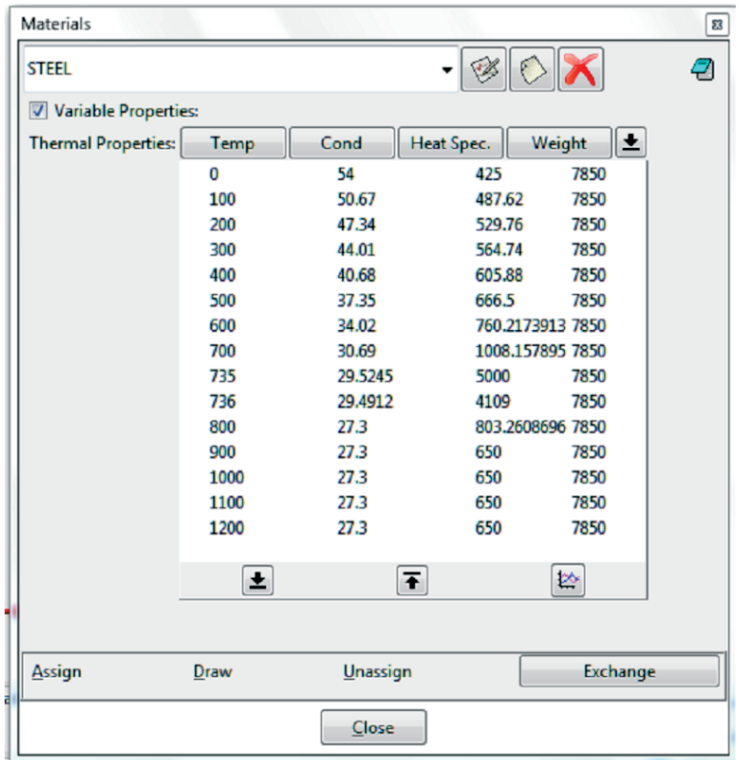

Figura 8 – Outros dados

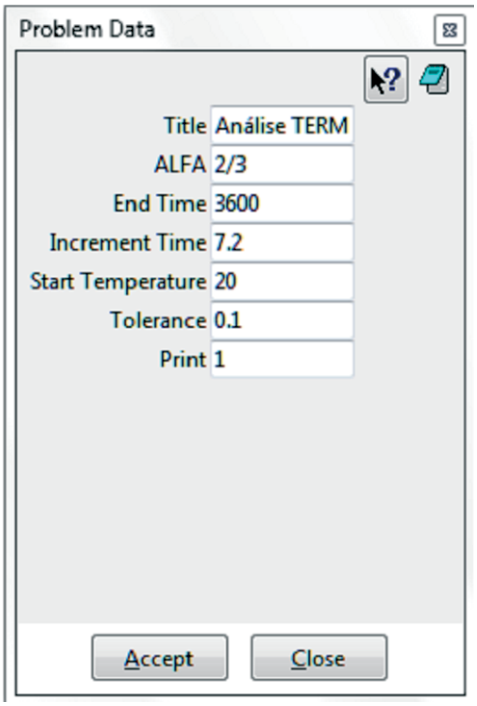

Figura 8. O coeficiente α varia de 0 (Método de Euler Implícito) a 1 (Método de Euler Explícito) e define a estabilidade numérica para a integração ao longo do tempo. O programa STC utiliza α=2/3, conhecido como Método de Galerkin.

Figura 9 – Geometria da viga

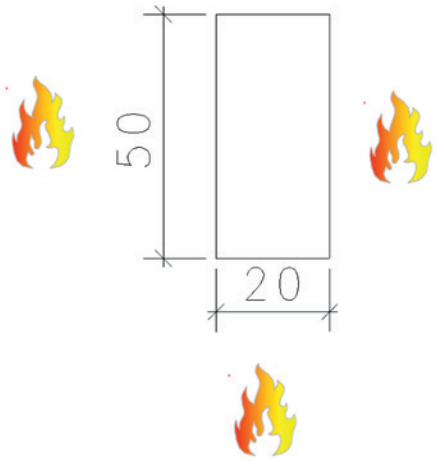

Figura 10 – Influência da malha na temperatura nodal

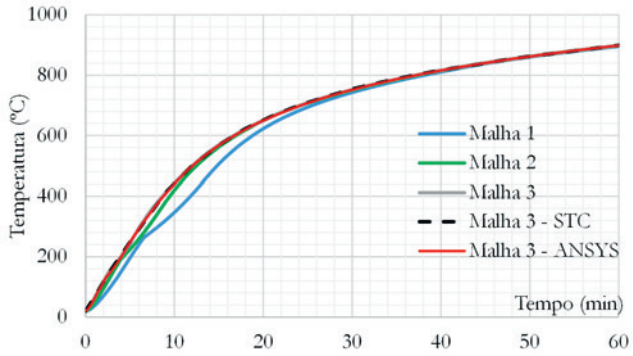

5. Simulação numérica

Para validar o programa desenvolvido neste trabalho, foram realizadas três simulações numéricas cujos resultados foram comparados aos obtidos por meio dos programas STC [4] e ANSYS [6]. As propriedades térmicas adotadas para o concreto tiveram por base a ABNT NBR 15200:2012 [1]. Nos exemplos deste trabalho, utilizou-se concreto silicoso com teor de umidade igual a 1,5% em peso.
Em todos os exemplos, a ação térmica é determinada de acordo com a curva de incêndio-padrão ISO 834 [8].

5.1 Viga de concreto

Como primeiro exemplo, é analisado o aquecimento de uma viga de concreto de seção retangular de dimensões 20x50 cm, conforme mostra a Figura 9. Admite-se que o incêndio atue em três faces da viga. Considera-se que a massa especifica do concreto é variável com a temperatura [1] e para 20 ºC a massa especifica é igual a 2400 kg/m³, conforme recomendações da ABNT NBR 6118:2014 [9]. O fator de emissividade e o coeficiente de convecção foram adotados iguais a 0,7 e 25 W/m².ºC, respectivamente. Adota-se para temperatura inicial da estrutura o valor de 20ºC.

Figura 11 – Geometria da laje nervurada

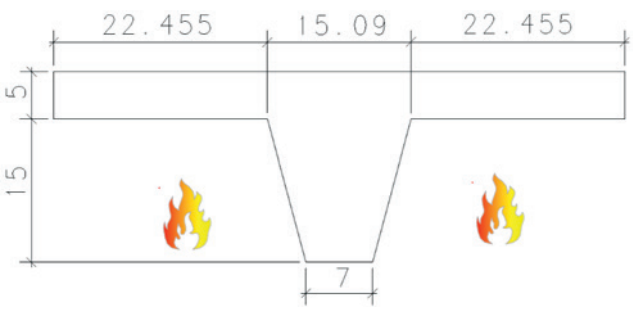

Figura 12 – Modelo analisado

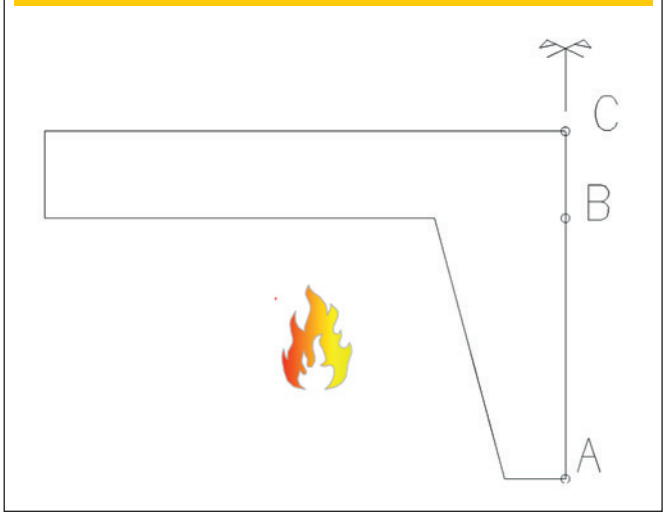

A estrutura foi discretizada em elementos quadrados, sendo que para o programa ATERM foram utilizadas 3 malhas: na Malha 1 utilizaram-se elementos de 5 cm de lado, na Malha 2 elementos de 2,5 cm de lado e, na Malha 3, elementos de 1 cm de lado. Para a modelagem nos programas ANSYS e STC utilizou-se apenas a Malha 3. A Figura 10 apresenta a influência do refinamento da malha na evolução da temperatura em função do tempo no nó localizado na metade do menor lado aquecido. Observa-se que, com o refinamento da malha, as temperaturas se elevam um pouco até o instante t = 28 minutos e após esse instante as temperaturas obtidas para as diferentes malhas são praticamente iguais. Nota-se que a solução tende a convergir com o refinamento da malha, sendo que para a malha 3 os resultados obtidos pelos programas ATERM, ANSYS e STC são praticamente iguais.

5.2 Laje nervurada

A Figura 11 mostra a geometria da laje nervurada analisada termicamente (dimensões em cm). A parte inferior da laje está exposta ao fogo. O fator de emissividade e o coeficiente de convecção foram adotados iguais a 0,7 e 25 W/m².ºC, respectivamente, conforme recomendações do Eurocode 2 parte 1.2 [5]. Na face superior da laje, não exposta ao incêndio, os fenômenos combinados de convecção e radiação foram simulados por α_c = 9 W/m² °C [10]. Adota-se 20ºC para temperatura inicial da estrutura. Devido à simetria, apenas a metade da laje foi modelada, sendo que a linha de simetria foi considerada adiabática.

Figura 13 – Evolução da temperatura em função do tempo

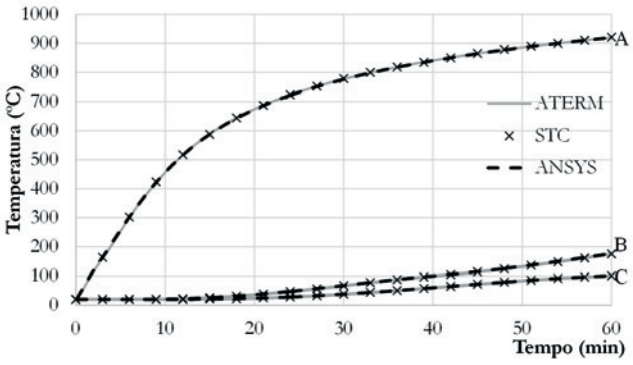

A Figura 13 mostra a variação da temperatura nodal em função do tempo obtida pelos programas ATERM e STC para três pontos distintos localizados na linha de simetria da laje (conforme mostra a Figura 12): ponto A – na base da nervura; ponto B – na altura da junção da nervura e a capa; ponto C – na face superior da laje A laje foi discretizada em elementos triangulares de 0,5 cm de lado, sendo gerados 1653 elementos no STC e 1809 elementos no ATERM A diferença do número de elementos gerados pelos programas deve-se ao fato de os programas utilizarem geradores de malha distintos. Observa-se que os resultados obtidos pelos programas são praticamente iguais. Observa-se também uma boa correlação entre os resultados obtidos pelos programas ATERM e ANSYS.

Figura 14 – Campo de temperaturas para 60 minutos: (a) ATERM e (b) STC

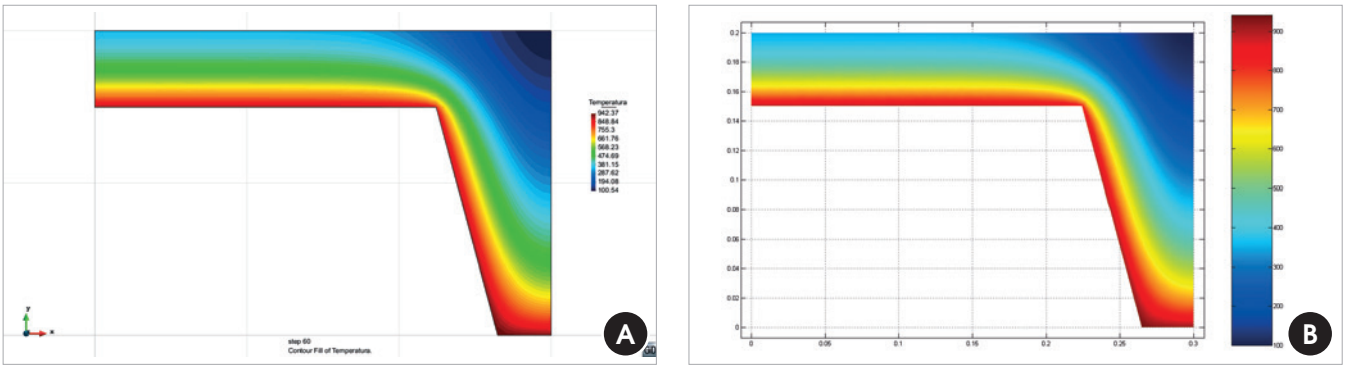

Figura 15 – Modelo com EPS/placa cimentícia (dimensões em mm)

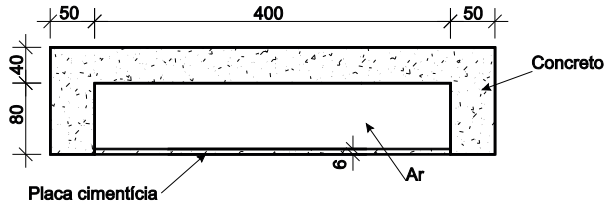

A Figura 14 mostra o campo de temperaturas após 60 minutos de incêndio obtidos pelos programas ATERM e STC.

5.3 *Projeto de lajes nervuradas com preenchimento*

No Brasil também são usadas lajes nervuradas com preenchimento com EPS sobre placa cimentícia, conforme mostra a Figura 15. O EPS quando aquecido se decompõe rapidamente resultando em um grande espaço preenchido de ar enclausurado. O ar enclausurado contribui na transferência de calor entre a placa cimentícia, a qual se encontra em temperaturas mais elevadas, e a capa de concreto. Essa transferência de calor pode ser contabilizada no modelo numérico por meio do procedimento indicado no item 3 deste trabalho.

Na face diretamente aquecida pelo incêndio foi aplicada a curva padronizada pela ISO 834 [7] e, na face não exposta diretamente ao calor, foi tomada uma combinação de convecção e radiação, simulada por α_c = 9 W/m² °C.

As propriedades térmicas da placa cimentícia utilizadas nas análises foram: condutividade térmica igual a 2,22 W/mºC, calor específico igual a 840 J/kg K e densidade igual a 1200 kg/m³ [11].

Analisou-se a variação da temperatura em dois pontos, conforme mostra a Figura 16: ponto A – ponto médio da face superior da capa de concreto e ponto B – localizado na chapa de aço. O EPS foi admitido totalmente consumido pelo fogo e desconsiderado na análise.

A variação da temperatura em função do tempo de exposição ao incêndio nos pontos A e B está apresentada na Figura 17. Verifica-se, novamente, uma boa correlação entre os resultados obtidos pelos programas ATERM e STC.

Observa-se que a consideração do ar enclausurado no modelo provoca um aquecimento na face superior da laje na região entre as nervuras. Os campos de temperaturas aos 60 minutos de incêndio-padrão na face inferior da laje com e sem a consideração do ar enclausurado estão apresentados nas Figuras 18 e 19, respectivamente.

A não consideração do ar enclausurado, por meio de cavidades, não provoca o aquecimento na face superior da laje na região entre as nervuras, ou seja, após 60 minutos de incêndio a face superior da laje está à temperatura ambiente. Há apenas um leve aumento de temperaturas na face superior da laje região das nervuras.

Na realidade, o ar enclausurado provoca uma transferência de calor por convecção e radiação entre as superfícies aquecida (placa cimentícia) e a não exposta ao incêndio (capa de concreto). Este exemplo demonstra que essa transmissão de calor pode ser modelada por meio de cavidades.

Figura 16 – Pontos de controle para a análise

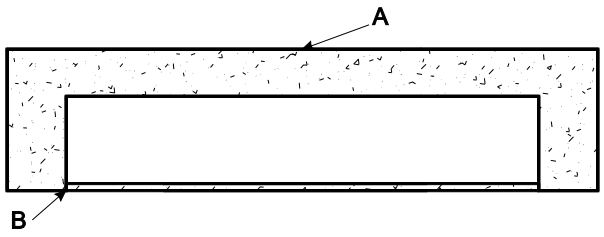

6. Conclusão

Neste trabalho apresentou-se a formulação do Método dos Elementos Finitos aplicado à análise térmica não linear de estruturas bidimensionais, empregada na elaboração do programa de computador ATERM. Esse tipo de análise é fundamental no estudo de estruturas em situação de incêndio.

Os resultados obtidos pelos autores foram validados com o programa STC [4] e por meio do ANSYS [6]. Observou-se que os resultados obtidos pelos programas apresentam uma ótima correlação em todos os exemplos realizados.

Notou-se também que, dependendo da malha utilizada, os resultados podem não representar o comportamento físico. Assim, recomenda-se que se realize um estudo de malhas geométrica e temporal antes de se proceder à análise térmica.

Em algumas situações, tais como em lajes nervuradas preenchidas com material inerte e em lajes nervuradas, há presença de cavidades no interior do elemento estrutural. Essas cavidades são preenchidas por ar que, quando aquecidos, transferem calor, por convecção e radiação, para as regiões próximas. Na análise por elementos finitos, a transferência de calor por meio do ar enclausurado pode ser considerada, tanto no programas ATERM como no STC.

O desempenho computacional do programa ATERM mostrou que este programa é bastante eficaz em relação ao STC, tendo um tempo de processamento bem menor.

Figura 17 – Evolução da temperatura em função do tempo nos pontos A e B

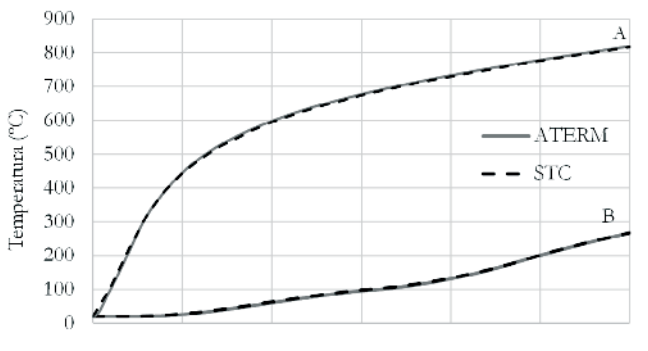

Figura 18 – Campo de temperaturas aos 60 minutos com a presença de cavidades

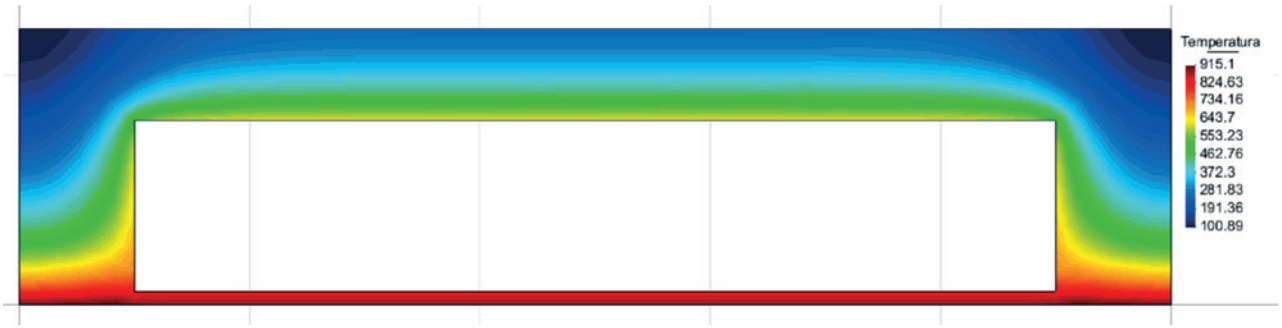

Figura 19 – Campo de temperaturas aos 60 minutos sem a presença de cavidades

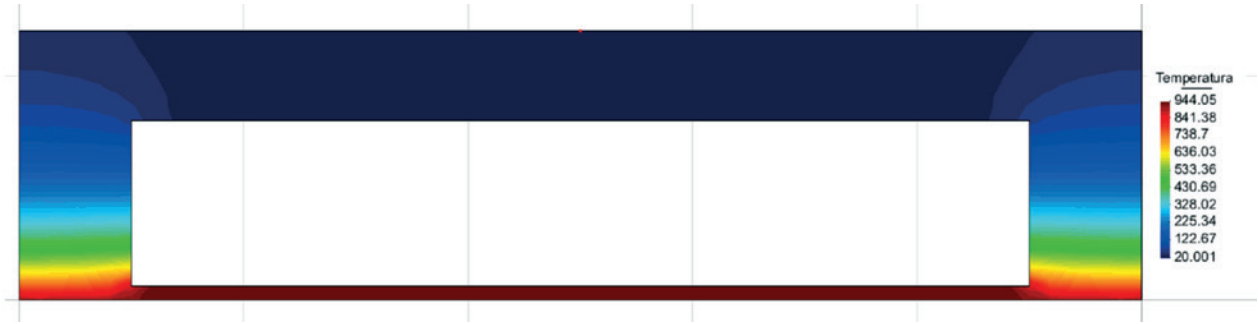

Por meio do programa GiD foram criadas várias seções para entrada de dados, tais como retangular e seção T, as quais facilitam a criação da geometria e da malha de elementos finitos. Esses modelos básicos podem ser utilizados para a definição de outras geometrias mais complexas.

7. Agradecimentos

Agradece-se à FAPESP – Fundação de Amparo à Pesquisa do Estado de São Paulo, ao CNPq – Conselho Nacional de Desenvolvimento Científico e Tecnológico e à Tuper.

8. Referências bibliográficas

[01] ASSOCIAÇÃO BRASILEIRA DE NORMAS TÉCNICAS. NBR 15200: Projeto de estruturas de concreto em situação de incêndio. Rio de Janeiro, 2012.

[02] PIERIN; I. A instabilidade de perfis formados a frio em situação de incêndio. Tese de Doutorado. Escola Politécnica. Universidade de São Paulo. 2011.

[03] International Center for Numerical Methods in Engineering (CIMNE). GiD 10.0 Users Manual. http://gid.cimne.upc.es/., 2011.

[04] FIRE SAFETY DESIGN (FSD). TCD 5.0 User's manual. Lund: Fire Safety Design AB, 2007.

[05] EUROPEAN COMMITTEE FOR STANDARDIZATION. EN 1992-1-2: Eurocode 2: Design of concrete structures - part 1.2: general actions - actions on structures exposed to fire. Brussels: CEN, 2004.

[06] Ansys INC, (2004). Ansys Realese 9.0 – Documentation,

[07] SILVA; V. P. Projeto de estruturas de concreto em situação de incêndio. Editora Blucher, 2012.

[08] INTERNATIONAL ORGANIZATION FOR STANDARDIZATION. ISO 834: Fire-resistance tests: elements of building construction - part 1.1: general requirements for fire resistance testing. Geneva, 1999. 25 p. (Revision of first edition ISO 834:1975).

[09] ASSOCIAÇÃO BRASILEIRA DE NORMAS TÉCNICAS. NBR 6118: Projeto de estruturas de concreto. Rio de Janeiro, 2014.

[10] EUROPEAN COMMITTEE FOR STANDARDIZATION. EN 1991-1-2: Eurocode 1: Actions on structures - part 1.2: general actions - actions on structures exposed to fire. Brussels: CEN, 2002.

[11] PIERIN; I., SILVA; V. P. Fire design of composite ribbed slabs. Revista IBRACON de Estruturas e Materiais. v. 7, p. 178-192, 2014.

Volume 8, Number 1 (February 2015) p. 49-65 • ISSN 1983-4195
REVISTA IBRACON DE ESTRUTURAS E MATERIAIS
IBRACON STRUCTURES AND MATERIALS JOURNAL

A bi-dissipative damage model for concrete

Um modelo de dano bi-dissipativo para o concreto


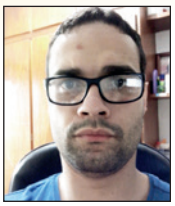

J. J. C. PITUBA [a]
Julio_pituba@ufg.br

W. M. PEREIRA JÚNIOR [b]
w.junioreng@gmail.com

Abstract

This work deals with an improvement of an anisotropic damage model in order to analyze reinforced concrete structures submitted to reversal loading. The original constitutive model is based on the fundamental hypothesis of energy equivalence between real and continuous media following the concepts of the Continuum Damage Mechanics. The concrete is assumed as an initial elastic isotropic medium presenting anisotropy, permanent strains and bimodularity induced by damage evolution. In order to take into account the bimodularity, two damage tensors governing the rigidity in tension or compression regimes are introduced. However, the original model is not capable to simulate the influence of the previous damage processes in compression regimes. In order to avoid this problem, some conditions are introduced to simulate the damage unilateral effect. It has noted that the damage model is agreement with to micromechanical theory conditions when dealing to unilateral effect in concrete material. Finally, the proposed model is applied in the analyses of reinforced concrete framed structures submitted to reversal loading. These numerical applications show the good performance of the model and its potentialities to simulate practical problems in structural engineering.

Keywords: damage mechanics, unilateral effect, concrete structures, structural failure.

Resumo

Este trabalho trata do aperfeiçoamento de um modelo dano anisótropo de modo a analisar estruturas em concreto armado submetidas à inversão de carregamento. O modelo constitutivo original é baseado nas hipóteses fundamentais de equivalência de energia entre meio real danificado e meio contínuo equivalente segundo os conceitos da Mecânica do Dano no Contínuo. O concreto é assumido como um meio inicialmente elástico e isótropo que passa a apresentar comportamento mecânico anisótropo, plástico e bimodular induzidos pelos processos de danificação. Com o intuito de se levar em conta a bimodularidade do meio, são propostos dois tensores de dano governando a rigidez em regimes de tração e de compressão. Entretanto, o modelo original não é capaz de simular a influência de processos prévios de danificação em regimes de compressão. Objetivando contornar este problema, algumas condições são introduzidas no modelo para simular o efeito unilateral causado pelo dano. Observa-se que o modelo de dano está de acordo com as condições obtidas da Teoria Micromecânica quando tratando do efeito unilateral em materiais frágeis, como o concreto. Finalmente, o modelo de dano proposto é aplicado na análise de estruturas de pórticos de concreto armado submetidas a cargas com inversão de sinal. Os resultados comprovam o bom desempenho do modelo e potencialidades para simular problemas práticos da Engenharia Estrutural.

Palavras-chave: mecânica do dano, efeito unilateral, estruturas de concreto, falha estrutural.

[a] *Department of Civil Engineering, Federal University of Goiás, Campus Catalão, Catalão, Goiás, Brazil;*
[b] *School of Civil Engineering, Federal University of Goiás, Campus Goiânia, Goiânia, Goiás, Brazil.*

Received: 25 May 2014 • Accepted: 15 Dec 2014 • Available Online: 03 Feb 2014

1. Introduction

The Continuum Damage Mechanics (CDM) has already proved to be a suitable tool for simulating the material deterioration in equivalent continuous media due exclusively to microcracking process. In this work, for modeling the concrete behavior, it can be assumed that the concrete belongs to the category of materials which can be considered initially isotropic and unimodular presenting different behaviors in tension and compression when damaged. A formulation of constitutive laws for isotropic and anisotropic elastic materials presenting different behaviors in tension and compression under small deformations was proposed in Curnier [1] for two and three-dimensional cases. The authors have considered a bimodular hyperelastic material defining an elastic potential energy density W which must be once continuously differentiable (whole wise), but only piecewise twice continuously differentiable. In this way, the model is able to produce different response in tension and compression. Pituba [2] has extended that formulation in order to take into account the damage effects. Accordingly with, the bulk (λ_{ab}) and shear (μ_a) moduli are considered as functions of the damage state, so that the stress-strain relationship would be influenced by damage variables. Moreover, the hypersurface $g(\varepsilon, D_i)$ adopted as the criterion for identification of the constitutive responses in compression or tension would be also influenced by the damage variables. Then, a damage constitutive model accounting for induced anisotropy and bimodular elastic response for the concrete was derived from Pituba [2] and its potentialities for 1D and 2D analyses are discussed in Pituba [3], Pituba and Fernandes [4], Pituba and Lacerda [5] and Pituba [6]. Besides, the simulations of experimental tests in uniaxial, biaxial and triaxial stress tests are reported in Pituba and Fernandes [4]. The original version of the damage model is bimodular in the sense that presents different elasticity tensors in tension and compression. Thus, the model is potentially capable to simulate the stiffness recovery when the medium is submitted to a reversal loading that evidences the transition from predominant regimes of tension to compression, i. e., the so-called unilateral behavior of the damaged concrete. However, the model is not capable to simulate the influence of the previous damage processes in compression (diffuse damage) when there is the transition from predominant regimes of compression to tension Comi [7]. From a micromechanics point of view this characteristic is due to the partial closure of micro-cracks loaded in compression which affect less the elasticity moduli in compression than in tension, Desmorat [8]. Therefore, to avoid this problem a new elasticity tensor is proposed and some numerical analyses are performed to simulate practical problems in structural engineering.

Many different strategies are possible and have been proposed in the literature to model the stiffness recovery as described in Comi [7], Carol and Willam [9], Welemane and Comery [10], Bielski et al. [11], Liu [12] and Araújo and Proença [13]. For more details, in Bielski [11] is presented a summary of some formulations of models that take into account the unilateral effect of the damage process, such as: the use of fourth-rank projection operators for the decomposition of the stress and strain tensors into the positive and negative projections, besides the use of the generalized projection operators.

On the other hand, despite the progresses in the macroscopic modeling of the unilateral effect (in particular, the continuity problems that arise when the induced anisotropy is simultaneously described), this subject still remains as an open research field when it deals with induced anisotropy damage models, even when the micromechanical theory has been used to justify the proposal of constitutive models dealing with cracked media, Welemane and Comery [10], Zhu [14], Zhu [15] and Pichler and Dormieux [16]. This can be noted even when dealing with more actual approaches based on multi-scale analysis procedures, Skarzynski and Tejchman [17] and Pituba and Souza Neto [18]. Indeed, this work intends to contribute to the modeling of damage unilateral effect applied to concrete structures. However, it must be noted that the proposed model is not capable to take into account the friction effects, namely blocking and dissipative sliding of closed microcrack lips. This feature can be discussed in future works.

2. Bi-dissipative plastic-damage model

2.1 Original proposal of Pituba and Fernandes [4]

The original damage model formulation Pituba and Fernandes [4] is built from the formalism presented in Pituba [2]. Moreover, the model respects the principle of energy equivalence between damaged real medium and equivalent continuous medium established in the CDM. The damage model is briefly presented in this work. Initially, for dominant tension states, a damage tensor is proposed:

$$\boldsymbol{D_T} = f_1(D_1,D_4,D_5)\,(\boldsymbol{A}\otimes\boldsymbol{A}) + 2f_2(D_4,D_5)\,[(\boldsymbol{A}\underline{\otimes}\boldsymbol{I} + \boldsymbol{I}\underline{\otimes}\boldsymbol{A}) - (\boldsymbol{A}\otimes\boldsymbol{A})] \quad (1)$$

where $f_1(D_1, D_4, D_5) = D_1 - 2\,f_2(D_4, D_5)$ and $f_2(D_4, D_5) = 1 - (1\text{-}D_4)(1\text{-}D_5)$. The variable D_1 represents the damage in direction orthogonal to the transverse isotropy local plane of the material, while D_4 is representative of the damage due to the sliding movement between the crack faces. The third damage variable, D_5, is only activated if a previous compression state accompanied by damage has occurred. In Curnier [1], the tensor **I** is the second-order identity tensor and the tensor **A**, is formed by dyadic product of the unit vector perpendicular to the transverse isotropy plane for himself. Those products are given in Pituba [2]. For dominant compression states, it is proposed the other damage tensor:

$$\boldsymbol{D_C} = f_1^*(D_2,D_4,D_5)\,(\boldsymbol{A}\otimes\boldsymbol{A}) + f_2(D_3)\,[(\boldsymbol{I}\underline{\otimes}\boldsymbol{I}) - (\boldsymbol{A}\otimes\boldsymbol{A})] + 2f_3(D_4,D_5)\,[(\boldsymbol{A}\underline{\otimes}\boldsymbol{I} + \boldsymbol{I}\underline{\otimes}\boldsymbol{A}) - (\boldsymbol{A}\otimes\boldsymbol{A})] \quad (2)$$

where $f_1^*(D_2, D_4, D_5) = D_2 - 2f_3(D_4, D_5)$, $f_2(D_3) = D_3$ and $f_3(D_4,D_5) = 1 - (1\text{-}D_4)(1\text{-}D_5)$. Note that the compression damage tensor introduces two additional scalar variables in its composition: D_2 and D_3. The variable D_2 (damage perpendicular to the transverse isotropy local plane) reduces the Young's modulus in that direction and in conjunction to D_3 (that represents the damage in the transverse isotropy plane) degrades the Poisson's ratio throughout the perpendicular planes to the one of transverse isotropy.

On the other hand, the constitutive tensor is written as:

$$\mathbf{E}(\varepsilon) := \begin{cases} E_{-}(\varepsilon) \ if \ \ g(\varepsilon, D_T, D_C) < 0, \\ E_{+}(\varepsilon) \ if \ \ g(\varepsilon, D_T, D_C) > 0, \end{cases} \tag{3}$$

$$\boldsymbol{E}_{+}(\varepsilon) = \lambda_{II}[I \otimes I] + 2\mu_1[\bar{I} \bar{\otimes} I] - \lambda_{22}^{+}(D_1, D_4, D_5)\,[A \otimes A] - \lambda_{12}^{+}(D_1)\,[\mathbf{A}\otimes\mathbf{I}+\mathbf{I}\otimes\mathbf{A}] - \mu_2(D_4, D_5)\,[\boldsymbol{A}\bar{\otimes}\boldsymbol{I} + \boldsymbol{I}\bar{\otimes}\boldsymbol{A}] \tag{4}$$

$$\boldsymbol{E}_{-}(\varepsilon) = \lambda_{II}[\boldsymbol{I} \otimes \boldsymbol{I}] + 2\mu_1[\boldsymbol{I} \bar{\otimes} \boldsymbol{I}] - \lambda_{22}^{-}(D_2, D_3, D_4, D_5)\,[A \otimes A] - \lambda_{12}^{-}(D_2, D_3)\,[\mathbf{A}\otimes\mathbf{I}+\mathbf{I}\otimes\mathbf{A}] - \lambda_{II}^{-}(D_3)\,[\mathbf{I}\otimes\mathbf{I}] - \frac{(1-2\nu_0)}{\nu_0}\lambda_{II}^{-}(D_3)\,[\mathbf{I}\bar{\otimes}\mathbf{I}] - \mu_2(D_4, D_5)\,[\boldsymbol{A}\bar{\otimes}\boldsymbol{I} + \boldsymbol{I}\bar{\otimes}\boldsymbol{A}] \tag{5}$$

The remaining parameters will only exist for no-null damage, evidencing the anisotropy and bimodularity induced by damage. Those parameters are given by:

$$\lambda_{22}^{+}(D_1,D_4,D_5) = (\lambda_0 + 2\mu_0)(2D_1 - D_1^2) - 2\lambda_{12}^{+}(D_1) - 2\mu_2(D_4,D_5)$$
$$\lambda_{12}^{+}(D_1) = \lambda_0 D_1; \quad \mu_2(D_4,D_5) = 2\mu_0[1-(1-D_4)^2(1-D_5)^2]$$
$$\lambda_{22}^{-}(D_2,D_3,D_4,D_5) = (\lambda_0 + 2\mu_0)(2D_2 - D_2^2) - 2\lambda_{12}^{-}(D_2,D_3) + \frac{(\nu_0 - 1)}{\nu_0}\lambda_{II}^{-}(D_3) - 2\mu_2(D_4,D_5)$$
$$\lambda_{12}^{-}(D_2,D_3) = \lambda_0[(1-D_3)^2 - (1-D_2)(1-D_3)]; \ \lambda_{II}^{-}(D_3) = \lambda_0(2D_3 - D_3^2) \tag{6}$$

As it can see, the constitutive model includes two damage tensors in order to take into account the bimodularity induced by damage in the concrete behavior. Therefore, it is necessary a criterion to define the tension and compression dominant states to indicate what damage tensor should be used.

The criterion has been extended in Pituba [2] in order to the actual damage state can influence on the hyperplane definition. Therefore, the following relationship has been proposed:

$$g(\varepsilon, \boldsymbol{D_T}, \boldsymbol{D_C}) = \boldsymbol{N}(\boldsymbol{D_T}, \boldsymbol{D_C}) \cdot \varepsilon_e \tag{7}$$

In Pituba and Fernandes [4], a particular form is adopted for the hypersurface in the strain space: a hyperplane g(ε) defined by the unit normal **N** (||**N**|| = 1) and characterized by its dependence of the strain and damage states. Accordingly with Eq. (7) and referring to general cases of loading, the following relationship has been proposed for the hyperplane:

$$g(\varepsilon, \boldsymbol{D_T}, \boldsymbol{D_C}) = \boldsymbol{N}(\boldsymbol{D_T}, \boldsymbol{D_C}) \cdot \varepsilon_e = \gamma_1(D_1, D_2)\ \varepsilon_V^e + \gamma_2(D_1, D_2)\ \varepsilon_{II}^e \tag{8}$$

where $\gamma_1(D_1,D_2) = \{1+H(D_2)[H(D_1)-1]\}\eta(D_1)+\{1+H(D_1)[H(D_2)-1]\}\eta(D_2)$ and $\gamma_2(D_1,D_2) = D_1+D_2$.

The Heaveside functions employed above are given by:

$$H(Di) = 1 \ \text{ to } \ Di > 0; H(Di) = 0 \ \text{ to } \ Di = 0 \quad (i = 1, 2) \tag{9}$$

The $\eta(D_1)$ and $\eta(D_2)$ functions are defined, respectively, for the tension and compression cases, assuming for the first one that there was no previous damage in compression affecting the present tension damage variable D_1 and analogously, for the second one that has not had previous tension damage affecting variable D_2. The proposed functions are:

$$\eta(D_1) = \frac{-D_1 + \sqrt{3 - 2D_1^2}}{3} \tag{10}$$

$$\eta(D_2) = \frac{-D_2 + \sqrt{3 - 2D_2^2}}{3} \tag{11}$$

Note that if the damage process in the material is not activated ($D_1 = D_2 = 0$) the Eq. (8) recovers the equation proposed by Comi [7], thus the formulation satisfies the proposed condition of initially isotropic material. Already, if the material is totally damaged, $D_1 = D_2 = 1$ ($\eta(D_1) = \eta(D_2) = 0$) and $\gamma_2 = 2$, the hyperplane g(ε) is coincident to the transverse isotropy local plane of the material and, therefore, the normal vector to the hyperplane is given by the transverse isotropy tensor **A**.

On the other hand, due to anisotropy induced by damage, it is convenient to separate the damage criterion into two criteria: the first one is only used to indicate the beginning of the damage processes, or that the material is no longer isotropic; the second one is used for loading and unloading processes, when the material is already considered as transverse isotropic medium. This second criterion identifies if there is or not evolution of the damage variables. That division is justified by the difference between the complementary elastic strain energies of isotropic and transverse isotropic materials. If there is damage evolution, i. e., when $\dot{\mathbf{D}}_\mathbf{T} \neq \mathbf{0}$ or $\dot{\mathbf{D}}_\mathbf{C} \neq \mathbf{0}$, the evolution laws of the damage variables are written as associated variables functions. Considering just the case of monotonic loading, the evolution laws proposed for the scalar damage variables are resulting of fittings on experimental results. The general form proposed is:

$$D_i = 1 - \frac{1 + A_i}{A_i + exp[B_i(Y_i - Y_{0i})]} \quad i = 1, 5 \tag{12}$$

where A_i, B_i and Y_{0i} are parameters of the model that must be identified through the uniaxial tension and compression tests and biaxial compression tests.

When the damage process is activated, the formulation starts to involve the tensor **A** that depends on the normal to the transverse isotropy plane. Therefore, it is necessary to establish some rules to identify its location for an actual strain state. Initially, it is established a general criterion for the existence of the transverse isotropy plane. In Pituba and Fernandes [4] is proposed that the transverse isotropy due to damage only arises if positive strain rates exist at least in one of the principal directions. After assuming such proposition as valid, some rules to identify its location are defined.

2.2 Discussion about the unilateral effect in brittle materials

The original version of the damage model is bimodular, however it is necessary to take into account the diffuse damage generated in previous compression regimes when dealing with tension regimes. This problem can be solved by introduction of a new elasticity tensor in tension dominant states. Therefore, respecting the principle of energy equivalence, for the uniaxial point of view, for instance, the constitutive tensor is written as:

$$\boldsymbol{E}_T = \boldsymbol{E}_0\,(1-D_1)^2(1-D_2)^2 \tag{13}$$

The relationship above shows that in tension dominant states prevailing prior to activation of damage in compression is possible to solve the problem discussed here. By analogy, under multiaxial stress states, it can be concluded that damage tensor in compression $\mathbf{D}_c$ should compose the expression of the constitutive tensor in tension dominant states. Therefore, respecting the principle of equivalence of energy, the constitutive tensor is now written as:

$$\mathbf{E}_T = (\mathbf{I}-\mathbf{D}_C)(\mathbf{I}-\mathbf{D}_T)\mathbf{E}_0(\mathbf{I}-\mathbf{D}_T)(\mathbf{I}-\mathbf{D}_C) \tag{14}$$

Considering a matrix representation and assuming, for instance, that the transversal isotropy local plane is coincident to the 2–3 plane, the constitutive tensor $\mathbf{E}_T$ may be described as follows:

$$\boldsymbol{E}_T = \begin{bmatrix} (\lambda_0+2\mu_0)(1-\boldsymbol{D}_1)^2(1-\boldsymbol{D}_2)^2 & \lambda_0(1-\boldsymbol{D}_1)(1-\boldsymbol{D}_2)(1-\boldsymbol{D}_3) & \lambda_0(1-\boldsymbol{D}_1)(1-\boldsymbol{D}_2)(1-\boldsymbol{D}_3) & 0 & 0 & 0 \\ \lambda_0(1-\boldsymbol{D}_1)(1-\boldsymbol{D}_2)(1-\boldsymbol{D}_3) & (\lambda_0+2\mu_0)(1-\boldsymbol{D}_3)^2 & \lambda_0(1-\boldsymbol{D}_3)^2 & 0 & 0 & 0 \\ \lambda_0(1-\boldsymbol{D}_1)(1-\boldsymbol{D}_2)(1-\boldsymbol{D}_3) & \lambda_0(1-\boldsymbol{D}_3)^2 & ((\lambda_0+2\mu_0)(1-\boldsymbol{D}_3)^2 & 0 & 0 & 0 \\ 0 & 0 & 0 & 2\mu_0 & 0 & 0 \\ 0 & 0 & 0 & 0 & 2\mu_0(1-\boldsymbol{D}_4)^4(1-\boldsymbol{D}_5)^4 & 0 \\ 0 & 0 & 0 & 0 & 0 & 2\mu_0(1-\boldsymbol{D}_4)^4(1-\boldsymbol{D}_5)^4 \end{bmatrix} \tag{15}$$

It can be noted that the equations (5) and (11) present different values for the shear moduli in compression and tension dominant states, respectively. Therefore, this alternative formulation in order to take into account the diffuse damage does not respect the Curnier´s condition about the tangential continuity. To avoid this problem, another expression for the damage tensor in compression dominant states $\mathbf{D}_C^*$ is proposed. This tensor is given by:

$$\boldsymbol{D}_C^* = f_1(D_2,)\,(\boldsymbol{A}\otimes\boldsymbol{A}) + f_2(D_3)\,[(\boldsymbol{I}\bar{\otimes}\boldsymbol{I}) - (\boldsymbol{A}\otimes\boldsymbol{A})] \tag{16}$$

where $f_1(D_2) = D_2$ and $f_2(D_3) = D_3$. It is important to observe that the damage tensor $\mathbf{D}_C^*$ provides the diffuse damage in previous compression states through the changing of the volumetric modulus, as proposed in Comi [7]. For simplicity, considering a matrix representation and assuming, for instance, that the transversal isotropy local plane is coincident to the 2–3 plane, equation (16) is written as:

$$\boldsymbol{D}_C^* = \begin{bmatrix} \boldsymbol{D}_2 & 0 & 0 & 0 & 0 & 0 \\ 0 & \boldsymbol{D}_3 & 0 & 0 & 0 & 0 \\ 0 & 0 & \boldsymbol{D}_3 & 0 & 0 & 0 \\ 0 & 0 & 0 & 0 & 0 & 0 \\ 0 & 0 & 0 & 0 & 0 & 0 \\ 0 & 0 & 0 & 0 & 0 & 0 \end{bmatrix} \tag{17}$$

Finally, taking into account the principle of energy equivalence, the constitutive tensor for tension dominant states is given by:

$$\mathbf{E}_T = (\mathbf{I}-\mathbf{D}_C^*)(\mathbf{I}-\mathbf{D}_T)\mathbf{E}_0(\mathbf{I}-\mathbf{D}_T)(\mathbf{I}-\mathbf{D}_C^*) \tag{18}$$

$$\boldsymbol{E_T}=\begin{bmatrix}(\lambda_0+2\mu_0)(1-\boldsymbol{D_1})^2(1-\boldsymbol{D_2})^2 & \lambda_0(1-\boldsymbol{D_1})(1-\boldsymbol{D_2})(1-\boldsymbol{D_3}) & \lambda_0(1-\boldsymbol{D_1})(1-\boldsymbol{D_2})(1-\boldsymbol{D_3}) & 0 & 0 & 0\\ \lambda_0(1-\boldsymbol{D_1})(1-\boldsymbol{D_2})(1-\boldsymbol{D_3}) & (\lambda_0+2\mu_0)(1-\boldsymbol{D_3})^2 & \lambda_0(1-\boldsymbol{D_3})^2 & 0 & 0 & 0\\ \lambda_0(1-\boldsymbol{D_1})(1-\boldsymbol{D_2})(1-\boldsymbol{D_3}) & \lambda_0(1-\boldsymbol{D_3})^2 & ((\lambda_0+2\mu_0)(1-\boldsymbol{D_3})^2 & 0 & 0 & 0\\ 0 & 0 & 0 & 2\mu_0 & 0 & 0\\ 0 & 0 & 0 & 0 & 2\mu_0(1-\boldsymbol{D_4})^2(1-\boldsymbol{D_5})^2 & 0\\ 0 & 0 & 0 & 0 & 0 & 2\mu_0(1-\boldsymbol{D_4})^2(1-\boldsymbol{D_5})^2\end{bmatrix} \quad (19)$$

Then, following the formalism presented in Pituba [2], the bidissipative anisotropy damage model taking into account the unilateral effect in brittle materials is written as:

$$W(\varepsilon)=\rho\psi(\varepsilon):=\begin{cases}W_-(\varepsilon)\ if\ \ \boldsymbol{g}(\varepsilon,\boldsymbol{D_T},\boldsymbol{D_C})<0,\\ W_+(\varepsilon)\ if\ \ \boldsymbol{g}(\varepsilon,\boldsymbol{D_T},\boldsymbol{D_C})>0,\end{cases} \quad (20)$$

$$W_+=\rho\psi_+(\varepsilon)=\frac{\lambda_{11}}{2}tr^2(\varepsilon)+\mu_1 tr(\varepsilon^2)-\frac{\lambda^+_{22}(D_1,D_2,D_3,D_4,D_5)}{2}\mathrm{tr}^2(\mathbf{A}\varepsilon)-\lambda^+_{12}(D_1,D_2,D_3)tr(\varepsilon)tr(\mathbf{A}\varepsilon)$$
$$-\frac{\lambda^-_{11}(D_3)}{2}tr^2(\varepsilon)-\frac{(1-2\nu_0)}{2\nu_0}\lambda^-_{11}(D_3)tr[(\boldsymbol{I}\overline{\otimes}\boldsymbol{I})\varepsilon]^2-\mu_2(D_4,D_5)\,tr(\boldsymbol{A}\varepsilon^2) \quad (21)$$

$$W_-=\rho\psi_-(\varepsilon)=\frac{\lambda_{11}}{2}tr^2(\varepsilon)+\mu_1 tr(\varepsilon^2)-\frac{\lambda^-_{22}(D_2,D_3,D_4,D_5)}{2}\mathrm{tr}^2(\mathbf{A}\varepsilon)-\lambda^-_{12}(D_2,D_3)tr(\varepsilon)tr(\mathbf{A}\varepsilon)$$
$$-\frac{\lambda^-_{11}(D_3)}{2}tr^2(\varepsilon)-\frac{(1-2\nu_0)}{2\nu_0}\lambda^-_{11}(D_3)tr[(\boldsymbol{I}\overline{\otimes}\boldsymbol{I})\varepsilon]^2-\mu_2(D_4,D_5)\,tr(\boldsymbol{A}\varepsilon^2) \quad (22)$$

Now, the parameters λ_{ij} and μ_i are given by:

$$\lambda^+_{22}(D_1,D_2,D_3,D_4,D_5)=(\lambda_0+2\mu_0)(2D_1-D_1^2)$$
$$-2\lambda^+_{12}(D_1,D_2,D_3)-2\mu_2(D_4,D_5)+\frac{(\nu_0-1)}{\nu_0}\lambda^-_{11}(D_3)+(\lambda_0+2\mu_0)\left[(1-D_1)^2-(1-D_1)^2(1-D_2)^2\right]$$
$$\lambda^+_{12}(D_1,D_2,D_3)=\lambda_0\left[(1-D_3)^2-(1-D_1)(1-D_2)(1-D_3)\right]$$
$$\mu_2(D_4,D_5)=2\mu_0[1-(1-D_4)^2(1-D_5)^2]$$
$$\lambda^-_{22}(D_2,D_3,D_4,D_5)=(\lambda_0+2\mu_0)(2D_2-D_2^2)-2\lambda^-_{12}(D_2,D_3)$$
$$+\frac{(\nu_0-1)}{\nu_0}\lambda^-_{11}(D_3)-2\mu_2(D_4,D_5)$$
$$\lambda^-_{12}(D_2,D_3)=\lambda_0[(1-D_3)^2-(1-D_2)(1-D_3)]$$
$$\lambda^-_{11}(D_3)=\lambda_0(2D_3-D_3^2) \quad (23)$$

The stress tensor is obtained from the gradient of the elastic potential, as follows:

$$\sigma(\varepsilon)=\begin{cases}\sigma_{-}(\varepsilon)=\nabla_{\varepsilon}\rho\psi_{-}(\varepsilon) \;\; if \;\; g(\varepsilon,\boldsymbol{D_T},\boldsymbol{D_C})<0,\\ \sigma_{+}(\varepsilon)=\nabla_{\varepsilon}\rho\psi_{+}(\varepsilon) \;\; if \;\; g(\varepsilon,\boldsymbol{D_T},\boldsymbol{D_C})>0,\end{cases} \tag{24}$$

$$\sigma_{+}(\varepsilon)=\lambda_{11}tr(\varepsilon)\mathbf{I}+2\mu_1\varepsilon-\lambda_{22}^{+}(D_1,D_2,D_3,D_4,D_5)\,\mathrm{tr}(\mathbf{A}\varepsilon)\mathbf{A}-\lambda_{12}^{+}(D_1,D_2,D_3)(\mathrm{tr}(\varepsilon)\mathbf{A}+\mathrm{tr}(\mathbf{A}\varepsilon)\mathbf{I})-\lambda_{11}^{-}(D_3)\,tr(\varepsilon)\boldsymbol{I}-\frac{(1-2\nu_0)}{\nu_0}\lambda_{11}^{-}(D_3)(\boldsymbol{I}\overline{\otimes}\boldsymbol{I})\varepsilon-\mu_2(D_4,D_5)(\boldsymbol{A}\varepsilon+\varepsilon\boldsymbol{A}) \tag{25}$$

$$\sigma_{-}(\varepsilon)=\lambda_{11}tr(\varepsilon)\mathbf{I}+2\mu_1\varepsilon-\lambda_{22}^{-}(D_2,D_3,D_4,D_5)\,\mathrm{tr}(\mathbf{A}\varepsilon)\mathbf{A}-\lambda_{12}^{-}(D_2,D_3)(\mathrm{tr}(\varepsilon)\mathbf{A}+\mathrm{tr}(\mathbf{A}\varepsilon)\mathbf{I})-\lambda_{11}^{-}(D_3)\,tr(\varepsilon)\boldsymbol{I}-\frac{(1-2\nu_0)}{\nu_0}\lambda_{11}^{-}(D_3)(\boldsymbol{I}\overline{\otimes}\boldsymbol{I})\varepsilon-\mu_2(D_4,D_5)(\boldsymbol{A}\varepsilon+\varepsilon\boldsymbol{A}) \tag{26}$$

The constitutive tensor is also obtained from the elastic potential, i. e.:

$$\mathbf{E}(\varepsilon):=\begin{cases}\boldsymbol{E}_{-}(\varepsilon)=\nabla_{\varepsilon}^{2}\rho\psi_{-}(\varepsilon) \;\; if \;\; g(\varepsilon,\boldsymbol{D_T},\boldsymbol{D_C})<0,\\ \boldsymbol{E}_{+}(\varepsilon)=\nabla_{\varepsilon}^{2}\rho\psi_{+}(\varepsilon) \;\; if \;\; g(\varepsilon,\boldsymbol{D_T},\boldsymbol{D_C})>0,\end{cases} \tag{27}$$

$$\boldsymbol{E}_{+}(\varepsilon)=\boldsymbol{E_T}=\lambda_{11}[\boldsymbol{I}\otimes\boldsymbol{I}]+2\mu_1[\boldsymbol{I}\underline{\overline{\otimes}}\boldsymbol{I}]-\lambda_{22}^{+}(D_1,D_2,D_3,D_4,D_5)[\boldsymbol{A}\otimes\boldsymbol{A}]-\lambda_{12}^{+}(D_1,D_2,D_3)[\mathbf{A}\otimes\mathbf{I}+\mathbf{I}\otimes\mathbf{A}]-\lambda_{11}^{-}(D_3)[\mathbf{I}\otimes\mathbf{I}]-\frac{(1-2\nu_0)}{\nu_0}\lambda_{11}^{-}(D_3)[\mathbf{I}\overline{\otimes}\mathbf{I}]-\mu_2(D_4,D_5)[\boldsymbol{A}\underline{\overline{\otimes}}\boldsymbol{I}+\boldsymbol{I}\underline{\overline{\otimes}}\boldsymbol{A}] \tag{28}$$

$$\boldsymbol{E}_{-}(\varepsilon)=\boldsymbol{E_C}=\lambda_{11}[\boldsymbol{I}\otimes\boldsymbol{I}]+2\mu_1[\boldsymbol{I}\underline{\overline{\otimes}}\boldsymbol{I}]-\lambda_{22}^{-}(D_2,D_3,D_4,D_5)[\boldsymbol{A}\otimes\boldsymbol{A}]-\lambda_{12}^{-}(D_2,D_3)[\mathbf{A}\otimes\mathbf{I}+\mathbf{I}\otimes\mathbf{A}]-\lambda_{11}^{-}(D_3)[\mathbf{I}\otimes\mathbf{I}]-\frac{(1-2\nu_0)}{\nu_0}\lambda_{11}^{-}(D_3)[\mathbf{I}\overline{\otimes}\mathbf{I}]-\mu_2(D_4,D_5)[\boldsymbol{A}\underline{\overline{\otimes}}\boldsymbol{I}+\boldsymbol{I}\underline{\overline{\otimes}}\boldsymbol{A}] \tag{29}$$

Taking into account the unilateral effect and assuming that direction 1 be perpendicular to the transverse isotropy local plane in the strain space, the complementary elastic energy of the damaged medium in tension dominant states is now expressed by:

$$W_{e+}^{*}=\frac{\sigma_{11}^{2}}{2E_0(1-D_1)^2(1-D_2)^2}+\frac{(\sigma_{22}^{2}+\sigma_{33}^{2})}{2E_0(1-D_3)^2}-\frac{\nu_0(\sigma_{11}\sigma_{22}+\sigma_{11}\sigma_{33})}{E_0(1-D_1)(1-D_2)(1-D_3)}-\frac{\nu_0\sigma_{22}\sigma_{33}}{E_0(1-D_3)^2}+\frac{(1+\nu_0)}{E_0(1-D_4)^2(1-D_5)^2}(\sigma_{12}^{2}+\sigma_{13}^{2})+\frac{(1+\nu_0)}{E_0}\sigma_{23}^{2} \tag{30}$$

The variables associated to damage variables in tension with damage activated in previous compression will also be modified, because they are obtained from the elastic potential (20). Therefore, the following relationships are valid:

$$Y_T = \frac{\partial W^*_{e+}}{\partial D_1} + \frac{\partial W^*_{e+}}{\partial D_4} = Y_1 + Y_4 \quad (31)$$

$$Y_1 = \frac{\sigma^2_{11}}{E_0(1-D_1)^3(1-D_2)^2} - \frac{\nu_0(\sigma_{11}\sigma_{22}+\sigma_{11}\sigma_{33})}{E_0(1-D_1)^2(1-D_2)(1-D_3)} \quad (32)$$

$$Y_4 = \frac{(1+\nu_0)}{E_0(1-D_4)^3(1-D_5)^2}(2\sigma^2_{12} + 2\sigma^2_{13}) \quad (33)$$

Note that only Y_1 must to take into account the diffuse damage represented by D_2 and D_3. In this case, those damage variables are constants because there is no energy release rates during the damage evolution in tension dominant states related to D_2 and D_3. In the case of tension dominant states without activation of damage processes in previous compression, the original version of the damage model is recovered.

It can be verified that the unilateral damage model satisfies two basic requirements of this modeling kind:

Figure 1 – Finite layered element

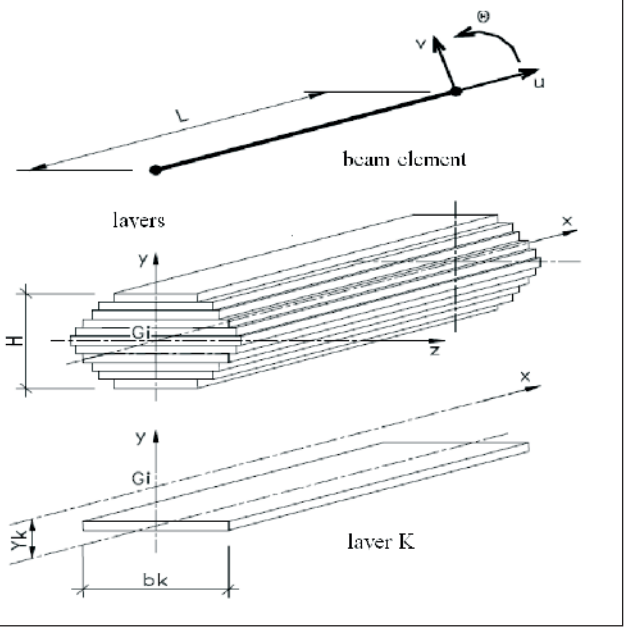

The model does not produce spurious energy dissipation upon closed load paths which do not activate damage, Matallah and La Borderie [19].

The continuity of the stress-strain law across the tension-compression interface is assured (hiperplano $g(\varepsilon,\mathbf{D}_T,\mathbf{D}_C)$), because the damage model is derived from the formulation proposed in Pituba [2], following the requirements of Curnier [1] and Welemane and Comery [10]. The continuity of the stress-strain law between two damage states imposes that the elastic potential must be once continuously differentiable (whole wise), but only piecewise twice continuously differentiable.

Accordingly with Curnier [1], other problem related to this kind of modeling concerns the loss of isotropy of the elasticity tensor in the transition through the tension-compression interface. The isotropy is preserved only if the interface is defined in the same group of symmetry of the elasticity tensor. In the proposed model the hyperplane and elasticity tensor belong to the group of isotropic material if there is not damage process. On the other hand, if there is activation of damage processes, the hyperplane starts to present the symmetry of the transverse isotropic material as well as the elasticity tensor. Anyway, the model always preserves the isotropy of the elasticity tensor.

2.3 Damage model applied in framed RC structures

This work intends to show the capabilities of the modified damage model to simulate the mechanical behavior of reinforced concrete structures submitted to reversal loading in possible practical situations of structural engineering. So, it is necessary that the model presents efficient numerical responses, i. e., numerical analyses with low computational cost and a few parameters of the model to be identified. Therefore, the one-dimensional version of the damage model has been implemented in a finite element code for bar structures analysis with finite layered elements in order to model the reinforced concrete framed structures. For the longitudinal reinforcement bars, standard elastoplastic behavior is admitted. In the transversal section, a certain layer can contain steel and concrete, see Fig. 01. A perfect adherence between materials is adopted and an equivalent elasticity modulus and inelastic strain are defined for each layer by using homogenization rule:

$$E_k = (1 - C_{sk})E_{ck} + C_{sk}E_{sk} \quad (34)$$

$$\varepsilon_{ink} = (1 - C_{sk})\varepsilon_{cink} + C_{sk}\varepsilon_{psk} \quad (35)$$

where,

– C_{sk} is the volumetric rate of steel in the layer N° k
– E_{sk} is the elasticity modulus of steel in the layer N° k
– E_{ck} is the elasticity modulus of concrete in the layer N° k
– ε_{psk} is the plastic strain of steel in the layer N° k
– ε_{ink} is the homogenized inelastic strain in the layer N° k
– ε_{cink} is the inelastic strain of concrete in the layer N° k
– E_k is the homogenized elasticity modulus in the layer N° k

Considering the direction 1 as the longitudinal direction of the finite element, the formulation presented in the previous item is simplified and presented as follows:

$$\boldsymbol{E}(\varepsilon) := \begin{cases} \mathbf{E}_{-}(\varepsilon) = \nabla^2_{\varepsilon}\rho\psi_{-}(\varepsilon) & \text{if} \quad g(\varepsilon, \mathbf{D}_T, \mathbf{D}_C) < 0, \\ \mathbf{E}_{+}(\varepsilon) = \nabla^2_{\varepsilon}\rho\psi_{+}(\varepsilon) & \text{if} \quad g(\varepsilon, \mathbf{D}_T, \mathbf{D}_C) > 0, \end{cases} \tag{36}$$

$$E_T = E_0(1-D_1)^2(1-D_2)^2 \tag{37}$$

$$E_C = E_0(1-D_2)^2 \tag{38}$$

$$W^*_{e+} = \frac{\sigma^2_{11}}{2E_0(1-D_1)^2(1-D_2)^2} \tag{39}$$

$$W^*_{e-} = \frac{\sigma^2_{11}}{2E_0(1-D_2)^2} \tag{40}$$

$$Y_T = \frac{\partial W^*_{e+}}{\partial D_1} = Y_1 \tag{41}$$

$$Y_C = \frac{\partial W^*_{e-}}{\partial D_2} = Y_2 \tag{42}$$

$$Y_1 = \frac{\sigma^2_{11}}{E_0(1-D_1)^3(1-D_2)^2} \tag{43}$$

$$Y_2 = \frac{\sigma^2_{11}}{E_0(1-D_2)^3} \tag{44}$$

The one-dimensional version of the model takes into account permanent strains induced by damage evolution. Assuming, for simplicity, that the permanent strains are composed exclusively by volumetric strains, as it has already been considered in Comi [7], and taking into account the unilateral effect, the evolution law results:

$$\dot{\varepsilon}^p = \left(\frac{\beta_1}{(1-D_1)^2}\dot{D}_1 + \frac{\beta_2}{(1-D_2)^2}\dot{D}_2 \right) \mathbf{I} \tag{45}$$

Observe that β_1 and β_2 are parameters directly related to the evolutions of permanent strains induced by damage in tension and in compression, respectively. The consideration of the permanent strains improves the capture of the transverse strains by the model, as it can see in Pituba and Fernandes [4]. Besides, the model predicts the change in sign of the volumetric strain.

3. Micromechanical theory

Although the damage model has been based on the macromechanical behavior of the concrete, this item intends to show the strong connection between the model and the micromechanical theory. The description of the damage activation-deactivation process as part of macroscopic modeling requires knowing when the transition between these two states of damage occur and how damage deactivation affect the elastic properties of the material, Welemane and Comery [10]. Moreover, there is a difficulty in recognizing tension and compression states in 3D micro-scale analysis in order to adopt a differentiable Gibbs potential. It is noted that the formulation for bimodular anisotropic damaged media proposed in Pituba [2] replies the first question (see Equation (7)). Besides, the continuity of the stress-strain law has been assured. In this context, this section aims to point out the influence of the opening-closure of microdefects on the elastic properties of the microcracked concrete.

Following Welemane and Comery [10], consider a RVE (representative volume element) of an homogeneous isotropic elastic linear matrix (Young modulus E_0 and Poisson rate v_0) weakened by an array of N randomly distributed flat penny-shaped microcracks (unit normal n_k, radius a_k), whose radii are very small in comparison with

Figure 2 – Parallel microcracks on concrete submitted to uniaxial tension stress

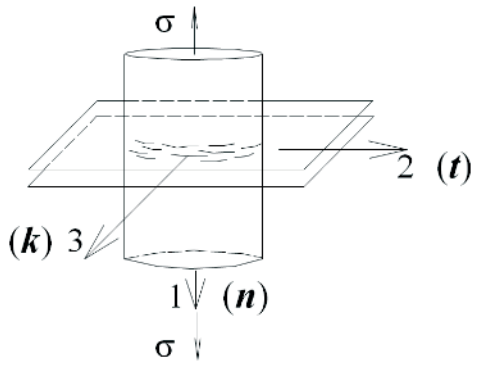

the size of the RVE. Assuming non-interaction among microcracks and sliding without friction of their lips, the free enthalpy of the microcracked medium is given by:

$$u=\frac{(1+\nu_0)}{2E_0}tr(\sigma\cdot\sigma)-\frac{\nu_0}{2E_0}(tr\sigma)^2+\frac{8}{3V}\frac{(1-\nu_0^2)}{(2-\nu_0)E_0}\sigma:\sum_{K=1}^{N}a_K^3\left[n_k^{\otimes 2}\underline{\otimes}I+I\underline{\otimes}n_k^{\otimes 2}-\left[2-(2-\nu_0)H(\sigma_n^k)\right]n_k^{\otimes 4}\right]:\sigma \quad (46)$$

The Heaviside function H depending on the normal stress to each microcrack is open ($\sigma_n^k \geq 0$) or closed ($\sigma_n^k < 0$).

Consider the simple case of a material weakened by a single array of parallel microcracks with unit normal n as in Fig. 2 and parameter $A = 16(1-\nu_0^2)/(6-3\nu_0)$. This case is interesting for the damage model proposed in this work because the effective medium exhibits the symmetry associated with the geometric shape of the microcracks with the privileged direction n (transverse isotropic material).

Then, the elastic moduli are fully determined by five independent coefficients E(**n**), E(**t**), ν(**n**,**t**), ν(**t**,**k**) and μ(**n**,**t**), for any vectors **t** and **k** forming with n an orthonormal basis of R^3. Using Eq (46), it can be obtained the elastic moduli mentioned above.

$$E(n)=E_0\left[1+\frac{A}{V}\sum_{K=1}^{N}a_k^3(2-\nu_0)H(\sigma_n^k)\right]^{-1} \quad (47)$$

$$\nu(n,t)=\nu_0\left[1+\frac{A}{V}\sum_{K=1}^{N}a_k^3(2-\nu_0)H(\sigma_n^k)\right]^{-1} \quad (48)$$

$$E(t)=E_0 \quad (49)$$

$$\nu(t,k)=\nu_0 \quad (50)$$

$$\mu(n,t)=\mu_0\left[1+\frac{A}{(1+\nu_0)V}\sum_{K=1}^{N}a_k^3\right]^{-1} \quad (51)$$

In Welemane and Comery [10] are described some conclusions about eqs (47)-(51) that are useful for a discussion about the proposed model. In general way, a macroscopic approach of the unilateral effect in brittle materials should no longer be considered only by the single restoration of the Young modulus in the direction normal to closed microcracks. Therefore, based on micromechanical observations, some important aspects related to unilateral effect of damage processes can be pointed out:

- The elastic moduli E(**n**) and Poisson ratio ν(**n**,**t**), related to normal direction to parallel microcracks, are affected by the evolution of the microdefects. In particular, those moduli recover their initial values (E_0 and ν_0) when the microcracks are closed.
- In the other hand, the shear modulus μ(**n**,**t**) remains the same when the microcracks are closed (partial deactivation of damage). This behavior is consistent with the hypothesis about tangential jump null of the constitutive tensor. However, the elastic moduli E(**m**), ν(**m**,**p**) and μ(**m**,**p**) related to directions with different orientations at principal axes (**n**,**t** and **k**) are partially recovered when the microcracks close.

The particular nature of the microdefects contribution allows extending these considerations for any of *N* microcracks with different normal vectors. In this context, let us compare the damaged elastic moduli given by the proposed model to those ones given by the micromechanical equations. Then, considering Fig. 2 and assuming, for instance, that the transversal isotropy local plane is coincident with the 2-3 plane, the elastic moduli given by the proposed model in dominant compression (subscript *C*) and in tension (subscript *T*) regimes are written as:

$$E_{T1}=E_0(1-D_1)^2(1-D_2)^2;\ E_{C1}=E_0(1-D_2)^2 \quad (52)$$

$$\nu_{T12}=\nu_{T13}=\nu_0\frac{(1-D_1)(1-D_2)}{(1-D_3)};\ \nu_{C12}=\nu_{C13}=\nu_0\frac{(1-D_2)}{(1-D_3)} \quad (53)$$

$$E_{T2}=E_{T3}=E_0(1-D_3)^2;\ E_{C2}=E_{C3}=E_0(1-D_3)^2 \quad (54)$$

$$\nu_{T23}=\nu_{C23}=\nu_0 \quad (55)$$

$$\mu_{T12}=\mu_{T13}=\mu_{C12}=\mu_{C13}=\mu_0(1-D_4)^2(1-D_5)^2 \quad (56)$$

The longitudinal elastic moduli in tension and in compression in the direction 1 depend on the dominant state, i. e., of the opening-closure criterion. This is also valid for the Poisson ratio in the 12 and 13 planes. On the other hand, the Poisson ratio in the

Figure 3 – Uniaxial test on concrete specimens submitted to reversal load

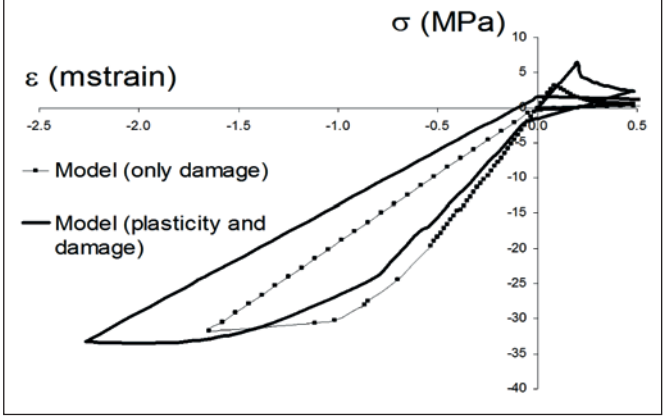

23 plane (transversal isotropy local plane) is not affected by the damage process. The shear moduli are not changed in the transition from the tension to compression regimes and vice-versa. Observe Eq. (54) and consider the transition from dominant tension regime (damage process in tension activated or not) to the compression regime without previous compression. In this case one has: $E_{T2} = E_{T3} = E_{C2} = E_{C3} = E_0$. This result is in correspondence with the form described by (49). Indeed, the $(1 - D_3)^2$ coefficient is necessary to take into account the diffuse damage in previous compression when the current dominant state is tension.

Obviously, in general cases, when the damage process is activated, the formulation starts to involve the tensor **A**, which depends on the knowledge of the normal to the transverse isotropy plane,

Figure 4 – Geometry, reinforcement details and loading history

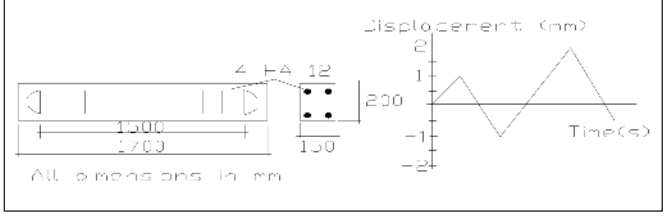

Pituba and Fernandes [4]. Therefore, the discussion about elastic moduli presented above is valid but that moduli are dependents of the tensor **A**, as described in item 2.1.

Finally, it is observed that despite the proposed model has macromechanical motivations in the macroscopic behaviour of the concrete, the model assists to the requirements suggested by Welemane and Comery [10] for the micromechanical analysis of the unilateral effect in materials.

4. Numerical applications

Initially, the unilateral model is used in the simulation of an uniaxial test in concrete specimens subject to reversal load in order to show the qualitative numerical response. Observe that the permanent strains are important in the definition of the hyperplane, in the sense that the total strains start to compose the criterion, Eq. (8). The initial stiffness recovery can be clearly observed taking into account permanent strain in the dominant tension regime. It is noted the contribution of the diffuse damage generated in previous compression regimes when dealing to tension regimes.

Figure 5 – Parametric identification in uniaxial compression test – La Borderie's RC Beam

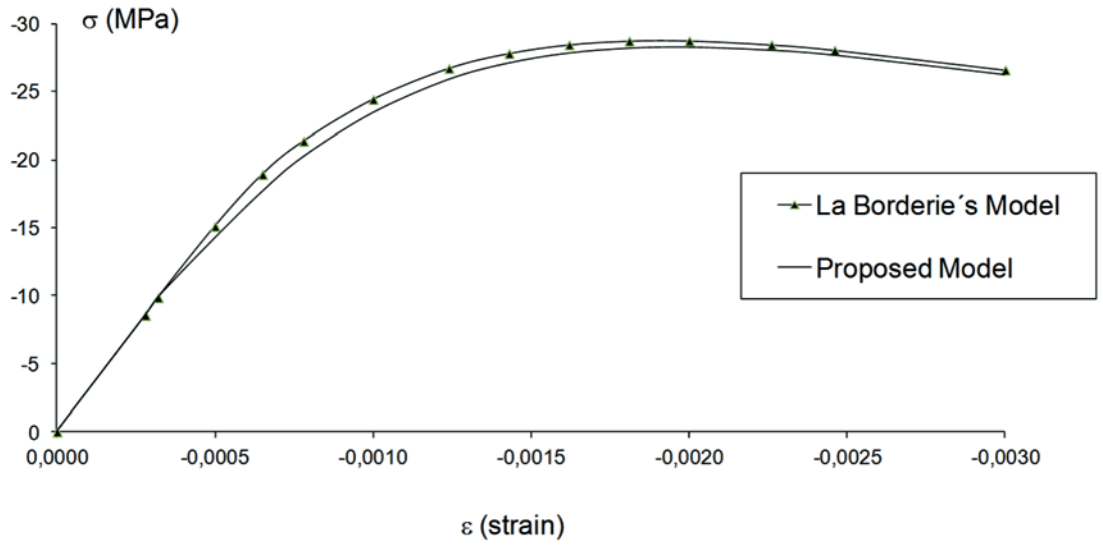

Figure 6 – Parametric identification in uniaxial tension test – La Borderie's RC Beam

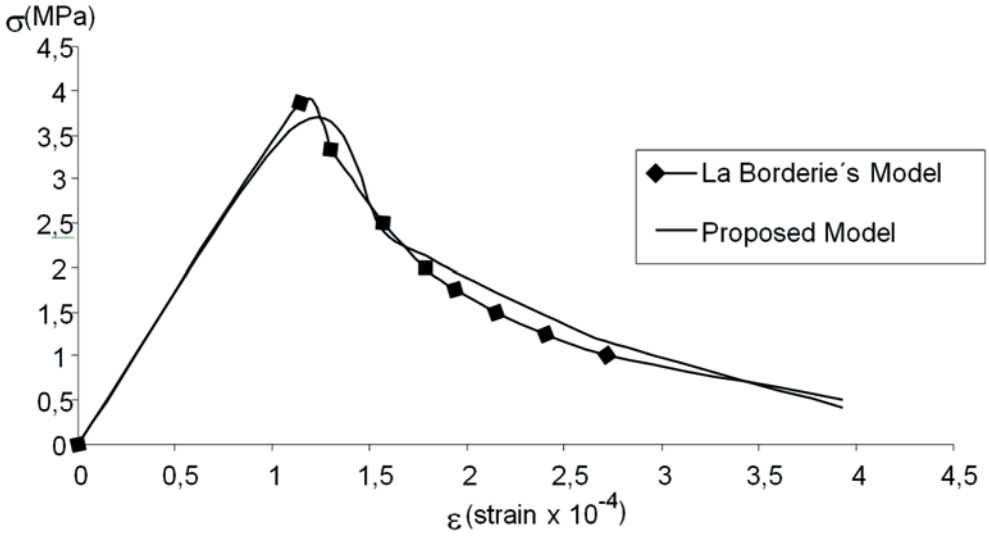

4.1 *Reinforced concrete beam with symmetric reinforcement*

This example deals with a test performed by La Borderie [20] and Matallah and La Borderie [19] that corresponds to a reinforced concrete beam in a configuration of three points cyclic flexion. The beam is subject to cyclic loading at the middle of the span. The concrete has elasticity modulus E_c = 31,800 MPa; the steel has E_s = 210,000 MPa, yielding stress of 445 MPa and ultimate stress of 540 MPa. In the experimental test, the beam is subjected to two loading cycles of amplitude, the first one is 1mm and the second one 2 mm (see Fig. 4). The beam geometry and its reinforcement distribution are illustrated in Fig. 4.

Figures 5 and 6 show the results of the parametric identification of the proposed damage model. The parameters used by La Borderie [20] were taken as reference in the simulation of uniaxial tension and compression tests. Table 1 presents the parameter values. It is important to note that the experimental tests do not present loading/unloading paths to identify β_1 and β_2. Therefore, the parameters β_1 and β_2 have been adopted in order to obtain the permanent strains evidenced by the numerical analysis of the concrete beam during the unloading process. This adoption has been made without interference in the value of the compression and tension strengths of the concrete.

In the numerical analysis, displacements increments have been enforced in the middle of the span. Using the advantage of symmetry, only half of the beam has been discretized into 20 finite elements. The transversal sections were divided into 16 layers where the reinforcement layers are located in the medium planes of the second and fifteenth layers. In Fig. 7 are shown the numerical and experimental responses of the vertical force and displacement in the middle of the span related to the first stage of the loading. It is noted the good precision of the numerical response.

In the other hand, in the Fig. 8 is illustrated the global response of whole test. The results obtained by the model are satisfactory despite the limited parametric identification of the parameters related to permanent strains. The ultimate experimental loads related to the first and second cycles are obtained by the both analyses: when only damage processes are considered and the other one when permanent strains (b_1 and b_2) are taken into account too. However, the permanent strains in the unloading processes are only captured by the modelling with permanent strains, as expected. In general way, the model reproduces satisfactorily the cyclic behaviour of the beam.

Besides, the damage profile is also close to experimental test observations, see Matallah and La Borderie [19]. In Fig. 09 is shown the damage distribution in tension regimes at two points of the curve illustrated in Fig. 08. The first point is located at the end of the first loading and the second one is located in the end of the second loading (reversal loading). These distributions have shown the opening/closure cracks process. The first damage in tension zone (D_1) occurs in the bottom of the beam. On the other hand, when the load is inverted, the damage in tension zone (D_1) appears in the upper zone of the beam, but the D_1 distribution in the bottom

Table1 – Parameters for the proposed damage model – La Borderie's RC Beam

Tension	Compression
Y_{01} = 6.0x10^{-5} MPa	Y_{02} = 3.0x10^{-3} MPa
A_1 = -0.93	A_2 = 1.50
B_1 = 110 MPa^{-1}	B_2 = 10.01 MPa^{-1}
β_1 = 8x10^{-5} MPa	β_2 = 1.0x10^{-3} MPa

Figure 7 – Experimental and numerical responses - first loading

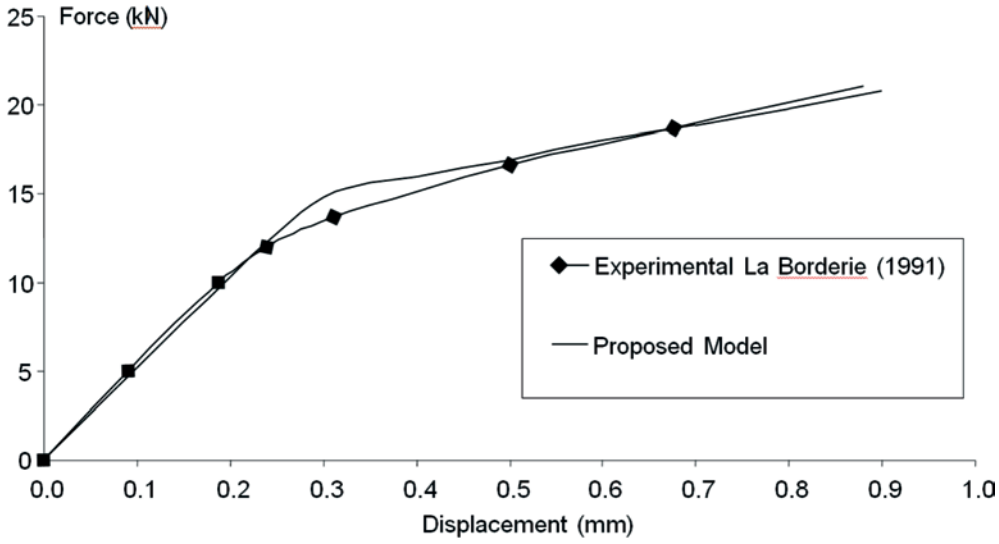

of the beam remains the same, although there is no increasing of values. Therefore, the cracks previously open are now closed. Note that the damage processes in the compression regimes (D_2) are not so important in this numerical application, according to observations in La Borderie [20]. It can be observed that the symmetric arrangement of the reinforcement leads to an additional support to compression stresses in the concrete.

4.2 Reinforced concrete frame

This experimental test was originally performed by Vecchio and Emara [21] taking into account just proportional loading/unloading, but without reversal loading. However, in this work, the reinforced concrete frame is submitted to loading/unloading and then a reversal loading is applied in order to show the potentialities of

Figure 8 – Global response of the reinforced concrete beam

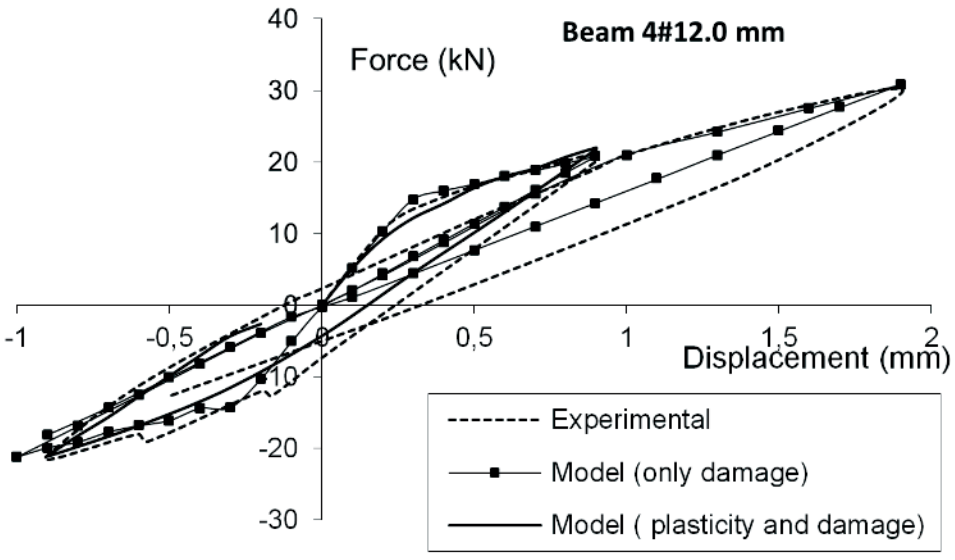

Figure 9 – Damage distribution in tension (D_1): a) End of first loading; b) End of second loading (reversal loading)

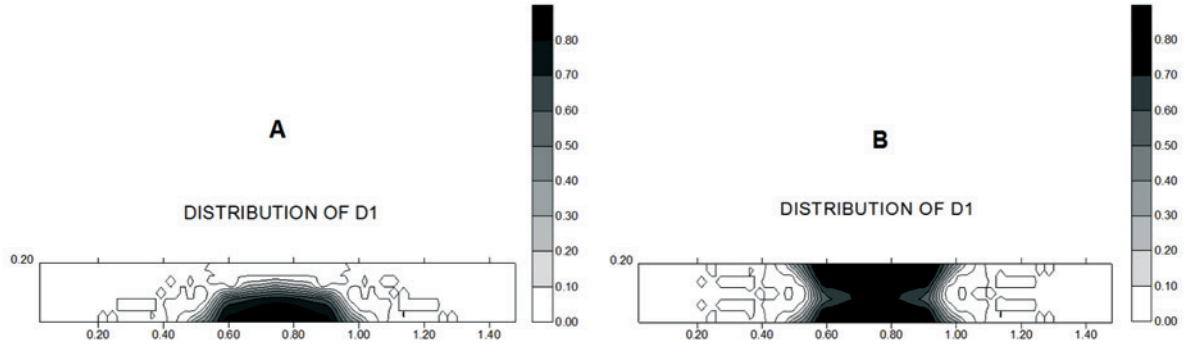

the proposed model to simulate the collapse of frames in cyclic loading conditions.

The frame geometry and its reinforcement distribution are illustrated in Fig. 10. The concrete has the elasticity modulus E_c=30,400 MPa and the steel has E_s=192,500 MPa, yielding stress of 418 MPa and ultimate stress of 596 MPa. For the mechanical behaviour of the reinforcement, a bilinear elastoplastic model has been adopted with a reduced elasticity modulus in the second branch (E_{s2}=0.009 E_s). Also, Table 2 contains the values for the concrete parameters as well as in the Fig. 11 is illustrated the parametric identification by fitting experimental curve on compression test given in Vecchio and Emara [21]. However, the parameters in tension regime have been obtained using the La Borderie´s model response given by Pituba [3].

Two kinds of support conditions have been used for the numerical analyses. The first one, Case 1, considers the frame clamped on two columns. The second one, case 2, considers the frame with a support beam. The goal is to investigate the possible influence of the support conditions in the analyses performed here.

In the experimental test, initially it has been applied an axial load of 700 kN at each column, which was maintained constant throughout the test. The lateral force has been applied in increments up to the frame ultimate loading be achieved. In the numerical analysis originally performed by Pituba [3], displacements increments have been enforced in the application point of the horizontal force up to the frame ultimate load. In that work, it has been performed loading and unloading trying to simulate the experimental behaviour of the frame. The numerical results were very satisfactory simulating

Figure 10 – Geometry and reinforcement details of the frame

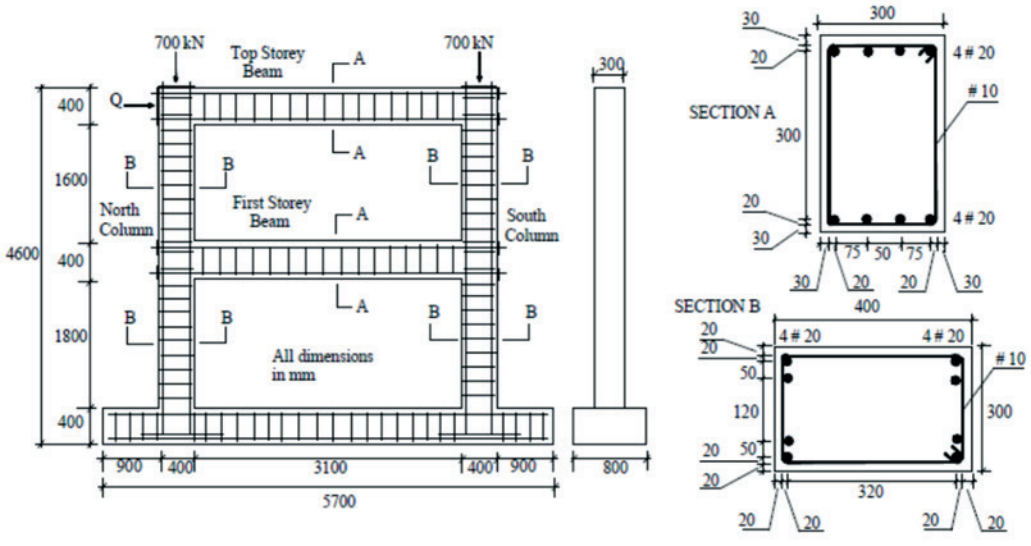

Figure 11 – Parametric identification: a) Uniaxial compression test; b) Uniaxial tension test

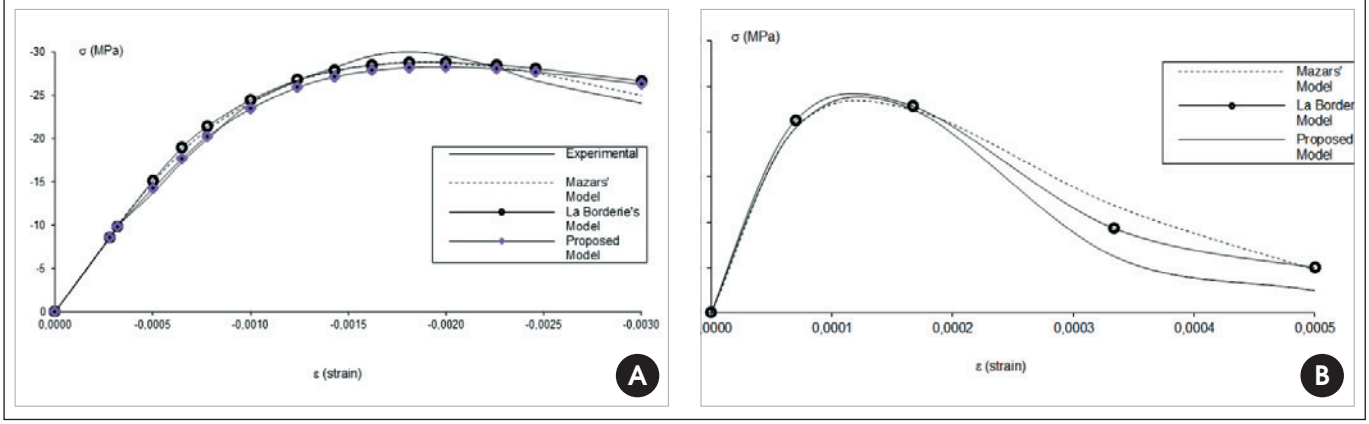

the ultimate load as well as the residual strains.

For the Case 1, the frame has been discretized into 30 finite elements, 10 of which have been used in the discretization of each column and 5 in each beam. The transversal sections have been divided into 10 layers. For the Case 2, the same discretization for the Case 1 has been used with addition of 14 finite elements to model the support beam. In order to investigate the potentialities of the improvement of the damage model proposed in section 2.2, the framed structure has been analyzed attempting to perform an unloading of the horizontal force Q, including reversal loading. The goal is to observe the consistency of the qualitative response provided by the damage model. The numerical and experimental responses are illustrated in Fig. 13 for the both cases of support conditions, where the graphs represent the applied horizontal force versus horizontal displacement computed at the superior floor of the frame (see Fig. 10). Note that the numerical responses for the both support conditions are quite similar. In fact, the damage

Table 2 – Parameters values of the proposed damage model – RC Frame

Tension	Compression
Y_{01} = 0,72 x 10^{-4} MPa	Y_{02} = 0,17 x 10^{-2} MPa
A_1 = 49	A_2 = 0,30
B_1 = 6560 MPa^{-1}	B_2 = 5,13 MPa^{-1}
β_1 = 1 x 10^{-6} MPa	β_2 = 1 x 10^{-3} MPa

Figure 12 – Mesh and Boundary conditions used for the analyses

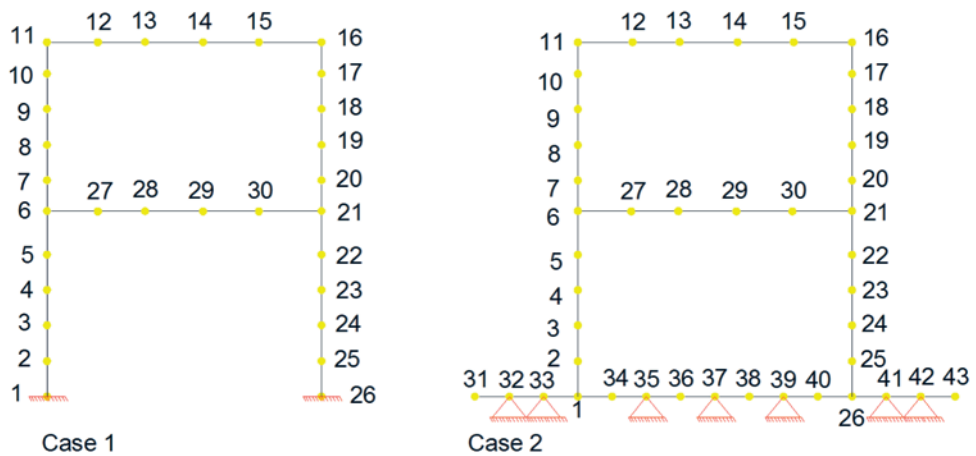

model does not consider the concrete strength complementary mechanisms for the mechanical behaviour of the framed structure, such as: aggregate interlock and dowel action. Following Vecchio and Emara [21] and Nogueira et al. [22], the shear contribution is important for this structure leading to different numerical responses as evidenced in Nogueira et al. [22].

It can be noted the agreement between numerical and experimental responses during the unloading process. In fact, it evidences the good performance of the damage model to capture residual strains. In this stage, the loading capacity of the frame has been achieved and the damage level is high in most zones of the frame, as it can see in Figure 14 for the Case 1. Note that the figure presents the damage distribution related to tension regimes (D_1) because the analysis has shown the importance of that variable. This is related to the concept of the damage model proposed in this work. It is possible to observe the evolution of the damage processes within the stages displayed in Fig. 14.

Besides, in Fig. 13 the symmetric behaviour of the frame related to load capacity when the horizontal force Q is applied to right direction and then it has been changed to left direction. In the first case, the load level capacity is about 294.3 kN. On the other hand, the load level capacity is 286.6 kN for the second case. Note yet, the capability of the model to simulate the recovery of the load capacity when the first cycle of loading is complete.

There are some parts of the frame with high values of damage variable D_1 that together with the yielding of the reinforcement bars contribute to concentrate damage-plastic zones like plastic joints. It can be observed these zones in first and second floor beam/column junctions and, mainly, in the supports of the frame. These observations are in agreement with described in Vecchio and Emara [21].

4.3 Reinforced concrete beam with unsymmetrical reinforcement

The third numerical application is about a reinforced concrete beam with unsymmetrical reinforcement. This numerical application has been originally performed by Pituba and Lacerda [5], but only monotonic loading has been imposed to the beam in that work. The elastic parameters of the concrete are f_c=25MPa and E_c=32.3MPa. For the reinforcement has been adopted E_s= 205 GPa, yielding stress 590 MPa and ultimate stress 750 MPa. The geometric characteristics of the beam are given in Figure 15. The loading is composed by two equal forces applied on the beam.

Table 3 presents the values of the parameters used in the analysis and adopted from Pituba and Lacerda [5], however in this work is considered the plastic strains generated by the damage model.

The structure has been discretized into 16 finite elements and the transversal sections have been divided into 15 layers where 3 layers have been used to represent the reinforcement bars according with Fig. 15.

The numerical and experimental responses are illustrated in Fig. 16.

In the first loading, it is noted that the numerical results are very close to the experimental ones evidencing a good quality response in the sense that captures the history of the mechanical behaviour of the structure. In this work, the numerical analysis continues with the unloading process about 110 kN, where the beam is quite damaged in tension zone (bottom of the beam) and the reinforcement bars present evident yielding in the same zone, Pituba and Lacerda [5]. The value to start the unloading process (110 kN) has been adopted in order to overcome numerical problems related to high values of the damage variable in tension.

The unloading process modelled by the damage model presents very important qualitative results. The damage model can

Figure 13 – Numerical and experimental results of reinforced concrete frame

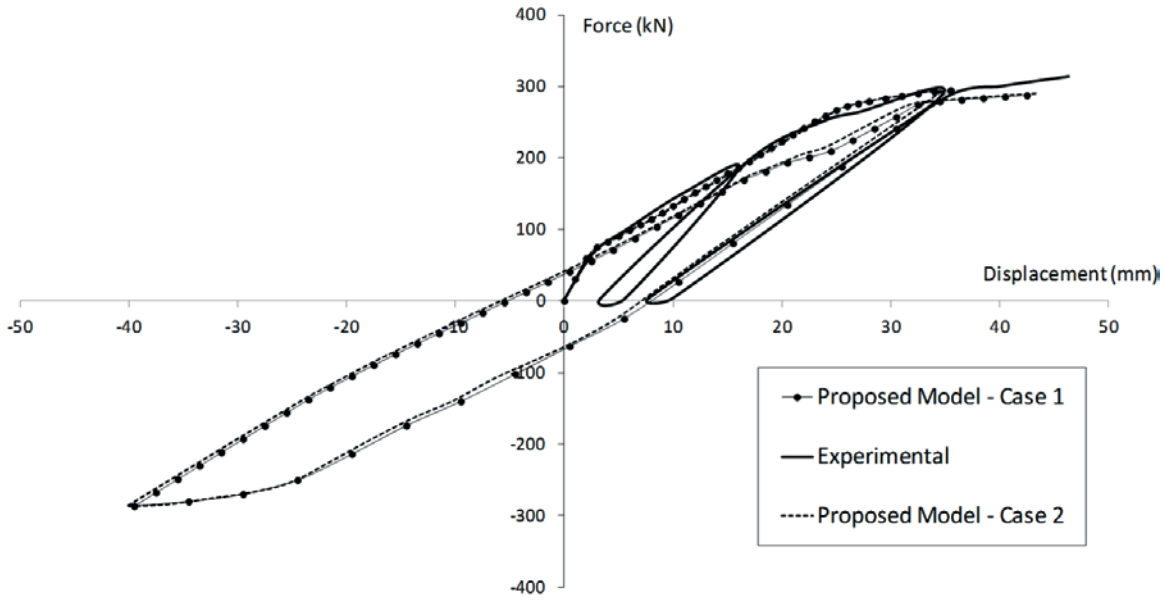

Figure 14 – D_1 damage distribution: a) First loading (Q=59.3 kN); b) First loading (Q=75.6 kN); c) First loading (Q=294.3 kN); d) Reversal loading (Q=-286.6 kN), see Fig. 12

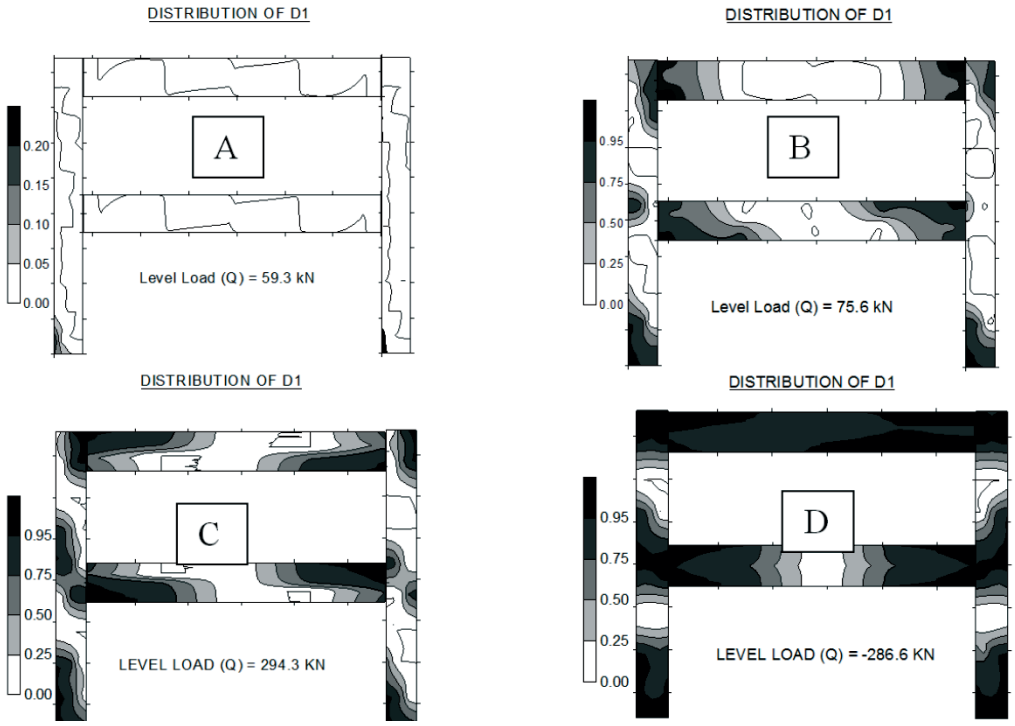

simulate a residual displacement when the reverse loading takes place. Furthermore, it is observed that due to the asymmetric arrangement of the reinforcement, i. e., there is sufficient reinforcement at the bottom to resist the tension stresses in the first loading and insufficient reinforcement (2#6.3mm) on the upper zone to resist the tension stresses in that zone when the load is changed. In this situation, the structure experiences a damage process in tension very intense in the upper zone of the beam. Therefore, it is natural that the strength of the beam be much smaller than in the initial first loading. It can be observed that the concrete does not have strength to the applied force and only the reinforcement resists to tension stresses indicating a strong plastic strain.

5. Conclusions

In this work, an improvement of a damage model incorporating the capability to simulate the unilateral effect of the concrete has been presented. This paper has shown that the proposed damage model assists to the requirements suggested by Welemane and Comery [10] for the micromechanical analysis of the unilateral effect in materials. Besides, the continuity of the stress-strain law across the tension-compression interface has been assured and the model always preserves the isotropy of the elasticity tensor.

In order to validate the proposed model in practical situations, a

Figure 15 – Geometry and reinforcement details

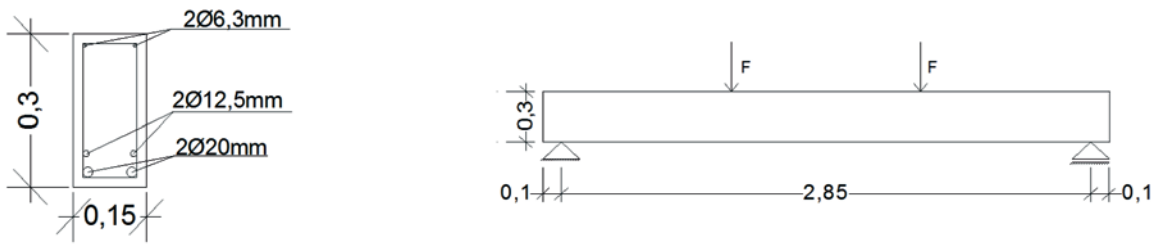

Table 3 – Parameter values of the proposed damage model – RC Beam

Tension	Compression
Y_{01} = 6.0 x 10^{-5} MPa	Y_{02} = 1.0 x 10^{-3} MPa
A_1 = 0.3	A_2 = 1.5
B_1 = 195 MPa^{-1}	B_2 = 10.2 MPa^{-1}
β_1 = 5 x 10^{-5} MPa	β_2 = 3 x 10^{-4} MPa

simplified 1D version has been used. The 1D analysis has shown an efficient and practical employment in the simulation of the damage processes in framed structures submitted to inverse loading, without numerical problems and low computational cost. Besides, the parametric identification is simple. In this case, the damage model could be used in estimative analyses of structures in practical situations, such as: numerical simulation of displacement in cracking concrete beams submitted to service loads, estimative of ultimate load capacity of frames and beams and collapse configuration of reinforced concrete frames.

The obtained results encourage us to proceed in the improvement of the model to deal with more complex phenomena in future works, e. g., blocking and dissipative sliding of closed microcracks lips, non-local version of the model and a more efficient parametric identification of β_1 and β_2, among others. Besides, the damage model can be improved with the consideration of the shear contribution of the concrete for the mechanical behaviour of framed structures even using 1D modelling.

6. Ackowledgements

The authors wish to thank to CNPq (National Council for Scientific and Technological Development) and CAPES (Foundation, Ministry of Education of Brazil) for the financial support.

7. References

[01] Curnier, A. He, Q. and Zysset, P. (1995), "Conewise linear elastic materials", *J Elasticity,* **37**, 1-38.

[02] Pituba, J. J. C. (2006), "On the formulation of damage constitutive models for bimodular anistropic media". *In: C. A. M. Soares (ed) European conference on computational mechanics, 3rd edn. Springer*, pp 371. DOI: 10.1007/1-4020-5370-3_371.

[03] Pituba, J. J. C. (2010), "Validation of a damage model for the non linear analysis of reinforced concrete structures", *Acta Sci-Technol.* **3,** 251-259. DOI: 10.4025/actascitechnol.v32i3.7009.

[04] Pituba, J. J. C. and Fernandes, G. R. (2011), "An anisotropic damage model for concrete", *J Eng Mech-ASCE*. **137**, 610-624. DOI: 10.1061/(ASCE)EM.1943-7889.0000260.

[05] Pituba, J. J. C. and Lacerda, M. M. S. (2012), "Simplified damage models applied in the numerical analysis of r einforced concrete structures", *Rev IBRACON Estrut Mater.,* **1**, 26-37.

[06] Pituba, J. J. C. , Delalibera, R. G. and Rodrigues, F. S. (2012), "Numerical and statistical analysis about displacements in reinforced concrete beams using damage mechanics", *Comput Concrete.* **10**, 307-330.

[07] Comi, C. (2001), "A non-local model with tension and compression damage mechanisms", *Eur J Mech A-Solid.* **20**, 1–22

[08] Desmorat, R. (2000), "Strain localization and unilateral conditions for anisotropic induced damage model", *In: Proc. Continuous Damage and Fracture*, Cachan, 71–79.

[09] Carol, I. and Willam, K. (1996), "Spurious Energy dissipation/generation in stiffness recovery models for elastic degradation and damage", *Int J Solids Struct.*, **33**, 2939–257.

[10] Welemane, H. and Cormery, F. (2002), "Some remarks on the damage unilateral effect modeling for microcracked materials", *Int J Damage Mech.*, **11**, 65–86.

[11] Bielski, J., Skrzypek, J. J. and Kuna-Cisal, H. (2006), "Implementation of a model of coupled elastic-plastic unilateral damage material to finite element code", *Int J Damage Mech.*, **15**, 5-39.

[12] Liu, Y., Teng, S. and Soh, C. (2008), "Three-Dimensional Damage Model for Concrete. II: Verification", *J Eng Mech-ASCE.*, **132**, 82-89.

[13] Araújo, F. A. and Proença, S. P. B. (2008), "Application of a lumped dissipation model to reinforced concrete structures with the consideration of residual strains and cycles of hysteresis", *J Mech Mater Struct.*, **3**, 1011-1031.

[14] Zhu, Q., Kondo, D., Shao, J. and Pensee, V. (2008), "Micromechanical modelling of anisotropic damage in brittle rocks and application", *Int J Rock Mech Min.*, **45**, 467–477.

[15] Zhu, Q., Kondo, D. and Shao, J. (2009), "Homogenization-based analysis of anisotropic damage in brittle materials with unilateral effect and interactions between microcracks", *Int J Numer Anal Met.*, **33**, 749–772.

[16] Pichler, B. and Dormieux, L. (2009), "Instability during cohesive zone growth", *Eng Fract Mech.*, **76**, 1729-1749.

[17] Skarzynski, L. and Tejchman, J. (2012), "Determination of representative volume element in concrete under tensile deformation", *Comput Concrete.*, **9**, 35-50.

[18] Pituba, J. J. C. and Souza Neto, E. A. (2012), "Characterization of macroscopic mechanical behavior of concrete with mesoscopic scale finite element analysis", *In: J. Eberhardsteiner, H. J. Böhm, F. G. Rammerstorfer (eds), European Congress on Computational Methods in Applied Sciences and Engineering*, Vienna University of Technology, Viena, ISBN: 978-3-9502481-9-7.

[19] Matallah, M. and La Borderie, C.I (2009), "Inelasticity–damage-based model for numerical modeling of concrete cracking", *Eng Fract Mech.*, **76**, 1087-1108.

[20] La Borderie, C. (1991), "Phenomenes unilateraux dans un materiau endommageable: modelisation et application a l'analyse de structures en beton", *Doctoral Dissertation*, University of Paris 6, France.

[21] Vecchio, F. J. and Emara, M. B. (1992), "Shear deformations in reinforced concrete frames", *ACI Struct J.*, **89**, 46-56.

[22] Nogueira, C. G., Venturini, W. S. and Coda, H. B. (2013), "Material and geometric nonlinear analysis of reinforced concrete frame structures considering the influence of shear strength complementary mechanisms", *Latin American Journal of Solids and Structures*, **10**, 953-980.